Florida International University

FIU Digital Commons

3-26-2021

Textile-Integrated Wearable Radio Frequency (RF) Wireless Power Transfer and Harvesting for Battery-Free Medical Sensing

Dieff Vital
dvita008@fiu.edu

Follow this and additional works at: https://digitalcommons.fiu.edu/etd

 Part of the Electrical and Computer Engineering Commons

Recommended Citation

FLORIDA INTERNATIONAL UNIVERSITY

Miami, Florida

TEXTILE-INTEGRATED WEARABLE RADIO FREQUENCY (RF)

WIRELESS POWER TRANSFER AND HARVESTING FOR BATTERY-FREE

MEDICAL SENSING

A dissertation submitted in partial fulfillment of the

requirements for the degree of

DOCTOR OF PHILOSOPHY

in

ELECTRICAL AND COMPUTER ENGINEERING

by

Dieff Vital

2021

To: John L. Volakis
    Dean of the College of Engineering and Computing

This dissertation, written by Dieff Vital, and entitled Textile-Integrated Wearable Radio Frequency (RF) Wireless Power Transfer and Harvesting for Battery-Free Medical Sensing, having been approved in respect to style and intellectual content, is referred to you for judgment.

We have read this dissertation and recommend that it be approved.

_____
Shekhar Bhansali

_____
Elias A. Alwan

_____
Douglas H. Werner

_____
Markondeyaraj Pulugurtha

_____
A. Selcuk Uluagac

_____
Shubhendu Bhardwaj, Co-Major Professor

_____
John L. Volakis, Co-Major Professor

Date of Defense: March 26, 2021

The dissertation of Dieff Vital is approved.

_____
John L. Volakis
Dean of the College of Engineering and Computing

_____
Andres G. Gil
Vice President for Research and Economic Development
and Dean of the University Graduate School

Florida International University, 2021

DEDICATION

This dissertation is dedicated to the variety of people who challenged me, sustained me, and made me the person that I am today. I would like to start with my mother, Marie Y. Vital who endured the darkest day of her life, defied her family's will to carry me to term on the day of December 23, 1986. I would not be alive today if she did not make the decision to put her life and freedom on the line for me. Her selfless action makes me believe that everything I do in life belongs to her. Her selfless action was later supported by my aunts Marie Lourdes Vital and Marie Ange Mireille Vital who took care of me when my mom left Haiti [I was eight years old at that time]. They taught me that the two places that will allow me to be a great member of society are school and church. They were happy when I was the top of my class and showed some sadness when I felt to be. Because of that, I always worked hard and compete to be on top because I am so, that put a smile on their face. The other persons that I would like to dedicate this book to are my [biological brothers] Marc-Arthus Vital and Yves-Marie Joseph. These two gave me a title that I cherish the most which is, "father-in-chief". They are the reason why I am always pushing to be the best version of myself. I would like to make a special dedication to my late elder [biological] brother, Mykeull Vital who died during the earthquake on January 12, 2010. They are always by my side when life is tough, and they assure me that the best days are always on the horizon. I also have Michele Laurent and her husband, Claude-Jean Laurent, Marie Merville, Marie Paris, Alexander Lucius Twilight, and Edward Alexander Bouchet. These people are among my biggest cheerleaders. They are the soundtrack of all the success that I have been able to reach for the past 8 years. I cannot thank them enough for being there for me every second of that journey. The other group of people that I would like to dedicate this dissertation to are the

ACKNOWLEDGMENTS

ABSTRACT OF THE DISSERTATION

TEXTILE-INTEGRATED WEARABLE RADIO FREQUENCY (RF)

WIRELESS POWER TRANSFER AND HARVESTING FOR BATTERY-FREE

MEDICAL SENSING

by

Dieff Vital

Florida International University, 2021

Miami, Florida

Professor Shubhendu Bhardwaj, Co-Major Professor

Professor John L. Volakis, Co-Major Professor

Body-worn sensing is becoming increasingly important for patient monitoring, particularly the elderly. The vital signs can be directly transferred to their physicians, personal caregivers, or used for self-diagnosis. To achieve this, wireless, wearable, and self-powered sensors are required. Wireless RF powering/charging, implemented into clothing, upholstery, and smart dressing presents itself as a convenient and practical solution for powering wearable sensors. In this dissertation, the implementation of such wireless charging platforms that are integrated into clothing, and the integration of medical sensor electronics is shown.

Fabric-based wireless charging allows for lightweight, scalable, flexible, batteryless, and comfortable wearing. It is also important to address misalignment issues as users may not always be aligned with the RF transmitters used for charging. In this work, we develop wireless power transfer modalities with the receiving antennas integrated into clothing. The proposed antenna and circuits are realized by embroidering conductive threads onto fabric substrates. The dissertation begins with a characterization of the conductive textiles and microwave circuits used to optimize the substrate materials. Best design guidelines suggested the use of organza fab-

rics and the conductive textiles embroidered in the direction of the RF currents for up to 10 GHz. These design guidelines are used to develop textile-based rectifying circuits exhibiting RF-to-DC efficiency of 77.23% with 22.5 dBm illumination and RF-to-DC efficiency of 70% when illuminated with 8 dBm.

Three clothing-integrated wireless charging platforms are presented. The first configuration used a near-field power transfer for ergonomic charging application. For this specific case, wireless charging was achieved by integrating the receiving antennas and rectifiers into clothing. The transmitters into items such as chairs and bedsheet. This system employed anchor-shaped antennas connected to a rectifying circuit resonant at 360 MHz to collect DC power up to 10 mW across an area of 4 ft $\times$ 4 ft with the near-field transmitting power at 1 W. A second configuration used a far-field transmitter illuminating a 2 $\times$ 3 textile-based patch rectenna array (antenna + rectifier) resonating at 2.45 GHz. This setup exhibited a DC power collection of 0.6 mW from a boosted Wi-Fi signals. In this case, the transmitter was within 10 cm of the receiver.

In the third configuration, an electrochemical sensor, data-modulation and transmitter antenna blocks were added. This sensor system was illuminated by an interrogator transmitting RF power to the bandaid at 2.45 GHz. The bandaid featured a rectifying circuit to convert the external RF power into DC to power a textile-based electrochemical sensor and a voltage-controlled oscillator (VCO). The subject electrochemical sensor was uric acid detector whose uric acid concentration was translated into a frequency shift in the response of the VCO. Uric acid concentrations from 0.2 mM to 1 mM were detected and can be used to assess the health status of chronic wounds. The VCO outputted an RF signal whose frequencies are modulated by the uric acid sensor, and was found to be between 1089 MHz and 1120

MHz. The average sensitivity of the system was 44.67 MHz/mM and the maximum power used was 0.38 mW.

TABLE OF CONTENTS

LIST OF TABLES

LIST OF FIGURES

xiv

xvii

CHAPTER 1

INTRODUCTION

1.1 Problem Statement

The emergence of Internet of Things (IoT), Internet of Everything (IoE), and Internet of Health Things (IoHT) opens a new world of flexible, cost-efficient, low-profile, scalable, and light-weight textile-integrated RF modules in wearable applications. RF modules integrated with wearable have following known applications:

- Assisting military and space exploration programs by providing:

  - Wearable electronics for RF communications and medical sensing in extreme environment,

  - sensor-equipped space suits.

- Constant connectivity between objects and humans

  - concussion detecting helmets, health metrics (heart rate, oxygen levels, etc) data-collection.

  - sleep monitoring, location tracking,

  - integrated sensors in curtains, seats, carpets, security/emergency for various home applications.

These electronics are said to be smart due to the fact that they do not require human interactions to perform a given task. For that, they have to be powered wirelessly in a continuous manner in order to sustain various cycles of uses. Radio-Frequency (RF) powering can be done two ways: (1) in the far field where single antenna and arrays of antennas can wirelessly send power from a distance of more than $2D^2/\lambda$,

where D is the largest dimension of the antenna and λ, its associated wavelength. In addition, the power can be transferred in the (2) near-field, i.e at a distance less than $\lambda/2$. Various antennas and RF modules have been recently proposed. However, the fact that they are developed using rigid substrates, using conventional batteries and obtrusive cases to enclose their electronics, they become uncomfortable to wear. To make the latter wearable, the need of integrating them into clothing is a multifaceted problem and the main attributes include (1) developing fully-flexible, low-profile, and low-cost antennas and other RF modules like rectifiers, voltage-controlled oscillators, etc and (2) developing clothing and accessories like smart jackets, smart dresses, and smart bandages using automated embroidery of conductive textiles into fabric substrates.

1.2   Research Objectives and Contributions

Developing flexible electronic circuits to cater to the high demand in IoT/IoE/IoHT devices requires the design and prototyping of antennas and other RF modules that are resilient to mechanical deformations like bending and twisting, environmental conditions, misalignments between transmitting and receiving modules, and the intermittent movements of the bearers. The work carried out in this dissertation tackles this problem by developing fully-flexible and fabric-integrated wireless power transfer and harvesting systems taking into account the resilience to angular and lateral misalignments when their are used in wearable applications. These structures will be able of performing in both far and near fields while incorporating the capabilities to sustain the aforementioned issues. The milestones achieved within the realm of this work include:

- <u>Optimizing the embroidery process for large-area electronics development</u>: this work involves the optimization of the stitching patterns that provides excellent RF transmission, ability to undergo mechanical deformations like bending and twisting without compromising the RF performance of the structures, ability to be integrated into normal clothing while keeping the initial weight and no discomfort added, and seamless development of electric circuitries on fabric-substrates without fear of loss of conductivity etc.

- <u>Antennas and arrays on fabric substrates</u>: the antennas used in our wearable systems are of low-profile, which means we use dipoles and patch antennas for the most part in far field applications. These antennas are very easy to make and integrate into clothing items.

- <u>RF-to-DC conversion modules on fabric substrates</u>: because our wearable devices need DC power to operate, we feel the need to incorporate RF-to-DC conversion modules to our wireless RF power transfer systems to convert the received RF power into usable DC power to feed the wearable devices. Since we are focusing on low-profile designs, our work on developing single-diode rectifiers capable of exhibiting at least 50% of power conversion efficiency (PCE). This low-profile design will reduce the number of lumped components and the footprint of the circuit. The latter will be later incorporated with the antennas in a complete system for clothing integration

- <u>Inductively coupled power transfer systems</u>: For near field applications, radiation of the Electromagnetic (EM) wave is not considered. The method used is inductive coupling where the transmitting and receiving antennas are at a distance less than $\lambda/2$ and use the electric and magnetic couplings to transfer RF power wirelessly. These methods of transferring power have been subjects of many great works in the past and will be discussed in the subsequent

3

chapter. In near field applications, one of the challenges faced by the antennas is provided by the effects of angular and lateral misalignments between the transmitter and receiver. To overcome this challenge, we develop a new class of antenna known as "anchor-shaped antennas" capable of sustaining all degrees of misalignments while keeping high power transfer efficiencies.

- Battery-less sensor electronics for medical sensing: this work encompasses all the aforementioned endeavors. In addition to that, electrochemical sensing and data modulation are put together with power transfer and rectification into a smart bandage to remotely monitor the healing process of chronic wounds. The bandage will be illuminated by an interrogator composed of a scanner and a spectrum analyzer that sends RF signals to the bandage that features an electronic circuit to convert that received power into DC energy to power an electrochemical sensor. The later has the task to detect the level of uric acid from the wound fluid. A voltage-controlled oscillator converts the uric acid level into an RF signal with different frequencies that can be captured by the spectrum analyzer of any other remote receiver. Based on the modulation of the wound-health data, the healing process of the wound can be assessed. This method is revolutionary due to the fact it is the most user-friendly method to assess wound status where the patient does not need to go to the hospital or doctor's. The data collected by the bandage can be remotely send to the physician or caregiver for follow-ups.

1.3   Methodology

Our objectives are deemed plausible because of some methods and facilities put at our disposal. All the antennas and RF modules will be designed using Ansys

4

HFSS where full-wave analysis can be also performed. For the characterization of the conductive textiles, multiple transmission lines are designed and simulated using HFSS. The conductive traces are chosen to be of copper and the substrates are chosen to be fabric-materials whose EM parameters such as dielectric constant and loss tangent are already published. The fabrication of these structures are done using the automated embroidery of E-threads (Elektrisola-7) onto fabric substrates. The RF characterization is done using a Keysight PNA N5222B vector network analyzer to measure the scattering parameters from which we deduce the insertion loss.

The low-profile antennas and RF modules are designed and fabricated by the same process. The radiation patterns of the antennas are obtained from a STARLab anechoic chamber and the reflection coefficient are determined via a Keysight vector network analyzer.

The anchor-shaped antennas are designed using a single-loop antenna, opening two cavities in opposite sides and placing a dipole in the middle for feeding purposes. The full-wave simulation ifs done through HFSS and fabrication method is the automated embroidery of conductive textiles onto fabric substrates. The single-diode rectifiers are designed and simulated using ADS Keysight simulator and the fabrication is done using automated embroidery of conductive textiles onto fabric substrates. The DC voltage used to compute the RF-to-DC efficiency is obtained by feeding the rectified with RF power provided by a Keysight signal generator and the DC voltage is captured by a Keysight true RMS multimeter.

1.4 Dissertation Outline

In this dissertation, we first present the background and literature study of the different wireless power transfer and harvesting methods and their integration into textiles. This section is laid out in Chapter 2. In Chapter 3 we present the RF characterization of conductive textiles and their use to develop antennas and RF modules. The characterization and optimization of the conductive textile surfaces will be done via the optimization of the stitching patterns, the thread density, and the thread tension. In addition to that, the choice of fabric is important due to their micro-structures. The interconnects are made of high-conductivity silver-based ink to enable soft-to-soft and hard-to-soft connections for frequencies up to 5 GHz. In Chapter 4, far-field fabric-integrated wireless power transfer and harvesting systems are presented and discussed. This system will enable the recycling of microwave signals available anywhere around a cell tower or in the areas where the use of portable phone is ubiquitous. In Chapter 5, the anchor-shaped antenna is developed and the fundamental study is presented. A textile-integration of the anchor-shaped antenna is also developed and used in ergonomic applications. This new class of planar antenna is unique due to the fact that it exhibits high power transfer efficiency while being resilient to both lateral and angular misalignments. In Chapter 6, a smart bandage for electrochemical detection of uric acid from chronic wounds is developed and a setting that mimics *'in-vivo/real-life'* setting is presented. This system features a voltage-controlled oscillator that converts the wound-health data into RF modulated signal for a quick and reliable assessment of the chronic wounds healing status. Finally, Chapter 7 lays out the conclusions and future works.

CHAPTER 2

BACKGROUND AND LITERATURE SURVEY

2.1 Introduction

This chapter consists of the background and prior works on wearable electronics, textile antennas, wireless power transfer and harvesting, as well as smart solution for electrochemical monitoring and sensing. These systems are said to be attractive to the Internet of Things (IoT), internet of Health Things (IoHT), and Internet of Everything (IoE) due to their cost-efficiency,low-power characteristic, low-profile design, ease to manufacture, and ease to be integrated into everyday garment. Their cost efficiency is based on the materials used to manufacture them such as cheap lumped components and fabric substrates to ensure lightweight, flexibility, and comfort while wearing them. The electronic modules are limited in power based on the requirements defined by the federal Communications Commission (FCC) and Food and Drug Administration (FDA) [for on-/off-body applications]. Their low-profile characteristic makes them easy to be manufactured and embedded into clothing. This literature survey starts with the integration of the wearable electronics into clothing items (Section 2.2). Next, some ground work is presented in wireless power transfer and harvesting and its integration into clothing (Section 2.3). Finally, some previous efforts in smart solutions for electrochemical monitoring and sensing are presented (Section 2.4) and all the aforementioned survey is broken down into multiple chapters (Section 2.5).

2.2 Clothing-Integration of Antennas and RF Modules

2.2.1 Loss Characterization of Conductive Textiles

Quality assurance in continuous and undisturbed wireless power transfer, harvesting, sensing, and data transfer for modern personal and customized IoT devices is the key when it comes to the bearer's movement and surrounding. These IoT devices are usually developed using flexible substrates where the metallization is made of conductive surfaces from tapes [1], screen printed nanowires [2], liquid metal alloy [3], inkjet-printed electronics [4], and conductive E-threads [5, 6, 7, 8]. The surfaces made of E-threads has been the most attractive metallization due to their ruggedness and low fabrication cost from automated embroidery using commercial stitching machines. These E-threads are made of 7 silver-coated polymer-filaments twisted together to make a strand in order to strengthen and improve the strand. Each filament has a core of diameter 10 μm and coated with a copper layer of 5 μm. The brand name of these threads is "Elektrisola" and this thread has been proven to be the best candidate for textile antenna manufacturing due to high resolution achieved in the recent work [7]. The conductive surfaces are made via the automated embroidery of these threads onto fabric substrates. The resulted prototypes are fully-flexible, durable, and capable of seamless integration into clothing, wearable, and portable items. Past publications have demonstrated an excellent RF performance of E-threads used to develop antennas and other RF modules. The performance exhibited was similar to that of copper tapes [5], demonstrating high RF conductivity of the surfaces. Furthermore, excellent robustness and tolerance across temperature ranges were observed [8].

Consistent RF performance of the developed devices was retained by precisely controlling the parameters pertaining to the embroidery process of the conductive

textiles as well as the choice of fabric substrates. Among the available parameters, we selected the number of threads per millimeter of embroidery known as "thread density". We also controlled the alignment of the thread with respect to the direction of the RF current as the "stitching pattern". Finally, the embroidery "tension" that is responsible for the interweaving of the conductive threads within the fabric substrates to realize a smooth seam with no presence of wrinkles or puckering. To test this, three different transmission lines made of E-threads embroidered onto denim substrate are designed and prototyped. For port excitation, two SMA connectors are attached to the extremities of the textile striplines using solder. The transmission loss was determined from frequencies of up to 5 GHz. The results obtained from our experiment suggest that when the threads are aligned in the direction parallel to the RF current (90°-fill stitch), the optimal conductivity is achieved. That is up to 0.3 dB/cm of loss exhibited from 0.5 to 3.5 GHz. By doing so, it is expected that the finished prototypes will perform at their highest conductivity and will be able to withstand any mechanical deformation with no fear of compromising their RF performance. More about this aspect of the study is discussed below.

2.2.2 Effects of Mechanical Deformations on the RF performance of the Textile Transmission Lines

As previously stated, the primary reasons why wearable electronics are attractive reside in their full flexibility, light weight, durability, and their ability to be easily incorporated into daily garments. The latter require excellent performance functionality regardless of the conformal nature of the conductive surfaces nor the robustness to flex motions [9].

2.2.3   Flexible Interconnects Made of Epoxy for Textile Integration of RF Modules

The devices that are compatible for IoT applications are required to be wireless, energy independent, and resilient to mechanical deformations [10]. This will facilitate their integration into fabric substrates with no fear of impacting their surroundings, the manufacturing process, repeatability, and consumer experience [11].These necessities can be counted for when using interconnects for integration of fabric-based RF devices [12], wireless power transfer and harvesting, all on smart textiles.

Two main characteristics of these wearable devices are flexibility and reliability. They represent the key features in enabling smart textiles. Flexibility was achieved by controlling the embroidery parameters discussed in the previous sections and allowed for flexible interfaces. The latter still have to overcome the burden of solder-based interconnections presenting hard phases that limit the flexibility of the entire structures. The solder-based interconnections will be more pronounced when using large-area electronics where lumped components are used. To mitigate this issue, we employed epoxy-ink to replace the solder-based joints to compensate for the compromised flexibility. In this study, four TTLs were designed and fabricated using the automated embroidery of conductive textile on organza-based substrate. The port excitation was represented by two SMA connectors in each TTL connected to the stripline using solder and ink. Two continuous and two segmented (discontinuous) transmission lines where the interconnects are made of solder and ink were tested for flexibility, reliability, and impact on their RF performance. The conductive ink used was CreativeMaterials 127-48 with 82% of silver nanoflakes cured for 60 minutes at 110° to provide highest conductivity.The loss performance suggested that the interconnects made of epoxy-ink exhibit 50% less of connection loss than their

solder-based counterparts. That is, 0.1 dB/cm from DC to 5 GHz exhibited by the TTLs made of ink-based interconnects. Their solder-based counterparts experienced connection losses of up to 0.35 dB/cm for the same frequency range. Moreover, the performance of continuous and segmented TTLs are found to be similar. Their RF performance remained intact even after 10 cycles of bending. The proof of concept was validated using a 7-element Yagi-Uda antenna where the interconnects were made of solder and ink. In fact, the textile antenna made of ink-based interconnects outperforms the one made of solder-based interconnects, which proved the consistency of the results. This method can be used as guideline for clothing-integration of RF modules for wearable applications. The details about this study will be found in Chapter 3.

2.3 Wireless Power Transfer and Harvesting Methods

2.3.1 Radiative Power Transfer

Collection and recycling of ambient microwaves from wearable and portable devices like cellphones, laptops, and Wi-Fi routers has been of interest ever since the era of internet of things has started. The collected DC power is use to operate low-power sensors and other IoT devices [13, 14]. These low-power sensors and devices are in need of pW or μW of power to operate. The specific examples of these devices include temperature sensors, consuming power between 113 pW and 1.4 μW [15, 16, 17, 18, 19], current and voltage sensors as well as biosensors for micro-electromechanical systems (MEMS) applications, consuming 9.3 nW and 436 μW power [20, 21, 22, 23]. Therefore, power harvesting can be without hesitation used to operate such sensors, however one important concern is related to the inte-

gration of RF-harvesting antenna-arrays in items of clothing or upholstery. . The proposed conductive textile technology applies well to microwave frequencies as well as conductive ink, since they provide continuous metal phases due to presence of metallic-threads and metal nanoparticles in inks [24]. A slight difference might be noticed because the percentage of copper or silver used in each of the aforementioned materials are based on the applications. A notable comparison can also be made with metallized fabrics. Metallized fabrics may have shown better resolution than embroidery since the conductive surface is continuous, but may require a sophisticated laser cutting equipment. The embroidery process, however works well with any off-the-shelf sewing machine and does not require large-scale commercialization for low-cost manufacturing.Another drawback of the metallized fabric is the fact that excessive wrinkles can introduce small cuts that can compromise the conductivity of the conductive surfaces. The embroidered surfaces on the other hand, can withstand any kind of mechanical deformation and also exhibit robustness and durability [25, 26], [27] , including durability after washing and ironing. The embroidery process are CAD-based and therefore feature-resolution as low as 100μm [28], sufficient for many microwave applications, have been achieved. For textile-integration of wireless power transfer and harvesting, we propose arrays of patch antennas (low profile) combined with single-diode rectifiers. The uniqueness of the rectifier is found in the (1) use of a single-diode in a resonant circuit that achieves more than 50% of RF-to-DC conversion efficiency (up to 70%) and (2) elimination of the power management circuit that could contribute in the bulkiness or complexity of the system. These special design considerations allow easy manufacturing process and maintenance of the flexible nature of the cloth without compromising the power conversion efficiency. In previous works, single-diode rectifier configurations have been demonstrated [29, 30, 31], but since they used rigid substrates, they can-

not be integrated into clothing. This problem can be solved by implementing the rectifiers into fabric substrates. Having developed the antenna and rectifier elements, 2×2 and 2×3 rectenna arrays are prototyped and tested at 2.45 GHz. We also test the fabricated rectenna in realistic Wi-Fi environment where the available signal is given by a nearby phone, Wi-Fi router, and Cell tower. In this context, we show a new method of power harvesting in far field, in which available ambient power is externally amplified using a standalone amplifying system and then harvested. The 2×2 array was tested for ambient RF power and the 2×3 array used an incident power coming from a Wi-Fi router that was amplified. The DC power collected at the output of the 2×2 array was found to be 100 μW, while the 2×3 array shown a collection of 600 μW that was used to light up three LEDs placed in parallel. The details about the design, fabrication and outcomes of the tests are presented in Chapter 4. Other methods can be used in power harvesting. This include the inductive and capacitive power transfer that are done in near field ($\lambda/2$-distance). These methods are explained below.

2.3.2   Inductive and capacitive Power Transfer

Wireless RF power transfer and harvesting has been the corner stone of modern technologies, such as Internet of Things (IoT), wearable electronics, consumer electronics, medical, and portable equipment [32, 33, 34, 35]. The most reliable among these applications have been using the wireless power transfer in near-zone, where high efficiency of WPT (>50%) are plausible. Indeed, this technology has percolated to the most common consumer electronics application, such as wireless charging of wearable and portable devices like mobile phones. Other applications include healthcare, sport, space, and automobile.

In the past, single or multiple turns of wire have been traditionally used to design antennas/resonators for near-field wireless power transmission[32, 36, 37, 38, 39, 40, 41]. With regards to these, most of the prior research has focused on the goal of increasing the distance between the receiver and transmitter while maintaining high power transfer efficiency (PTE). Generally, this is accomplished either by using 3-D antenna geometry (as opposed to loops, which are planar) or by using intermediate structures positioned between the transmitting and the receiving antennas (relays). A notable example is strongly coupled resonance method, which uses an intermediate helical structure near the transmitting as well as near the receiving antennas [42]. This method aims at strengthening the electric/magnetic field used to transfer power from the transmitter to the receiver. A variation of this method consists of a parasitic loop in lieu of the helical element [43, 41]. The strategy of introducing intermediate elements has been also been extended to multiple (more than two) parasitic elements where the transmitter-to-receiver distance equivalent to several loop dimensions was achieved [44]. An important development within the strongly coupled regime was the use of planar versions of parasitic elements, where the parasitic loop and the excited loop differed in radii, but were placed in the same plane [45]. A version of this resonator for cylindrical shaped platform was shown in [46]. Apart from the above, metamaterial-based loading elements are also proposed as an intermediate structure for efficiency enhancement for longer distances [47, 48, 49]. In spite of the different topologies used to develop these antennas, the PTE decreases due to the axial mismatch between the transmitter and receiver as well as increase in distance of separation. The challenge here is to adopt this power transfer approach and overcome the issues of decaying PTE. In the next section, the issue of PTE decay due to misalignments is addressed and discussed.

2.3.3 Misalignment in Wireless Power Transfer

In wireless power transfer, the transmitter and receiver are never perfectly aligned, which degrades the PTE. The influence of lateral and angular misalignments on the PTE has remained a big challenge to overcome. That drew the attention of various researchers to find a solution to that. For the first time, the misalignment issued was tackled by Fotopoulou and Flynn [38], where the authors presented an analytical model to predict the performance of the power transfer system when it is subject to both lateral and angular misalignments. Other works addressed the problem by featuring an electronic tuning circuit suitable for Class-E inverter [50], an impedance compression network [51], and a T-model matching network [52], allowing 50% efficiency for a lateral misalignment of up to 70 cm at 10.14 MHz. To achieve this milestone, the antenna had a power (driving) coil of diameter 98 mm and a helical (transmitting) coil of 120 mm. Following this attempt to solve the misalignment issue, several spatial antenna configurations have been investigated. For example, The work done in [53] used 3-D omni-directional antenna to achieve 60% efficiency for all angular positions. Likewise, strongly coupled magnetic resonator (SCMR) based antennas, conformed over a cylindrical surface [46], were used to achieve 40% PTE regardless of the angular position. Even if they help in overcoming the issue, their applications are for curved surfaces. They cannot be employed in scenarios that require planar integration.That's where our contribution comes in.

In this regards, propose a new class of planar, misalignment-resilient antenna for wireless power transmission scenarios of small distances ($g < \lambda/20$). In the cases when the antennas are clothing-integrated and are in a close proximity to the receiver, resilience to misalignment can be achieved using this new antenna system. This makes this new system appealing to wearable applications. For such wearable applications, intermittent movements by the bearer are expected and therefore

resilience to misalignment is a top criterion. The proposed antenna is known as anchor-shaped antenna shown in Fig. 5.2. This new topology uses electric and magnetic coupling modes to ensure insensitivity to angular and lateral misalignments. In this structure, we introduce discontinuities in the loop that provide fringing electric-fields in the vicinity of the antenna. The resulted electric fields extend beyond the coupled surface (aperture) of the antenna and can combine with those of the nearby antenna (receiver) for high PTE achievement. A dipole-like bar placed in the middle of the two semi-circles aid in establishing resonance (as opposed to that in a loop). The bar also helps in miniaturization and frequency reduction of the antenna. Both of these factors allow increased couplings for the misalignment cases. Furthermore, the proposed planar geometry is simpler to fabricate compared to helical and other recently reported 3-D configurations.

In the past, coupling between discontinuous loops has been studied for microwave filter [54]. In these works, discontinuity or gap that is introduced, allows the generation of fringing electric fields, leading to an electric-field type coupling between the two loops. This is on-top of the inherent magnetic coupling between the metallic regions of the loop. Therefore, the discontinuity can give birth to magneto-electric couplings, where double resonance and frequency bifurcation effects are observed [55]. The proposed anchor-shaped structure uses similar combination of electric and magnetic couplings where frequency bifurcation is almost non-existent. We designed, simulated, and fabricated two anchor-shaped antennas resonating at 360 MHz and 600 MHz, respectively. The antenna resonating at 360 MHz has a diameter of 15 cm and its corresponding results were used to compare against those of a loop antenna of the same size resonating at 600 MHz. The latter was also compared with the anchor-shaped antenna resonating at 600 MHz. Lateral misalignments up to 10 cm and angular misalignments of up to 180° were performed and discussed. The

results suggested that by replacing the loop antenna by its anchor-shaped counter, we were able to achieve up to 25%, 65%, and 30% improvement under lateral, elevational, and azimuthal misalignments, respectively.This antenna topology was used to develop wearable systems for power transfer and harvesting.

2.3.4 Use of Anchor-Shaped Antennas on Fabric for Wireless Power Transfer and Harvesting in Ergonomic Applications

Wireless transfer of radio frequency (RF) energy over time is critical for Internet of Things (IoT), Internet of Health Things (IoHT) and other wearable medical sensors/devices. These devices work like standalone systems to perform the intended tasks. Notably wireless RF power can supply enough power to continuously power battery-free circuitries or in-situ chargeable devices. Although the sedentary mode seems to be attractive for wireless power transfer, it comes with some consequences such as the never-ending motions of the device's bearer. This causes misalignments between the body-worn antenna and the transmitting antenna that is positioned on the back of a chair, bed, mattresses, bed sheets, etc. Notably, wireless charging modality, allowing movement up to 2 to 3 ft. from charging surfaces could be beneficial. These movements also include minor movements while sitting or sleeping. Misalignment issues in RF power transfer have been investigated for a long time. A lot of work has been done to mitigate this problem, but most solutions focused on developing 3-D structures that are not eligible for planar clothing integration [56]. Prior related research on transferring power has been successful and the power transfer efficiency (PTE) is achieved for distances from 1 cm to 3 cm

with as high as 90% [57]. However, when extending the aforementioned range and subject the system to misalignment, the PTE decreases exponentially with distance $(1/r^3)$ [58, 59]. Various efforts have been put forth to solve this problem [60, 61]. After several attempts, the influence of misalignment between the transmitter and receiver on the PTE still remains a big challenge to deal with [62, 63, 64]. Furthermore, there is no prior work on fabric-integrated wireless power transfer (WPT) system operating at distances of up to several feet from the source. With this in mind, we seized the opportunity to propose wireless power transfer systems that are completely integrated into items of clothing and can interact with other clothing surfaces (such as upholstery, linen, curtains, etc.) for wireless charging. The system uses a proposed class of anchor-shaped antenna [65], which is shown to operate better than the traditional loop antennas under misalignments. The work presented in [65] laid the foundation of the anchor-shaped antenna performance that makes it better than its previously published counterparts. We further demonstrate that this class of antennas operate quite well for extended ranges, i.e. up to 3 ft. from a transmitter, and operate well under lateral misalignments. The latter is known to be the key to textile-integration of wireless charging modality into items of clothing and upholstery. We further integrate minimalistic rectifier circuits, which use transmission lines with optimized lengths and single-rectifying diodes. The antennas and rectifier circuits are combined to show excellent collection of wireless RF power over extended ranges.We designed, simulated, fabricated, and tested a textile-integrated wireless power transfer and harvesting system to operate at 360 MHz. The antennas used in this system are anchor-shaped made via the automated embroidery of conductive textiles into denim fabric. A textile-based single-diode rectifying circuit was co-optimized and combined with one of the anchor-shaped antennas at the receiving side of the system. The DC power was collected when the transmitter and

receiver were separated using all degrees of misalignments within 4 ft. The results demonstrated that an average of DC power ranging from 2 to 10 mW was collected within 4 ft. This power level is appropriate to operate a wide range of IoT devices. Tying all wireless power transfer and harvesting modalities together, we proposed the development of a smart bandage using incident RF power to monitor the healing process of chronic wounds. In the next section, the details pertaining to the bandage are presented and discussed.

2.4 Smart Solutions for Electro-chemical Sensing Using Data Modulation

Chronic wounds has been an prevalent medical condition in the United States targeting more like the geriatric population. A study reported that 8.2 million (15%) of Medicare beneficiaries are impacted by chronic non-healing wounds. Annually, an amount between 28 and 97 billion USD are invested in primary and secondary diagnoses of chronic wounds [66, 67]. The causes of chronicity of wounds include poor diet and wound management. Ability to learn the status of a healing wound without having to open the dressing is critical for improving wound monitoring in general. With that, no fear of relapse because the intervention of personnel with poor wound management skills can be avoided. This can be done by developing an electronic wound monitoring with sensing electronics embedded in the bandage itself. A close attention was drawn to assessing the wound status, which led to biosensing research that has yielded several physiological indicators referred to as biomarkers among which we find temperature, pH, bacterial loads, and uric acid [68]. Uric acid was found to be the most interesting finding due to the fact that it is associated to the severity and inflammation of the wound [69, 70, 68, 71]. Some

works have demonstrated that a concentration of uric acid above 6.8 mg/dL (0.4 mM) leads to inflammation in the wound [72, 70] and a concentration below that is an indication of the healing progress of the wound.Various smart bandages have been developed for wound monitoring [73].

2.5 Organization of the Dissertation

The work developed in this dissertation is organized in the following chapters as: (1) the loss performance of textile-based transmission lines where the interconnects are made of solder and epoxy/ink in Chapter 3, (2) the development of a textile-based power transfer and harvesting system in far-field in Chapter 4, (3) the development of a clothing-integrated wireless charging platform using anchor-shaped antennas in Chapter 5, (4) the use of wireless power transfer and harvesting combined with electrochemical sensing and data modulation to develop a smart bandage for chronic wound monitoring in Chapter 6, and (5) the major takeaways and future endeavors in Chapter 7.

CHAPTER 3

RF CHARACTERIZATION OF CONDUCTIVE TEXTILES AND THEIR USE IN DEVELOPING RF MODULES

3.1 Introduction

In this chapter, we present the study on the loss-performance of the proposed textile-transmission lines (TTLs) for different stitching pattern or thread alignments. The interconnects used for the study are solder-based. This study is followed by the RF performance of these TTLs when they are subject to mechanical deformations like bending and twisting. To establish uniformity in their performance when undergoing serious mechanical deformations, the three embroidery parameters mentioned above become the focus of the investigation. The latter uses the optimal stitching pattern along with the other two parameters and subjects two textile-based transmission lines (TTLs) made of two different substrates such as denim and organza to bending and twisting while monitoring the change in their loss performance for up to 10 GHz. The design and manufacturing process of these TTLs are the same as discussed in the previous section. We found out that by using the 90°-fill stitch embroidery technique, using 14 threads/mm, and selecting a thread tension of 4, the resulting transmission lines are found to be resilient to mechanical deformations and that those that are made of organza exhibit less loss due to the fact that this fabric substrate is made of various grids that offer a smooth weaving path to the conductive threads. In effect, 0.6 dB/cm for up to 10 GHz of loss was exhibited by organza-based TTLs while their denim-counterpart suffer from losses as high 1.08 dB/cm for the same frequency range. This excellent RF performance of the organza-based TTLs can also be explained by the fact that they have less moisture absorbance unlike their

- **Solder-based interconnects making hard phases**
- **Ink-based interconnects making crack-free phases**
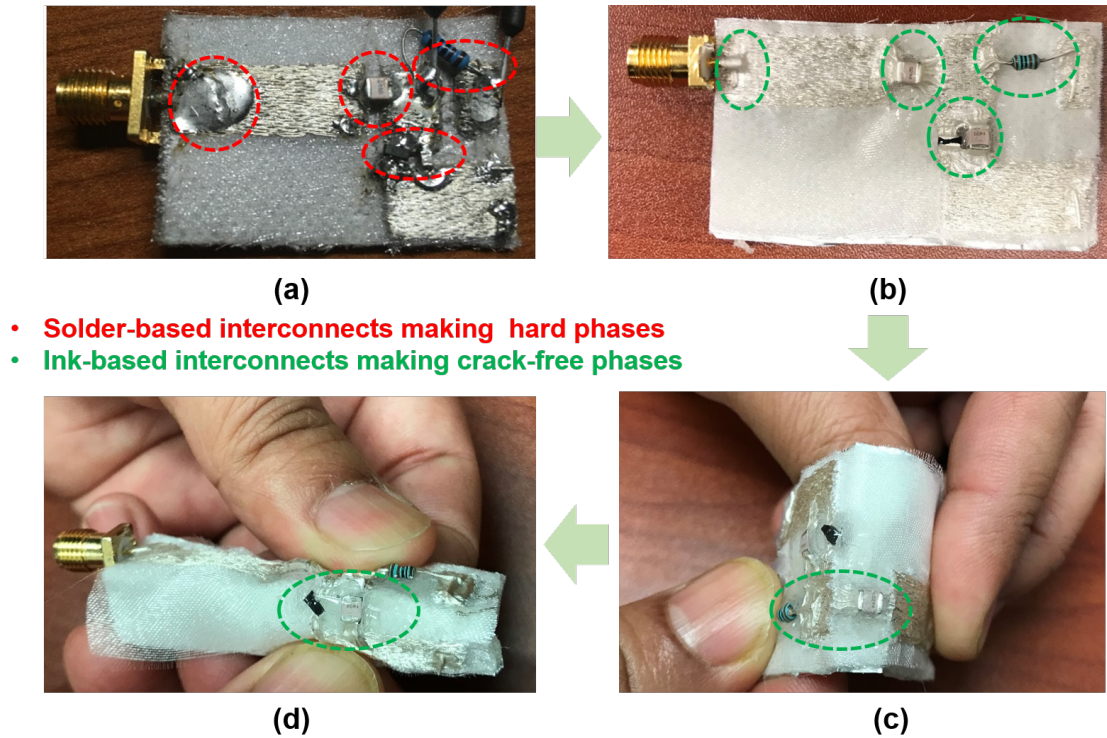
Figure 3.1: Interconnects between lumped elements (hard-to-soft) made of solder: a) Picture of the interconnects made of solder, b) Picture of interconnects made of ink, c) and d) Pictures of crack-free interconnects made one ink showing no crack even after several cycles of bending in all directions.

counterpart (denim). The latter is made of cotton that serve as arrays of traps to moisture and other agents that contribute to losses in the RF modules.

Finally, the study is concluded with the substitution of the solder-based interconnects by ink/epoxy-based interconnects and the evaluation of their corresponding connection loss with respect to that of their solder-based counterparts (see Fig. 3.1).

3.2 Optimization of embroidery parameters and RF Performance

The study debuted with the design and fabrication of four microstrip transmission lines (MTLs). The first one was made of copper cladded onto a DiClad880 substrate ($\epsilon_r = 2.2$ and $\tan\delta = 0.009$) and the other three MTLs are made of Elektrisola-7 embroidered onto denim fabric (Fig. 3.2). The stitching patterns used in the textile

(a)

(b)
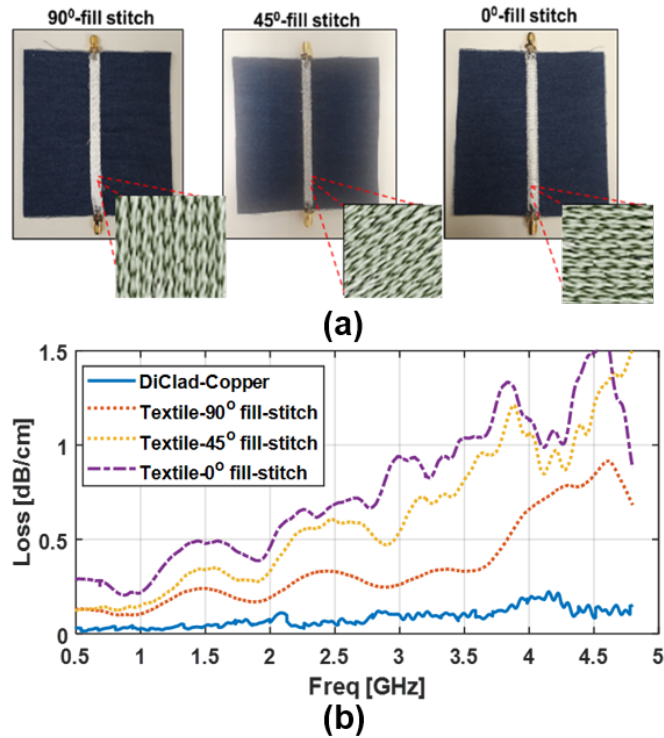
Figure 3.2: Loss-comparison of stitching patterns in textile-based transmission lines made of Elektrisola-7 embroidered onto denim fabric. (a) Photos of finished prototypes with three different embroidery patterns under study (angles are estimated between the thread and horizontal axis) and (b) Measured loss-performance of different patterns.

MTLs are: (1) 90°-fill stitch, which means that the conductive threads (Elektrisola-7) are embroidered in the direction of the RF current, (2) 45°-fill stitch, which means that the conductive threads are embroidered at 45° with respect to the direction of

the RF current, and (3) 0°-fill stitch, which means that the conductive threads are embroidered perpendicularly to the direction of the RF current. The scattering parameters were measured using a Keysight PNA N5222B and the loss performance was deduced using the equation 3.1.

$$Loss_{dB/cm} = \frac{10 \times log(1 - |S_{11}|^2 - |S_{21}|^2)}{L_{stripline}} \qquad (3.1)$$

The measured loss performance is reported in Fig. 3.2(b). This figure suggests that by aligning the conductive threads with the direction of the RF current (see Fig. 3.3), the loss performance is improved by 0.7 dB/cm at 3.5 GHz. It can be also noted that the 45°-fill stitch embroidery pattern shows intermediate loss performance. When compared to its copper MTL (cladded onto the DiClad880 substrate), the best performance was approximately 0.25 dB/cm for the whole transmission line. We also investigated the use of double-layered of conductive threads embroidered onto fabric to see if any improvement was possible. For this, we embroidered another layer of conductive threads (using the 90°-fill stitch pattern) on top of a textile MTL using the same stitching pattern (see Fig. 3.4(a)). The loss performance was evaluated using the equation 3.1 and reported in Fig. 3.4(b). As can be seen from
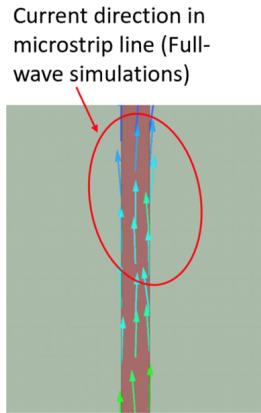
Figure 3.3: Illustration of the RF current flowing along the 90°-fill stitch Textile transmission line.

Fig. 3.4(b), using two layers of conductive threads to make a textile MTL did not

appreciably improve the loss performance. In overall, the 90°-fill stitch was found to be the optimal stitching pattern to embroider excellent textile transmission lines. That is, the performance of a textile transmission made of E-threads embroidered onto fabric substrates is dependent on the alignment of the threads with respect to the direction of the RF current. In addition, by aligning the threads in the direction of the RF current will result in achieving the least resistive path to the current. These results can be served as guidelines for the development of textile antennas and circuits for wearable applications.
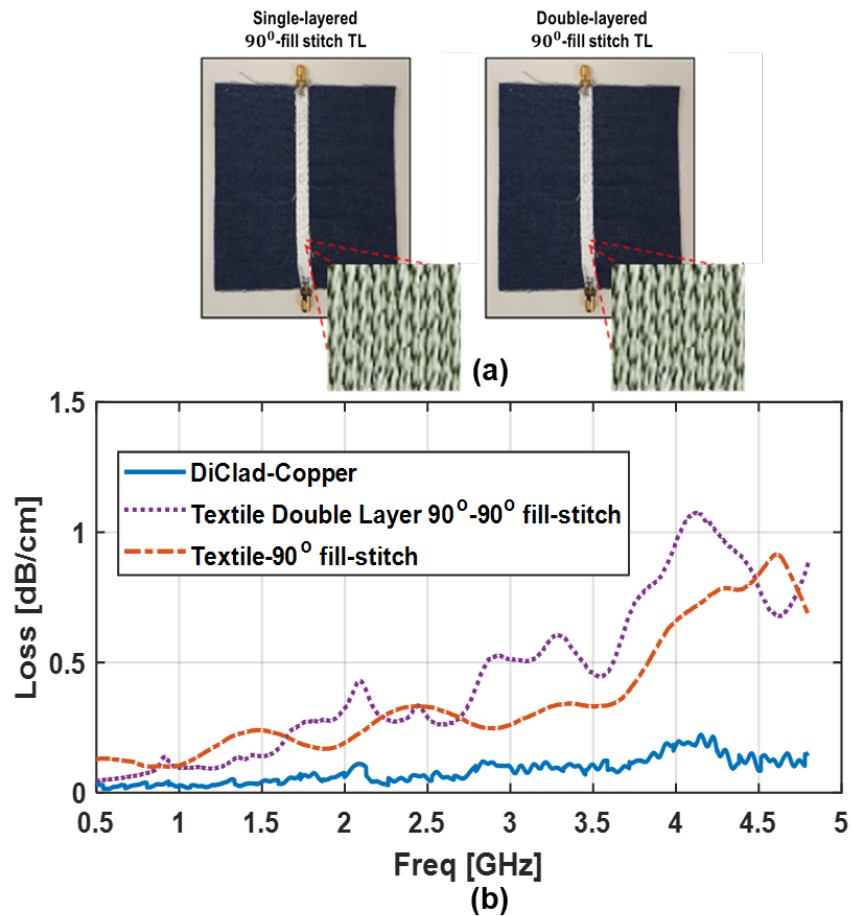
Figure 3.4: Loss-comparison of the double-layered textile transmission lines compared with that of single-layered textile transmission lines.

3.3 The Effects of Mechanical Deformations (Bending and Twisting) on the RF Performance of TTLs with Solder-Based Interconnects

As the textile TTLs will be used in the implementation of textile antennas, circuits, and RF modules, we decided to study the effects of mechanical deformations (bending and twisting) on the performance of the TTLs. In addition to that, we wanted to see how the choice of fabric substrates influence the loss performance of the TTLs. In this study, we considered two different substrates denim and organza, 90°-fill stitch (embroidery pattern), and the TTLs underwent bending and twisting. The loss performance was evaluated from scattering parameters using the equation 3.1 and the measured results were reported in Fig. 3.5. Two important stitching parameters namely, stitching density optimized to be 14 threads/mm and thread tension chosen to be 4 (from a scale 0 to 9). the design and fabrication processes were the same as previously discussed. The results from Fig. 3.5 (Bottom left and right) suggest that bending and twisting did not have a noticeable effect on the loss performance of the TTLs.

However, it can be seen that the TTLs that were made of organza outperform those that were made of denim. Specially, organza-based TTLs exhibited a loss of up to 0.6 dB/cm for frequencies ranging from DC to 10 GHz, while those made of denim suffered from a loss of 1.08 dB/cm for the same frequency range. The results did not change from one mechanical to another one. As a conclusion, the best design guideline for textile electronics is the embroidery of Elektrisola-7 in the direction of the RF current onto organza fabric substrates. The key reason why organza appears to be the best candidate for the design guideline of textile RF modules is because
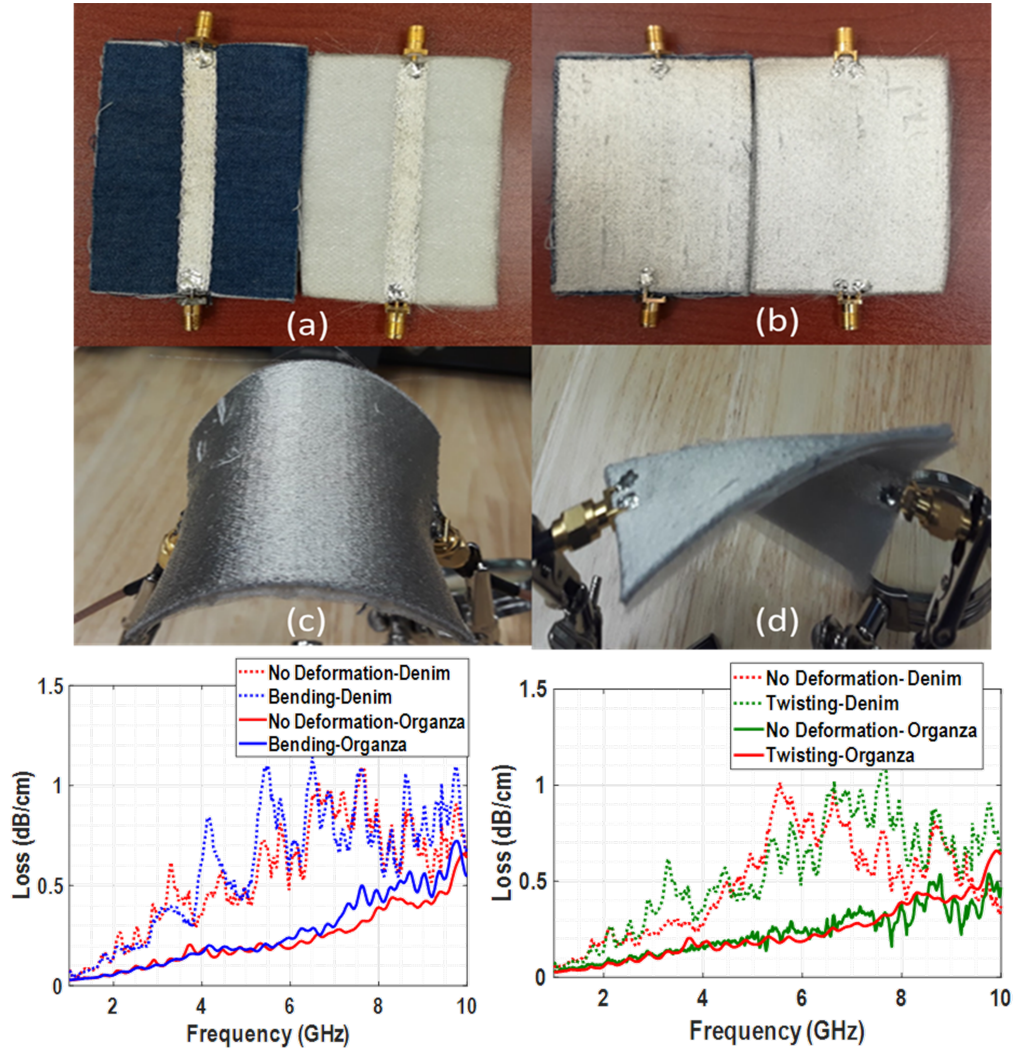
Figure 3.5: Effects of mechanical deformation on the performance of TTLs made of Elektrisola-7 embroidered onto denim
and organza fabrics: (a) finished prototypes, (b) backside of the prototypes, (c) bending process of the samples, (d) twisting process of the samples, Bottom (left): loss performance due to bending, and Bottom (right): loss performance due to twisting.

of its microstructure. As can be seen in Fig. 3.6 (b), the microstructure of organza is composed of an arrya of small grids that offer a smooth interweaving path to the conductive threads and do not store loss-enabling agents like dusts, moisture, etc. The microstructure of denim on the other hand is a cluster of cotton-based compartments that strap environmental stimuli like moisture, dust, and anything
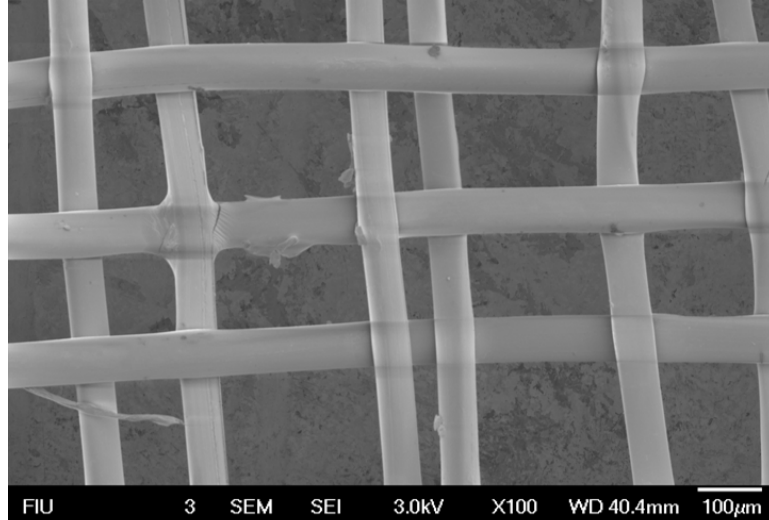
(a)
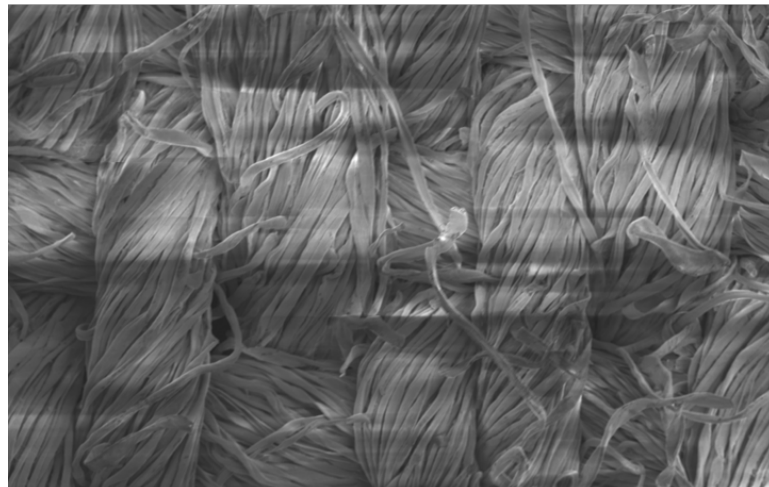
(b)

Figure 3.6: SEM micrographs of (a) denim and (b) organza fabric substrates realized at 3.0 kV, X100, WD 40.4 mm and for a 100-μm scale.

that can compromise the excellent RF performance of the TTLs. As a result, by changing the substrate material from denim to organza, the poss performance of the TTLs can be improved by 0.5 dB/cm. From this point, we have achieved an excellent milestone when it comes to investigating the best design procedure for clothing-integrated RF structures. However, the solder-based interconnections introduced

hard-phases when they are used as contact between the transmission lines and the excitation ports (represented by SMA connectors). In the next sections, we will present and discuss a novel process to ensure the elimination of hard-phases created by the solder balls used while developing the flexible textile TTLs.

3.4   Flexible Epoxy-Based Interconnects for Textile-Integrated RF Modules

To mitigate the issue of hard-phases obtained from soldering the interconnects in the transmission lines, we investigate the substitution of solder balls by ink-based interconnections. We evaluated the loss performance of two textile transmission lines (TTLs) with interconnects made of solder and ink. The TTLs were tested for flexibility, reliability, and the impact associated with their RF performance. Their reliability was tested through the variation in their RF performance after 10 cycles of bending. To validate the proof-of-concept, we develop two 7-element textile Yagi-Uda antennas where the SMA connectors are attached to the antennas via solder-based and ink-based interconnects. Below, the details about this study is presented and discussed.

3.4.1   Loss Comparison for Textile TLs (TTLs)

Excellent RF performance of IoT devices requires a very distinct design process. The latter involves the selection of various parameters that include the material for conductive surfaces and interconnects. Several materials have been used before for conductive surfaces and others are proven to be good for interconnects. Below, a concise summary of these parameters is presented:
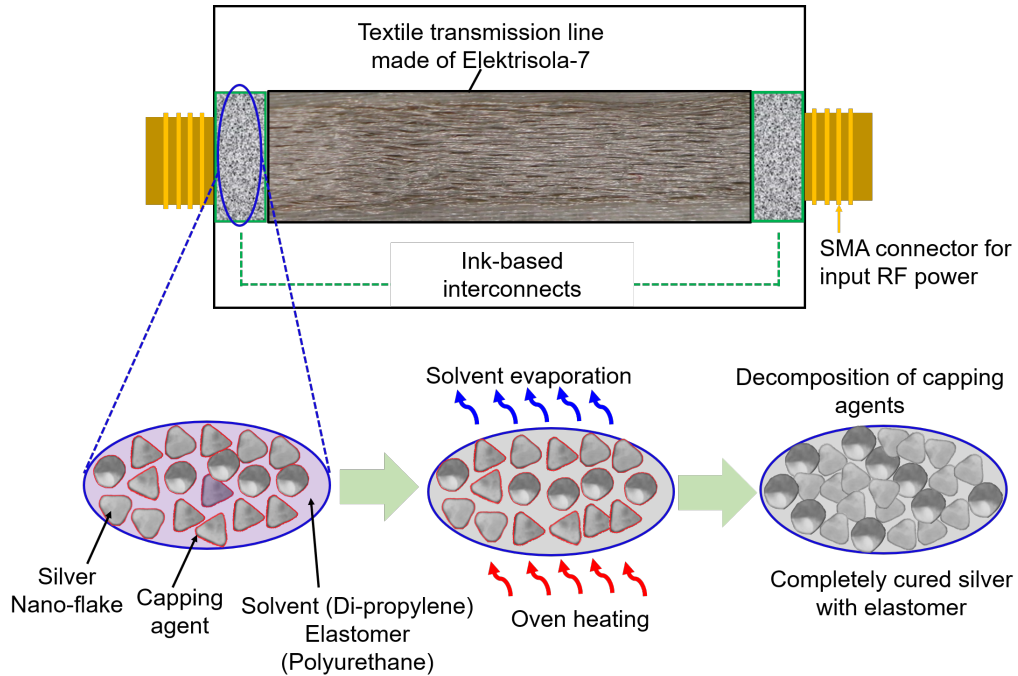
Figure 3.7: Microstructure shown in the cross section area of an ink-based interconnects with all elements involved as well as a closer look at the interconnect when subject to the curing process.

1. **Textile: conductive threads (E-fibers)**

    (a) Shieldtex silver-plated polyamide thread (234/34-2 ply HCB)

      Pros: sheet resistivity $100\Omega/$m

      Cons: thick thread, limited resolution

    (b) Elektrisola-7 (silver-coated copper)

      Pros: improved resistivity $0.0171\Omega/$m, good RF conductivity (2.44×10^6 S/m, fully flexible, suitable for RF applications, resilient to mechanical deformations (bending and twisting [74])

      Cons: No elastomer used

2. **Conductive printed ink: silver nanoparticles with or without polymeric binder**

30

(a) JS-A211 (Novacentrix)

Pros: easy to print on TPU, PET, polycarbonate

Cons: direct printing on fabrics (e.g. denim, organza), too small to properly saturate/coat the textile fibers, vulnerable to mechanical deformations.

3. **Conductive Epoxy: silver with polymer binder**

(a) nanoparticles

Pros: ink-jet printing, fast sintering, R2R, volume resistivity :$< 3.1 \times 10^{-5}\Omega/m^3$

Cons: cannot withstand repetitive mechanical deformations, not flexible (generate cracks under deformations) when used in hard-to-soft interconnections.

(b) nanoflakes (CreativeMaterials 127-48)

Pros: volume resistivity: $6.5 \times 10^{-5}\Omega/cm$, 82% of silver when cured [75], excellent crease resistance, excellent adhesion with fabrics, good to replace solder in crack-free interconnects, fully flexible, good for hard-to-soft and soft-to-soft interconnections, suitable for RF applications in printed circuits, and washable textiles.

Cons: conductivity improves with high curing temperature like 125°C.

(c) nanowires

Pros: superior conductivity under strain,very low solid content to offer flexibility

Cons: nothing noticeable

Conductive E-threads, according to the above summary, have been proven to have excellent RF performance [76]. The latter is a result from optimization of the

stitching pattern, the tension and the thread density of Elektrisola-7 embroidered onto fabric-substrates. We fabricated four 11-cm long textile-based transmission lines via automated embroidery of Elektrisola-7 onto organza substrate ($\epsilon_r = 2.75$ and $\tan\delta = 0.0015$) A sheet of copper tape was applied to the back of the embroidered surface to play the role of ground plane. For loss comparison, SMA connectors
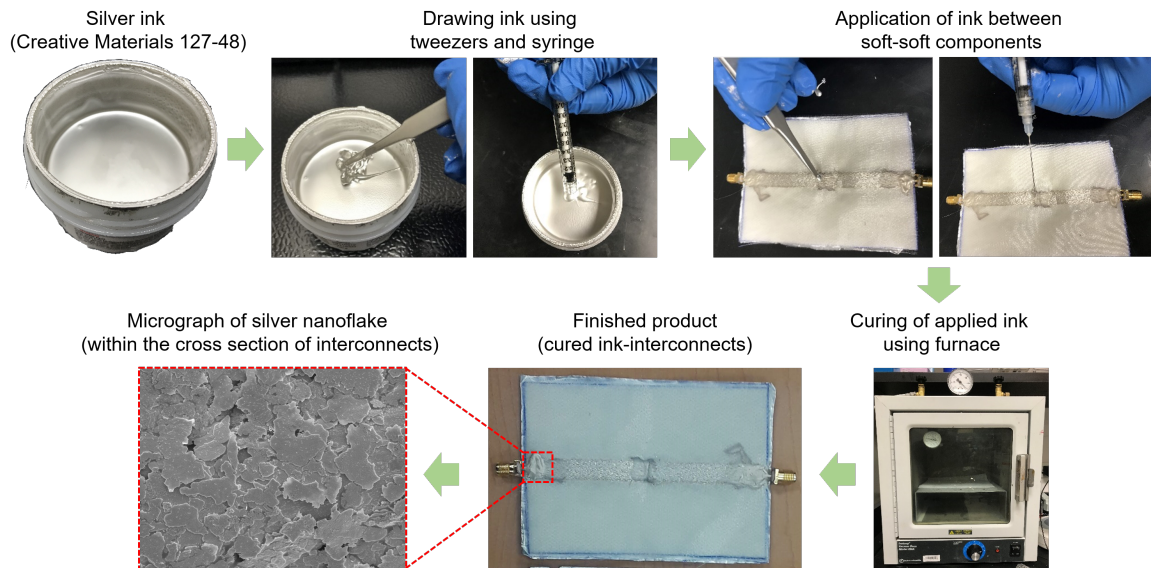
Figure 3.8: Steps involved in the curing process of the ink-based interconnects from the fresh ink to the fully cured interconnects for a textile RF transmission line.

were connected onto the TTLs using solder alloy and CM 127-48 (made of nano-flakes) (see Fig. 3.9) from CreativeMaterials. The ink-based samples were drawn using tweezers and syringe, then applied to the contacts between the transmission lines and SMA (see Fig. 3.8). As per the vendor's recommendation, the ink-based interconnects were cured for 60 minutes at 110 °C in a vacuum oven (Fisher Scientific 280A) for optimum conductivity (see Figs. 3.7 and 3.8). After curing, the samples were settled for one day and a Keysight PNA N5222B vector network analyzer was used to characterize their connection losses that were later compared with their solder-based counterparts.
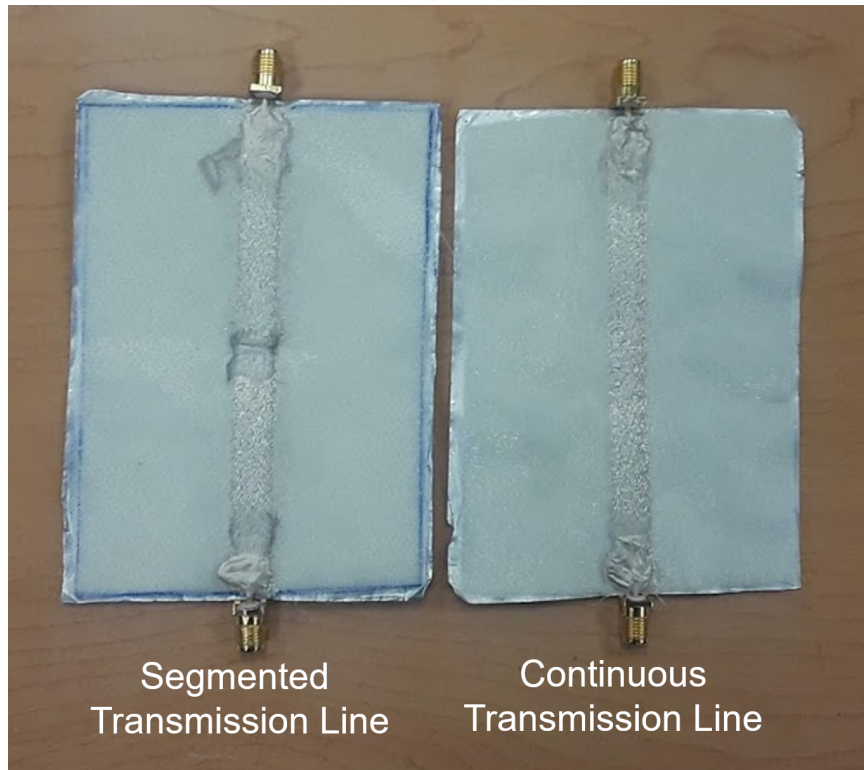
Figure 3.9: Finished prototypes of the ink-based transmission lines (left) segmented transmission line and (right) continuous transmission line.

The loss performance was evaluated using the formula in [77] for all four samples.

In the case of the continuous (non-segmented) TTLs, the results suggest a maximum connection loss of 0.15 dB/cm and 0.23 dB/cm for ink-based and solder-based interconnects, respectively.

As a result, the ink-based exhibit 50% less loss than their solder-based counterparts. For the segmented TTLs, a connection loss of 0.15 dB/cm and 0.35 dB/cm for ink-based and solder-based TTLs, respectively. This is the equivalent of more than 50% improvement in connection loss for ink-based interconnects over those of solder. In the case of continuous and segmented TTLs made of ink-based contacts, the loss exhibited when they undergo bending was found to be 0.1 dB/cm due to the fact that when bending, the epoxy/ink is able to stretch and eventually put in
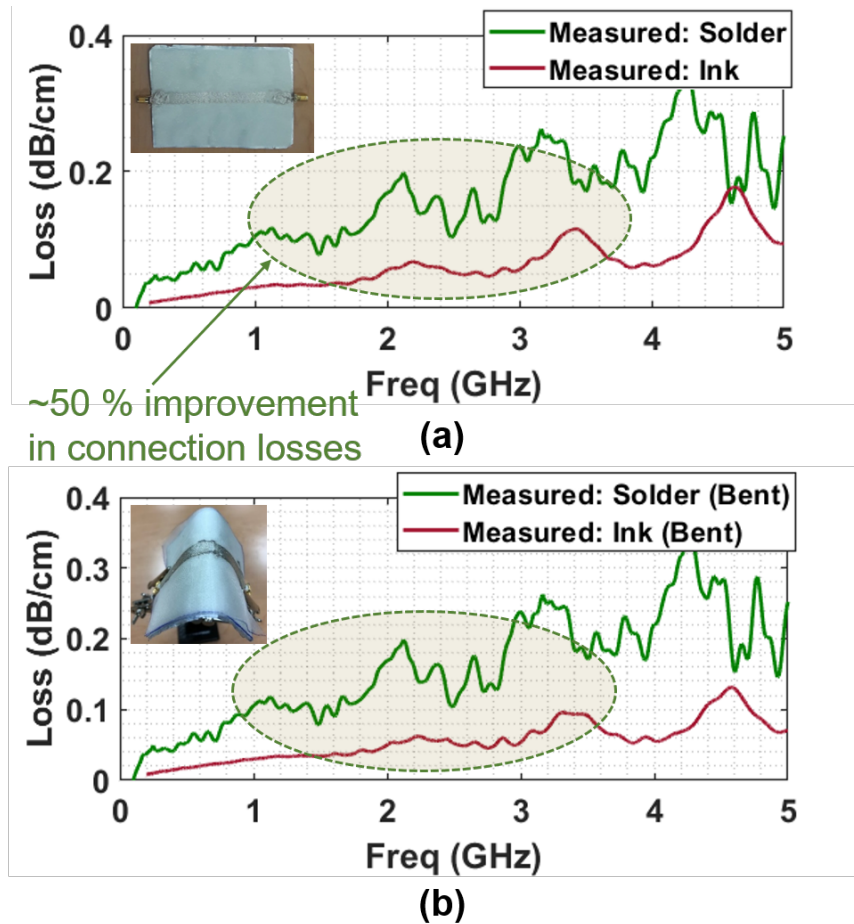
Figure 3.10: Evaluation of connection losses in textile-based continuous transmission lines when the interconnects are made with ink and solder when (a) no mechanical deformation is considered and (b) bending the structure.

contact some threads that might not have been in contact before the bending. The latter also holds true for the case of improvement in connection loss for ink-based interconnects in comparison with their solder-based counterparts.

The micrographs of both solder-based and ink-based interconnects are reported in Fig. 3.12. As suggested from Fig. 3.12, voids are created within the solder-based surfaces, which compromise the conductivity of the TTL (Fig. 3.12 (a)). In the case of ink-based, however, the epoxy infiltrates within the conductive surfaces of the TTL , which makes perfect contact with the threads and optimizes the conductivity

(Fig. 3.12 (b)). The effect of bending on the RF performance was also evaluated for reliability. The reliability test was performed for 10 cycles of bending. After undergoing these mechanical deformations, the samples remained crack-free due to the fact that the cured epoxy has 82% of silver [75] that keep their conductivity while being spread in the elastomer. In conclusion, epoxy/ink is the best option to realize flexible and reliable interconnections as it easily percolates the conductive surfaces made of E-threads.
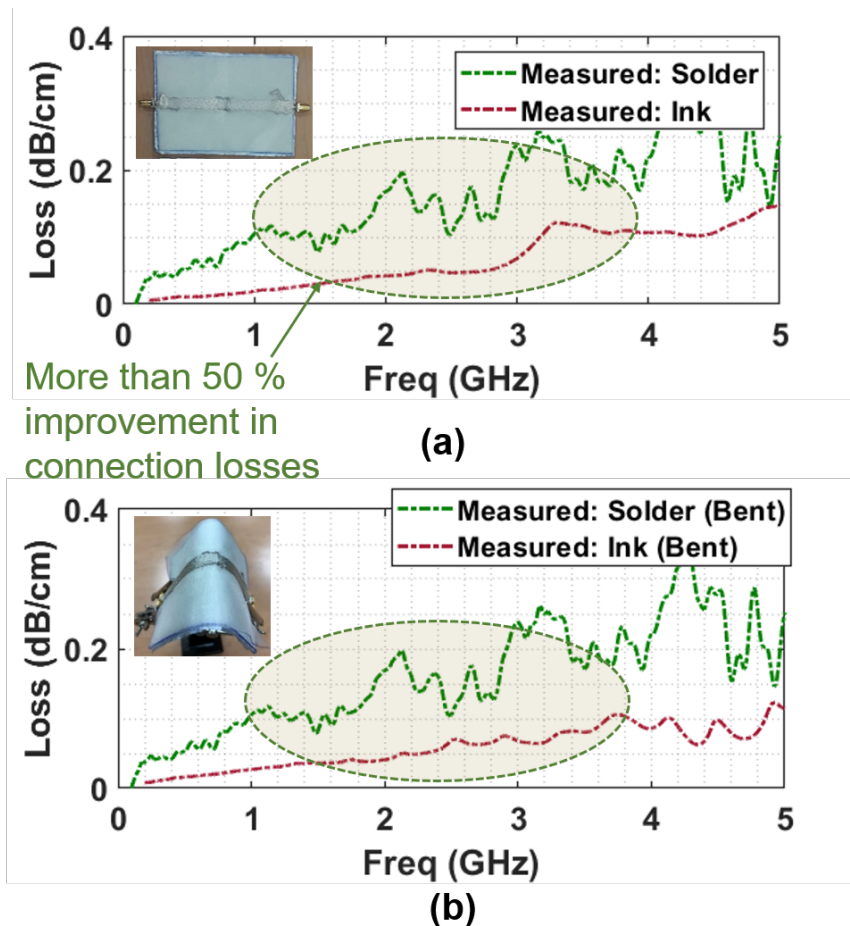
Figure 3.11: Evaluation of connection losses in textile-based segmented transmission lines when the interconnects are made with ink and solder when (a) no mechanical deformation is considered and (b) bending the structure.
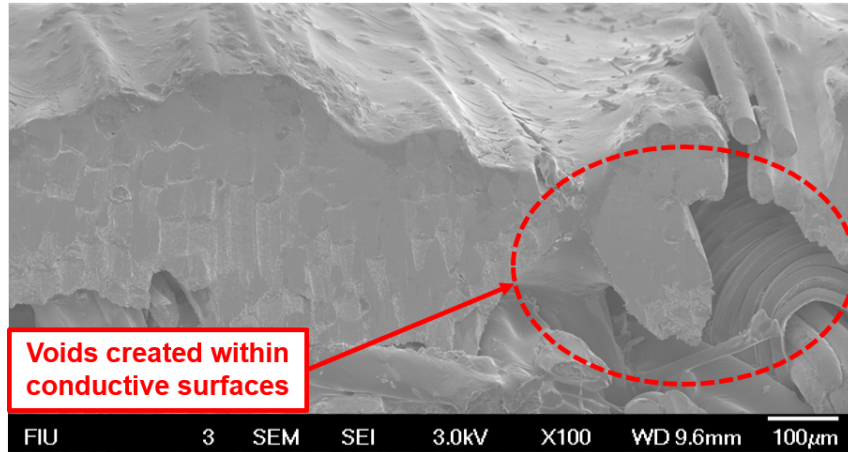
(a)
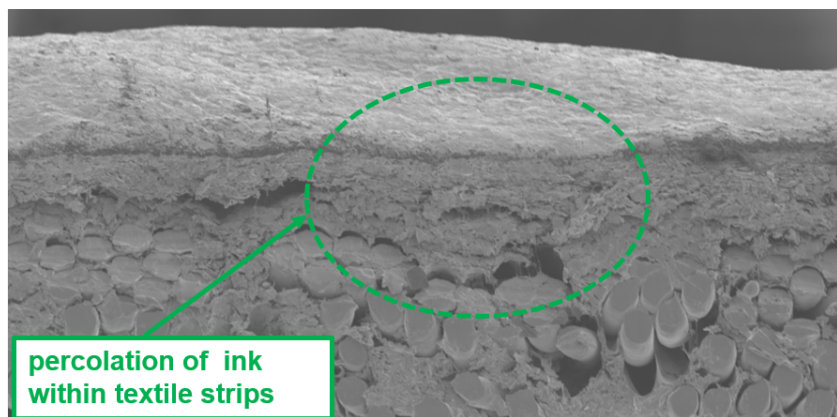
(b)

Figure 3.12: Micrograph of the cross sections of both (a) solder-based and (b) ink-based interconnects after a full curing cycle.

3.4.2   Textile-Based Yagi-Uda Antenna

To validate the aforementioned results for antenna applications, we designed and fabricated a 7-element textile Yagi-Uda antenna to operate at 2.45 GHz. The design was optimized according to [77, 74]. The antenna was designed and optimized using full wave FEM solver, HFSS and prototyped via automated embroidery of Elektrisola-7 onto denim ($\epsilon_r = 1.67$ and $tan\delta = 0.07$). The reflection coefficient and realized gain of the antenna were measured using a Keysight PNA N5222B vector

network analyzer and near field STARLAB anechoic chamber from the RFCOMLab and TAC/FIU, respectively. We simulated and tested the reflection coefficient and
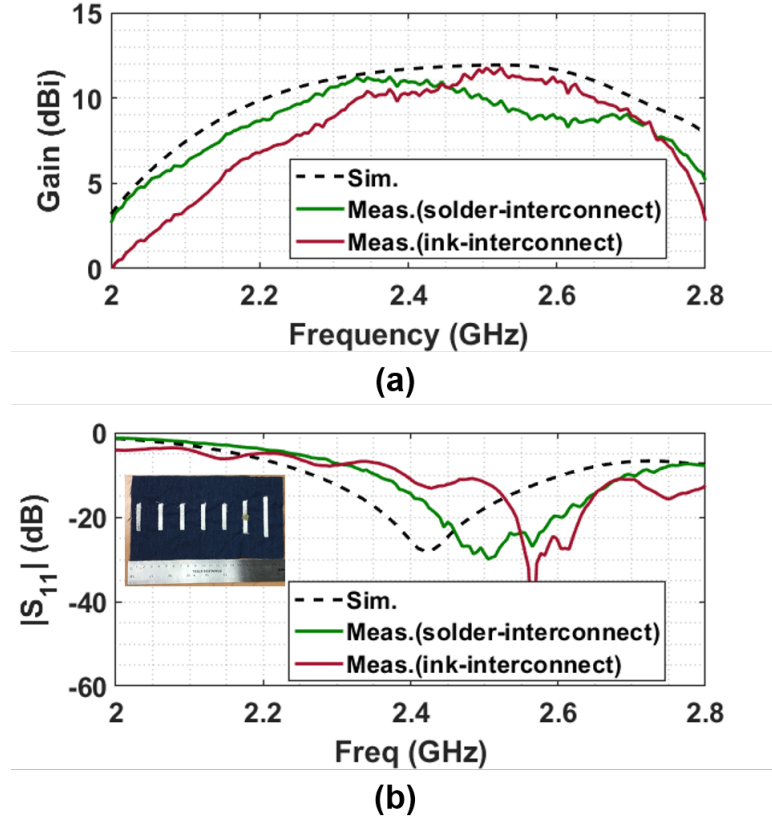
Figure 3.13: RF performance of a textile-based 7-element Yagi-Uda antenna with interconnects made of ink and solder: a) S_{11} and b) Gain

the realized gain of the 7-element textile Yagi-Uda. The results from Fig. 3.13(a) and (b) suggest that the antenna made of ink-based interconnects showed an $|S_{11}|$ = -16 dB at around 2.45 GHz and its realized gain was 11 dBi. These results show reasonable agreement with the simulated results. For the solder-based interconnects, however, the measured $|S_{11}|$ turned out to be -20 dB and the realized gain, 10 dBi. Using epoxy/ink-based interconnects is therefore more advantageous than those of solder. Therefore, the development of textile RF structures can be improved by

utilizing ink/epoxy-based interconnects necessary to establish contacts during soft-to-soft and hard-to-soft transitions.

3.5   Conclusion

In this chapter, we propose the study of the effects of embroidery techniques and interconnects on the RF performance of the textile RF modules. This study consisted of the embroidery patterns [fill-stitches], the materials used for embroidery, and the interconnections between the embroidery pieces of conductive lines and the connections to the equipment used for measurements. The results on embroidery patterns suggested that when the conductive threads are embroidered in the direction of the RF current, the textile modules [transmission lines in this case] exhibit the smallest insertion loss. In addition, the study pointed out that using 14threads/mm, the mechanical deformations [like bending and twisting] do not have any effects on the RF performance of the developed RF modules. The best fabric substrate reported to be choose for embroidery is the one that is made of grids where external agents like dust and moisture will not be stored-these agents contribute significantly to the loss exhibited during the RF testing of the modules. To assure excellent soft-to-soft and hard-to-soft transitions,the study suggested the use of CreativeMaterials 127-48, which is an epoxy/ink that exhibited less loss than its solder counterpart. This result can be used as a guidelines for future wearable RF modules where flexibility will be of great interest.

CHAPTER 4

FAR-FIELD FABRIC-INTEGRATED WIRELESS POWER TRANSFER AND HARVESTING FOR WEARABLES

4.1 Introduction

Integration of the wireless charging platform on clothing is enabled by the proposed embroidery processes. At the same time, it is hypothesized that clothing surfaces an allow larger power collection due to larger surface available area. We consider the integration of antenna array and rectifiers for far-field power collection in this chapter. In effect, the goal of implementing a novel RF harvesting jacket is realized.

We begin with the design, simulation, and fabrication of a textile-based single patch antenna made from the Elektrisola-7 thread embroidered onto organza. This is followed by the design, simulation, and fabrication of a single-diode rectifying circuit resonating at the same frequency. Later, both antenna and rectifying circuit were combined into a 2×2 and 2×3 rectenna arrays for power transfer and harvesting. Our rectifier is distinct from other published rectifiers since (1) it features a single-diode topology for the rectifier circuit to achieve an RF-to-DC efficiency of
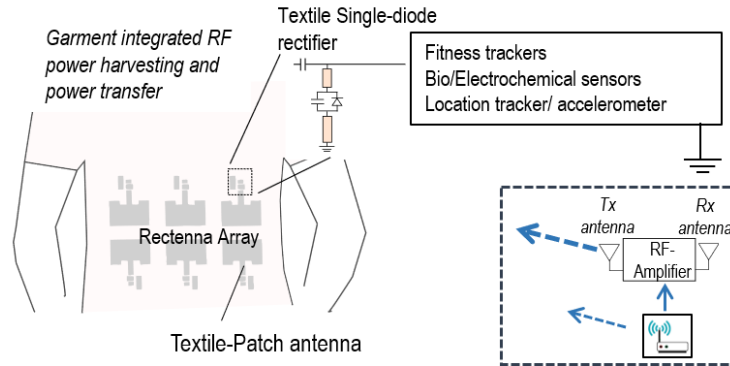
Figure 4.1: Wireless power harvesting system comprising of :(Bottom) Wi-Fi router, (Left) rectenna array, and (Top-right) various wearable applications

70% at 8dBm and (2) does not use an management circuit. The design-optimization and fabrication process of the rectifying circuit was precisely controlled to avoid sacrificing the conversion efficiency. In this chapter we also report the performance of the 2×2 rectenna array in a realistic Wi-Fi environment and the 2×3 rectenna array, by amplifying the available Wi-Fi signals and then harvest them. In effect, we proposed and tested the large area and fully flexible arrays of RF-power transfer and harvesting rectennas (see Fig. 4.1). This system uses automated embroidery of Elektrisola-7 thread onto organza fabric. As a result, the prototyped structure is robust, flexible and washable. In past works, several other flexible-electronics approaches have been demonstrated for power transfer and harvesting. These include conductive tapes [78, 79, 80], screen printing and inkjet-printing [81, 82], liquid metal alloy [83], along with conductive textiles known as E-threads [25, 84, 28, 85] and/or metallized fabrics [86, 87] In the next sections, a complete design, simulation, and fabrication of the full system is presented and discussed.

4.2 Conductive Thread Embroidery-Based Fabrication of Patch Antenna

The steps involved in the fabrication process are shown in Fig. 4.2. The conductive surfaces are mad of Elektrisola-7 and optimized via circuit or full-wave simulations and then are converted to respective CAD models. The CAD-models are then imported to a $Brother^{TM}$ Innovis VM5100 embroidery software, where a pattern of needle-paths (digitization of the CAD model) is generated for the embroidery process.

The digitized model is then fed to the automated embroidery machine for fabrication. The conductive surfaces are generated using automated embroidery of
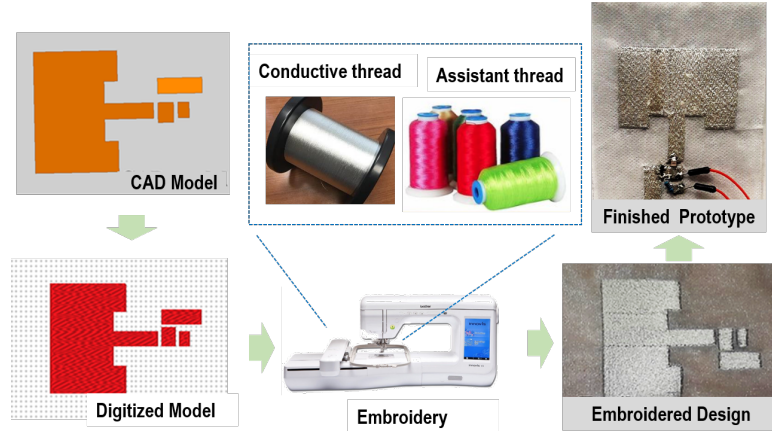
Figure 4.2: Steps involved in the fabrication of the conductive thread-based RF circuits and antennas from the optimized CAD models

E-threads (Elektrisola-7) on a regular cloth and a second layer of textile embroidery is used to implement the ground plane as shown in Fig. 4.3(a). In this work, Elektrisola-7 (supplied by vendor Elektrisola, www.elektrisola.com), consisting of silver-coated copper strands (Cu/Ag50 amalgam), was used to built the conductive interfaces of the RF modules used in the study. In past works, conductive surfaces made of this particular thread have demonstrated loss performances in the same order as observed in rigid substrates (or PCBs) where copper is cladded on the substrates for maximum conductivity [88, 84, 89]. For low conductive losses and maintaining the flexibility of cloth after embroidery, three related parameters are taking into consideration. These are stitching density (number of threads per unit length, stitching pattern (the alignment of the embroidered threads with respect to the direction of the RF current), and thread tension (the precision about how much the top and bottom threads have to pull each other in order to realize a smooth embroidery on both sides of the seam while avoiding thread breakage). As expected, high thread density is required for high conductivity. Therefore, the highest possible stitching density of 14 threads per mm was used in the embroidery. By using this
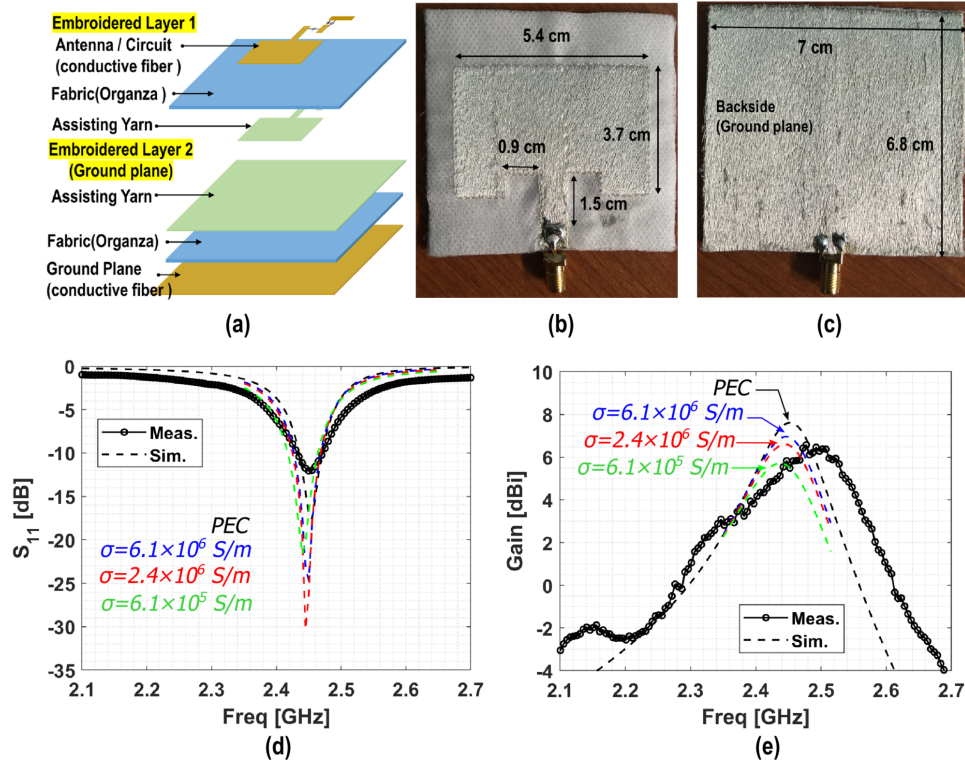
Figure 4.3: 2.45 GHz patch antenna made from conductive threads embroidered onto fabric substrate. (a) Exploded view of various layers used in the design (b) top front view of the patch antenna b) ground plane view of the antenna (c) measured and simulated (Ansys HFSS) return loss coefficient, and (d) realized gain as measured and simulated (Ansys HFSS) in the broadside direction.

optima thread density, we envision a compensation of the full conductivity when the structure is subject to mechanical deformations that force the threads to fray away from one another.In addition, stitching patterns have been known to impact the conductivity of RF structures. Selected stitching patterns were optimized to align the threads in the direction of RF current. In a prior work, such alignment is shown to have minimized losses in transmission lines to approximately 0.3 dB/cm for frequencies up to 3.5 GHz [88]. Finally, thread tension was controlled to ensure the highest possible precision without damaging the threads to maintain continuous

conductive surfaces. For this matter, we chose a thread tension setting of 4 (out of available scale of 0 to 9) for our application.

4.2.1 Antenna Design, Prototype and Measurements

A rectangular patch antenna was considered as per [90], but a crucial unknown was the dielectric constant of the textile substrate that was at the time, unknown. In order to find the dielectric constant, we measured the resonant frequency (f_r for a wavelength λ_r) of several patch antennas with varying lengths (l) that were made using organza and (sticky) stabilizer substrate onto which conductive surfaces were embroidered. By using the relation $l = \lambda_r/(2\sqrt{\epsilon_r})$, the effective dielectric constant of the fabric substrate was estimated as ϵ_r=2.75. The effect of fringing fields was ignored in this estimation due to small thickness of the substrate ($\approx$1.5 mm). Using this information, the length of the patch was determined to be $l = \lambda/(2\sqrt{\epsilon_r}) \approx$3.7 cm for 2.45 GHz operation. Other dimensions, shown in Fig. 4.3(b) and (c), were appropriately optimized using full-wave simulations to achieve a desired S_{11} bandwidth.

Based on previous conductivity studies[76], it was found that conductive surfaces can be modeled using perfect electrical conductor (PEC) model during design's optimization. This behavior can be understood by considering the nature of conductive thread. At 2.45 GHz, considering copper (conductivity as σ=5.95 $\times 10^7$ / Ωm) as conductive material, the corresponding skin depth ($\delta = (\rho/(\pi f_0 \mu_r \mu_0))$) was found to be 1.32 μm. Compared to this, the diameter of a single thread is 280 μm, which is the equivalent of 210 skin depths. Considering this calculation, we predict that the skin-depth effects are not dominant, and for design purposes the embroidered surfaces can be treated as PEC. As depicted in Fig. 4.3(d) and (e), the measured

gain and S_{11} agree well with simulated results. Specifically, the S_{11} curve shows a resonance at 2.45 GHz and impedance matching in the Wi-Fi band. The antenna exhibited a maximum gain of 6.5 dBi at 2.47 GHz in the broadside direction, with a gain-frequency profile closely following the simulated one. Next, we pursue efficiency calculations for the fabricated antenna. For reference, we consider the simulation model with PEC conductive surfaces and no dielectric loss which shows 100% radiation efficiency and 98.2% total efficiency which includes the losses due to impedance mismatch. That is, the total efficiency (e_t) and radiation efficiency (e_r) are related by the reflection coefficient S_{11}, as

$$e_t = e_r(1 - |S_{11}|^2) \tag{4.1}$$

Since simulation model uses PEC surfaces and lossless dielectric materials, $e_r = 100\%$ and $e_t = 98.3\%$ for $S_{11} = -17.59$ dB at 2.45 GHz. Assuming measured and simulated directivities of the antenna are identical, reduction is gain from simulation to measurements is due to added conductor losses, dielectric losses and additional mismatch losses. Therefore, total measured efficiency of the prototype is calculated using

$$e_{tm} = e_t \times 10^{(G_{pm}/10)}/10^{(G_{ps}/10)}, \tag{4.2}$$

where $G_{pm} = 6.57$ dBi and $G_{ps} = 7.61$ dBi are the measured and simulated peak gains respectively. Furthermore, measured radiation efficiency (e_{rm}) is estimated by removing the mismatch losses that were observed in the measurements, as

$$e_{rm} = e_{tm}/(1 - |S_{11m}|^2), \tag{4.3}$$

where suffix S_{11m} refers to measured reflection coefficient.. Comparing peak gain from this simulation, i.e. 7.61 dBi, with measured peak gain of 6.57 dBi, we calculate the total measured efficiency (e_{tm}) of the fabricated antenna as $e_{tm} = 77.3\%$. e_{tm}

takes into account all forms of losses, i.e. dielectric losses, conductive losses as well as mismatch losses at the antenna port. From the knowledge of measured mismatch losses, we also calculate the measured radiation efficiency (which includes only dielectric and conductive losses) of the antenna to be e_{rm} =89.1%.

The differences in measured and simulated gain can be used to estimate the conductivity of the fabricated conductive surfaces. To achieve the latter, we model the antenna with varying conductivity values of conductive surfaces as shown in Fig. 4.3(d) and (e). Assuming that dielectric losses are small and can be neglected, conductivity of the embroidered surface accounts for all losses in the antenna. In Fig. 4.3(e), the peak gain for the case with $\sigma = 2.4 \times 10^6$ S/m matches the peak measured gain, suggesting that fabricated surfaces should have conductivity $\sigma = 2.4 \times 10^6$ S/m or better. In reality, this value should be slightly higher, since mismatch losses are higher in the measured prototype, therefore conductor losses are overestimated in this conductivity comparison. Nevertheless, this analysis provides an approximate value of the effective conductivity of the developed embroidered surfaces.

The effects of the human body on the performance of the textile antenna were investigated using full-wave modeling of the antenna in presence of human body (Fig. 4.4(a) and (b)). The electrical properties of different layers used in the simulation are provided in Table 4.1. The mass-densities of the layers of skin, fat, and muscle were chosen as ρ=1.02 g/cm^3, 0.9094 g/cm^3, and 1.059925 g/cm^3, respectively. A small area with mass of 0.2 kg per layer was chosen for this study. The measurement setup was realized in accordance to [91]. The antenna was placed at a representative distance of 5 mm ($\approx \lambda/25$) from the human body, although this distance could be variable. The gain and S_{11} results (Fig. 4.4(c) and (d)) suggest that the antenna performance was not affected due to field interactions with the human body. This is primarily because of the ground plane, which provides isolation between the antenna

Table 4.1: Electrical properties of the layers in human body simulation

Layer	Thickness (mm)	Dielectric const. ϵ_r	Bulk cond. σ (S/m)
Skin	5	38	1.46
Fat	7	5.3	0.11
Muscle	30	52.7	1.77

*A spacing of 5 mm between the ground plane and the human model was considered.
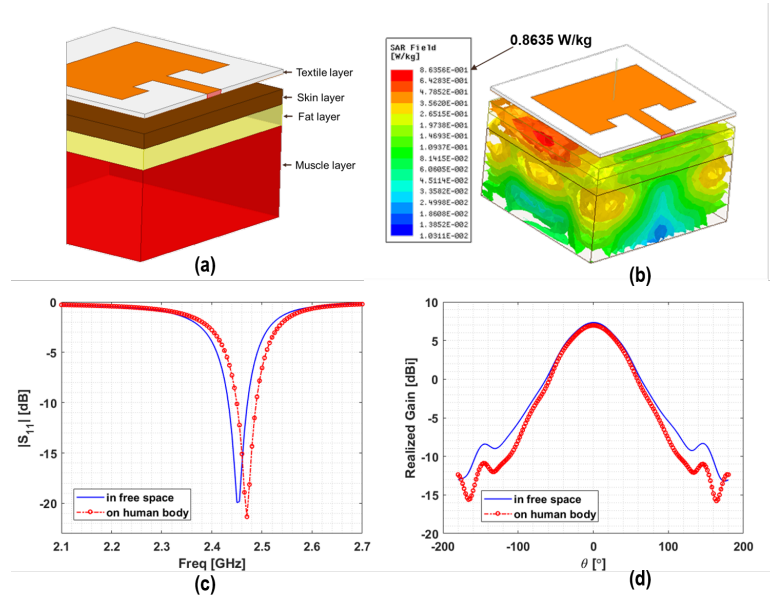
Figure 4.4: Effects of the human body on the performance of the textile antenna. a) different layers considered for the simulation setup, b) average SAR found to be 0.8635 W/kg when 1 W of power was used, c) simulated S_{11}, and b) realized gain of the textile-based antenna when exposed in air and mounted on human body.

and the human body. Simulations also show that surface absorption rate (SAR) was limited within a maximum of 0.87 W/kg, which in accordance with the limit of 1.6 W/kg as per IEEE standard C95.1-2005 for safety levels with human exposure [92].

4.3 Textile-Based Single-Diode Rectifier in Wearable Applications

4.3.1 Rectifier Design, Prototype and Measurements

Fig. 4.5 depicts the rectifier circuit prototype and measured performances. Achieving high efficiencies at low input power levels (below 0 dBm) and using minimal circuitry is a primary challenge for this design. The operation of single-diode rectifier involves use of resonant transmission line which is shorted at one end. The position of the diode is optimized by tuning the lengths L_1 and L_2 to increase the efficiency. The idea is to utilize the power stored in a standing wave, which causes higher voltage across diode terminals. As expected, the standing wave amplitude could be up to twice of the propagating wave (full rectification). This allowed us to achieve RF-DC conversion efficiency of 70%, which is greater than the 50% limit of single-diode half-wave rectifiers. Furthermore, the capacitors C_1 and C_2 were added and optimized for impedance matching with incoming RF and the rectifying diode. There is fair agreement between the simulated and the measured rectifier

Table 4.2: Lumped component values placed in the rectifier circuit

C_1	2 pF	Matching at 2.45 GHz
C_2	0.4 pF	Matching at 2.45 GHz
R	1 kΩ	Representative of a typical load
L_1	18 mm	Matching at 2.45 GHz and efficiency optimization
L_2	6 mm	Matching at 2.45 GHz and efficiency optimization

efficiency for input power level less than 0 dBm (see Fig. 4.5). But, the measured results deviate for input power levels greater than 0 dBm. This deviation is a known phenomenon among single diode rectifiers as also noted in [29], and is due to the

non-linear behavior of the diode. Since a linear RC model was used in ADS circuit simulations, we observe deviations between the simulated and the measured data. This is due to the fact that a linear model was used to design the rectifying circuit, which in reality, should be non-linear.
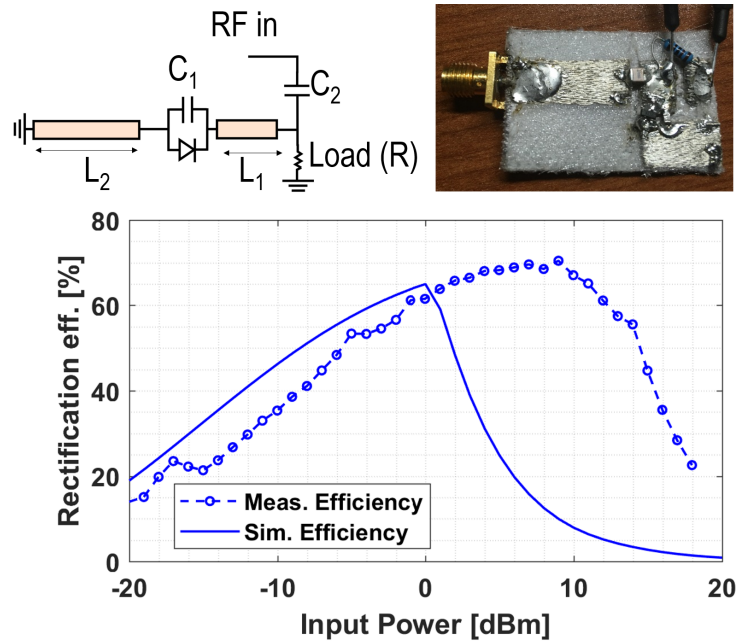
Figure 4.5: Textile-based, wearable rectifier using conductive embroidery onto organza substrate. Left, top: Schematic of the rectifying circuit using single-diode topology. Left, Bottom: fabricated prototype on organza-based clothing material, Right: Measurement and simulated (Keysight ADS) efficiency at 2.45 GHz.

The rectifying diode is a crucial component of the harvester (rectifying circuit) and must exhibit low turn-on voltage and low-leakage current to achieve high RF-to-DC conversion efficiency. In general diodes must provide a compromise between these quantities. In this regard, Schottky diodes provide a good compromise due to smaller turn on voltage [93, 94, 95] and their ability to rectify low input RF signals without requirement of a significant biased voltage. For our design, the Skyworks SMS7630 Schottky diode was selected. A comparison of the proposed rectifier to some recent rectifiers is shown in Table 4.3. Our design achieved close to 20%

Table 4.3: Efficiency-comparison of the textile rectifier circuit with recent publications

Input Power (dBm)	Efficiency (%)	Rectifying Diode	Reference
-20, 8	18, 70	SMS7630	This work
-13.3	2	SMS7630	[96]
-13	9	SMS7630	[97]
-20.4	10.5	SMS7630	[98]
10	53	HSMS2852	[99]
-20, 3	1, 45	HSMS2860	[100]
-20, 8	2, 73	HSMS2860	[101]

efficiency at -20 dBm input power. By comparison, earlier designs [98, 100, 101] show 10.5%, 2% ad 1% efficiency, respectively. Specifically, our circuit showed an RF-to-DC rectification efficiency between 20% and 60% for input-power level varying from -20 dBm to 0 dBm and this is in close agreement with the simulations. This textile-rectifier is used to be combined with the previous discussed antenna to realize an array of rectennas for power transfer and harvesting. The full details are reported in the next sections.

4.4 Design and Optimization of Textile Rectenna Array

4.4.1 Textile Array Design and Fabrication

Using the rectifier and patch antennas optimized and tested in previous sections, rectenna elements were fabricated (see Finished Prototype in Fig. 4.2). The elements were then used to fabricate 2×2 and 2×3 arrays as shown in Figs. 4.8 to 4.9. The inter-element distance in each of the arrays was chosen to be 8.5 cm in horizontal and 5.5 cm in vertical directions. This choice was based on ease of fabrication, but further optimization could be pursued to increase area density for optimal power

collection. Overall, the 2×2 and 2×3 arrays occupied an area of 300 cm^2 and 437 cm^2, respectively.
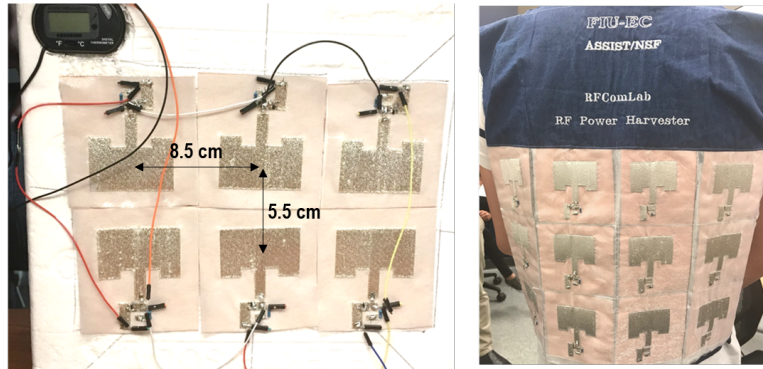
Figure 4.6: Photographs of the 6-element prototype array used for the RF-harvesting measurements. Right: photograph of full-scale jacket with power harvesters demonstrating the wearability.

Prior to testing the developed arrays, we characterized the available ambient RF power. The test results are presented in the next section.

4.5 RF-Power Availability Tests

Ambient RF power measurement was conducted using a low-gain, broadband spiral antenna with 2.4 dBi gain at 2.45 GHz. The antenna was placed at 20 cm from the radiating device (Wi-Fi router or phone) and was connected to a Keysight PXA N9030B Signal Analyzer to record the power-frequency spectrum. Peaks were observed in the spectrum at 700 MHz, 830 MHz and 2.4 GHz. Tables 4.4 and 4.5 summarize the peak power observed from a cell-phone and a Wi-Fi router, respectively.

Table 4.4 shows the emitted peak-power from a cell-phone at frequencies 700 MHz, 830 MHz (LTE bands) and 2.4 GHz (Wi-Fi band), when a voice or a video call was in session. As noted, the maximum power level of 1.5 dBm was recorded at

Table 4.4: Recorded power levels of the ambient RF signal (20 cm from respective devices)

Frequency	Voice calls	Video-Call	Ambient
700 MHz	1.5 dBm	0 dBm	-52 dBm
830 MHz	-22 dBm	-7.3 dBm	-60 dBm
2.4 GHz	-27 dBm*	-22.4 dBm*	-60 dBm

*Wi-Fi-enabled call

700 MHz during the video call. For a Wi-Fi enabled video call, a peak emission of -22 dBm was observed from the cell-phone. Likewise, emissions from Wi-Fi router are shown in Table 4.5. Emissions at 2.4 GHz during a Wi-Fi audio call and Wi-Fi video call were recorded to be -17 dBm and -11 dBm, respectively.

Table 4.5: Peak RF power level measured from a Wi-Fi-Router

Frequency	Audio calls	Video-Call/Streaming	Ambient
2.4 GHz	-17 dBm	-11 dBm	-60 dBm

*The Wi-Fi router used was a Kasda AC 1200M Dual Band KW6515 and the phone was an Iphone 6S

The measurements show that peak power levels of the RF signal could be strong, especially for LTE video calls. Even so, the average values could be smaller. We consider two approaches to attain higher levels: 1) increasing the antenna gain by developing rectenna arrays and 2) boosting the ambient Wi-Fi signal (via amplification) for enhanced power collection. These two approaches are discussed in the next section.

4.6 Power Harvesting Using Textile Rectenna Arrays

To characterize the rectenna array and effect of increasing the number of elements, we investigate the power collected by the single rectenna element, 2×1 rectenna array, and 2×2 rectenna array under dedicated RF signal with continuous sine waveform (see Fig. 4.7). To test the Wi-Fi power harvesting capabilities under ambient Wi-Fi conditions, we also report the power collection using 2×2 and 2×3 rectenna arrays as provided in Fig. 4.8 and 4.9. The rectenna elements of the array were connected in series to combine the harvested power from each antenna. Further, we did not combine the RF power by fear of having to deal with incident waves received at different phases, which could eventually decrease the received power level. For ambient Wi-Fi cases, a Wi-Fi-router at 2.45 GHz was used to stream a video. For the 2×3 rectenna array (Fig. 4.9), we considered the case of amplifying the ambient RF power using a standalone receiver-amplifier-transmitter unit (see Fig. 4.9, inset). The employed amplification unit consisted of a receiver antenna (horn with a gain of 9 dBi), RF-amplifier (mini-circuit coaxial amplifier of gain 30 dB) and re-transmitter antenna (horn with a gain of 9 dBi) and was placed at 5 centimeters away from the Wi-Fi router. The distance between the transmitter horn and the power harvester array was varied as shown in Fig. 4.9.

4.6.1 Measurements and Discussion

First we characterize the rectenna array and the effects of adding more elements on the rectified DC power in Fig. 4.7. The transmitting power (P_t) should be such that when it is output by the transmitter, its equivalent power ($EIRP_{max}$) concentrated into a smaller area by the receiving antenna should be:

$$EIRP_{max} = P_t(dBm) + G_t(dB) - P_g(dB). \tag{4.4}$$

P_t is limited to 30 dBm (1W) and the total EIRP ($EIRP_{max}$), 36 dBm (4W) as per the FCC regulations [102]. P_g is minus 1 for each 3 dB of antenna gain over 6 dB [103]. In this work, 500 mW RF power was transmitted using Agilent N5182A MXG vector signal generator and a minicircuits ZHL-42W+ amplifier connected to a 9 dBi gain horn antenna (Fig. 4.7). The transmitting system corresponds to an EIRP of 4 W (36 dBm), which is in compliance with FCC regulation according to [102, 103]. At 5 ft, single element shows a collection of 25 μW, which is enhanced to 55 μW when four rectenna elements are serially connected. Thus additional power gain is not directly proportional to the number of elements but provides some enhancements. In the future, appropriate serial or parallel power combination architecture should be explored to achieve more robust DC power collection.

In realistic Wi-Fi environment, due to the intermittent nature of the signal (bursty), the collected DC power should be characterized using averaged DC or peak DC power. In practical designs, a power management circuit can be used to account for the intermittent nature of the signal [100, 104]. But for our characterization, we simply conducted peak and averaged DC power measurements using mixed signal oscilloscope (MSO, Keysight MS0S254A) connected to the output of the rectenna arrays. The peak DC voltage (V_p) was recorded using the MSO and then the corresponding peak power (P_p) was calculated using $P_p = V_p^2/R$ where R=5.064 kΩ and R=5.295 kΩ as load resistance values. As a reference, total available RF-power was also calculated by measuring it using a spiral antenna and then extrapolating for a given harvesting area. For calculation of the peak incident RF power, we first used a reference spiral antenna of gain (G) 2.4 dBi connected to spectrum analyzer to record peak RF power (P_{RF}) at 2.4 GHz. Then by using spiral's effective area ($A_e = G\lambda^2/(4\pi)$) , the power density of the incident signal ($S = P_{RF}/A_e$) was calculated. The available peak power RF power incident on the rectenna array

was then calculated by using the array aperture area A as $P_{inc} = S \times A.$, and the corresponding measurements are given by the dashed-curves in Figs. 4.8 and 4.9.

The harvested peak power using 2×2 array was found to be varying between 100 and 0.8 μW as the distance was varied from 10 cm to 150 cm from the Wi-Fi router (Fig. 4.8) when the load resistance of 5.295 kΩ is measured across the terminals of the array. The corresponding DC voltage level was tested to be between 58 mV and 680 mV. These power levels may be considered small for many sensors used in health monitoring applications. Although, with the use supercapacitors, we can store up to nanowatt-level power to operate a wide range of typical sensors.
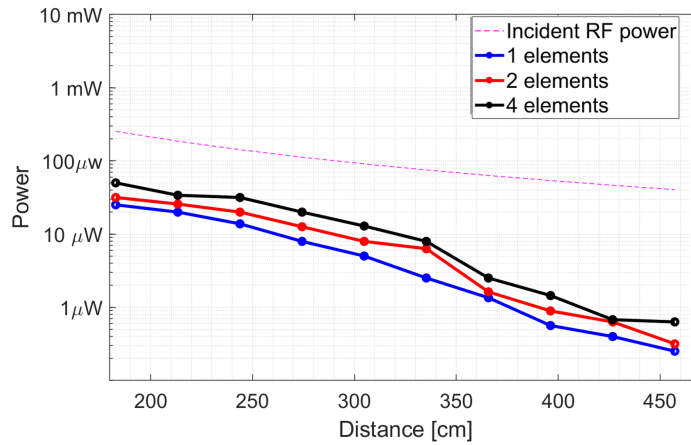
Figure 4.7: Power harvester performance using a 2×2 rectenna array. The average power collected by the 1, 2, and 4-element arrays and corresponding average incident power are shown as a function of distance.

The Wi-Fi signal amplification and collection was conducted using the 2×3 rectenna array. The results are shown in Fig. 4.9. The selected amplifier-unit was effective in increasing the incident power by two orders of magnitude, as shown by the dashed-curve in Fig. 4.9 when compared to dashed-curve in Fig. 4.8. For the 2×3 array case, we report the averaged DC power, where the averaging was done over a period of 10 minutes. As noted in Fig. 4.9, average power levels varied

between 1 to 600 μW as the distance was changed from 160 cm and 10 cm. Specifically at a distance of 60 cm, a DC-power of 80 μW is recorded. Three LEDs were connected in parallel at the output of the array and their lighting is shown for distances up to 60 cm. This means that the collected power levels are quite reasonable for practical applications such as charging super-capacitors or powering sensors for variety of healthcare and IoT type systems [15]-[23]. Notably, LED lighting experiment suggests that no power management circuit is needed to use the proposed harvesting system. Fig. 4.9 also provides rough estimate of total radiated power to
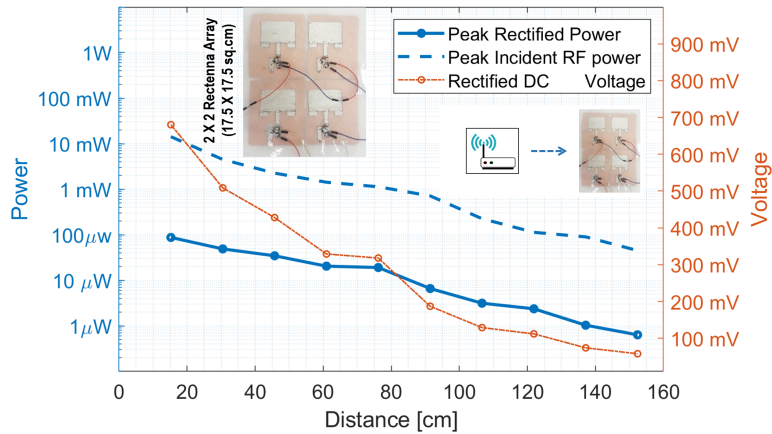
Figure 4.8: Power harvester performance using a 2×2 rectenna array. The DC voltage, its corresponding collected peak power collected by the rectifier circuit and peak incident power are shown as a function of distance.

understand its FCC compliance. As the transmitter antenna was a directive horn and rectenna array was placed at a close distance of 10 cm, most power emitted from the transmitter was received by the rectenna array. Estimated peak power is found to be 1 W for this case as shown in the Fig. 9. We note that average power could be 10 to 100 times lower, as Wi-Fi signal comes in bursts of pulses. This suggests that the shown set-up is compliant with FCC's maximum power limit of 1 W [103].

Many wearable rectennas have been proposed prior to this work [105, 106, 107, 108, 109, 110, 111]. The comparison shows that this work reports the first

embroidery-based textile rectenna system, which is completely integrated on fabric. Furthermore, the use of the embroidery-process and a minimalistic rectifier circuit has allowed us to extend the number of elements to 6, which is the highest reported elements for wearable applications. Thus, we have proposed a method to exploit large clothing areas for RF power-harvesting and power-transfer applications.
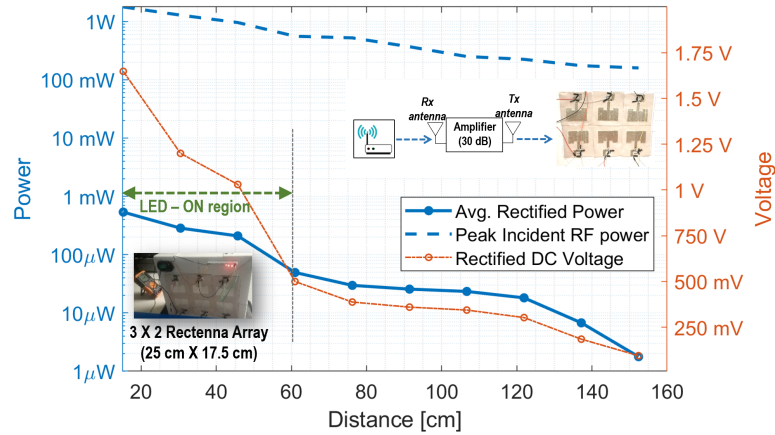
Figure 4.9: Power harvester performance of a 2×3 rectenna array. The DC voltage, its corresponding collected average power collected by the rectifier circuit and peak incident power are shown as a function of distance.

4.6.2 Potential Applications

The clothing-integrated RF-power harvesting circuitry onto textile substrates (see Fig. 4.6) comes with several advantages such as flexibility, comfort, lightweight and durability.Such advantages are contingent to the controlled design and fabrication processes. These attributes make it useful for the wearable electronics in defense and space applications, where it can be used to integrate communication interfaces and sensing tactical gears for dismounted personnel and sensor-enabled space suits for space explorers. Within healthcare and general fitness applications, there is interest for smart-wear with fitness devices. In childcare, they apply to smart garments

for sleep monitoring and location tracking. The developed RF-power harvesting textiles also apply to smart homes, where the RF modules can be embedded in couches, curtains, carpets to harvest neighboring Wi-Fi signals to power lamps, desk clock, etc. Other wearable applications that require a closer proximity between the transmitter and receiver have also caught the attention of recent research projects. However, when the receiving system is implemented into clothing and worn by its bearer (patients, consumer users, ...) it is subject to misalignments provided by the intermittent movements of the bearers and can compromise the RF performance of the system. In the next chapter, we will present and discuss a novel , patent-pending antenna topology used to mitigate the issue of misalignments while keeping excellent RF performance.

4.7   Conclusion

In this chapter, a harvesting jacket is proposed for the first time. It embodies the clothing-integration of antennas and power harvesting circuits for wearable applications. An array of low-profile antennas (patches) is combined with single-diode rectifiers where each antenna has its own rectifier and the outputs of all the rectennas (antenna + rectifier) are combined for high and robust DC power collection. Using boosted Wi-Fi signals, we were able to achieve a DC power collection of 0.6 mW, which is enough to drive a low-power sensor. This jacket can be used to wirelessly power low-power biosensors for medical applications.

CHAPTER 5

NEAR-FIELD FABRIC-INTEGRATED POWER TRANSFER AND HARVESTING FOR WEARABLE APPLICATIONS

5.1   Introduction

The next goal of this dissertation is to investigate wireless power transfer to wearable devices, using near-field power transfer systems integrated on items of clothing. Towards this, first a new antenna design, so called anchor shaped antenna is presented, and is demonstrated to be resilient to physical misalignment [112].Secondly, we use the proposed design to realize an ergonomic power transfer system which can use the daily use-cases of activities for wireless power supply [113]

We present and discuss a new class of antennas suitable to mitigate the effects of angular and lateral misalignments in near-field power transfer and harvesting. This antenna topology exploits the combination of both electric and magnetic coupling modes within the regime of inductive wireless power transfer to achieve a high power transfer efficiency (PTE) and also presenting a resilience to the lateral and angular misalignments. In this dissertation, we report a fabric-integrated wearable charging platform that exploits daily life activities, such as sitting on a chair or laying in a bed, to operate wearable devices. This wearable charging feature is relevant in the context of prior studies on sedentary lifestyle, which reports a dominance of sedentary states in our daily activities [114]. This study reported that on average, test subjects spent approximately 57% of the time in activities like lying, reclining, and sitting, and 37% in light activities where they could be in close vicinity of the surfaces (back of a chair, mattress, sheets, etc) to receive wireless RF power. This prevalent lifestyle provides an opportunity for wireless charging of phones, IoT/IoHT devices (Fig. 5.1). In the next sections, the fundamentals are presented

and discussed (Section 5.2) and followed by the integrated of the antenna structure into clothing for wearable applications (Section 5.3).

5.2   Anchor-Shaped Antenna: Fundamentals

Electric and magnetic coupling modes discontinuous loops has been studied in microwave filters [54]. The fringe-enabling cavity or gap allows generation of fringing electric fields, leading to an electric-field type coupling between the two loops. This electric field is added to the magnetic field that is inherent to the metallic structure of the loop. As a result, the fringe-enabling cavity can enable a magneto-electric couplings, where double resonance and frequency bifurcation effects take place [55]. The proposed structure is referred to as an anchor-shaped structure that uses the mixture of electric and magnetic couplings for power transfer. Specifically, electric coupling modes are enabled, when anchor-shaped antennas are misaligned from their normal, perfectly aligned (broadside) position.
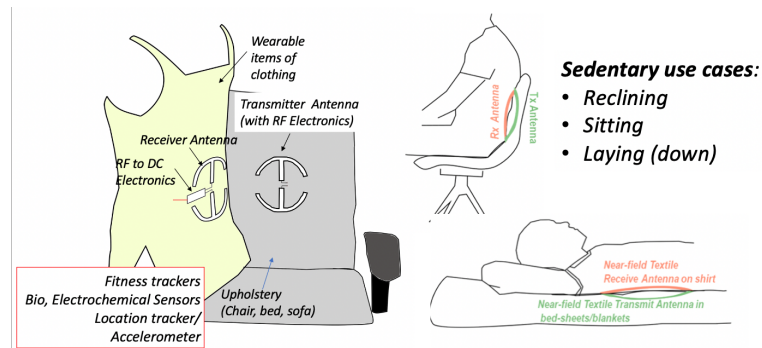
Figure 5.1: Integration of the proposed wireless power transfer and harvesting system consisted of textile-based anchor-shaped antenna (operating at 360 MHz) into clothing and upholstery: (left) implementation of the system into a dress and chair with potential sensing applications and (right) illustration of different sedentary use-cases.

RF to DC
Electronics

Transmitter
electronics

g

θ

ΔY

ΔX

(b)

(a)

(c)
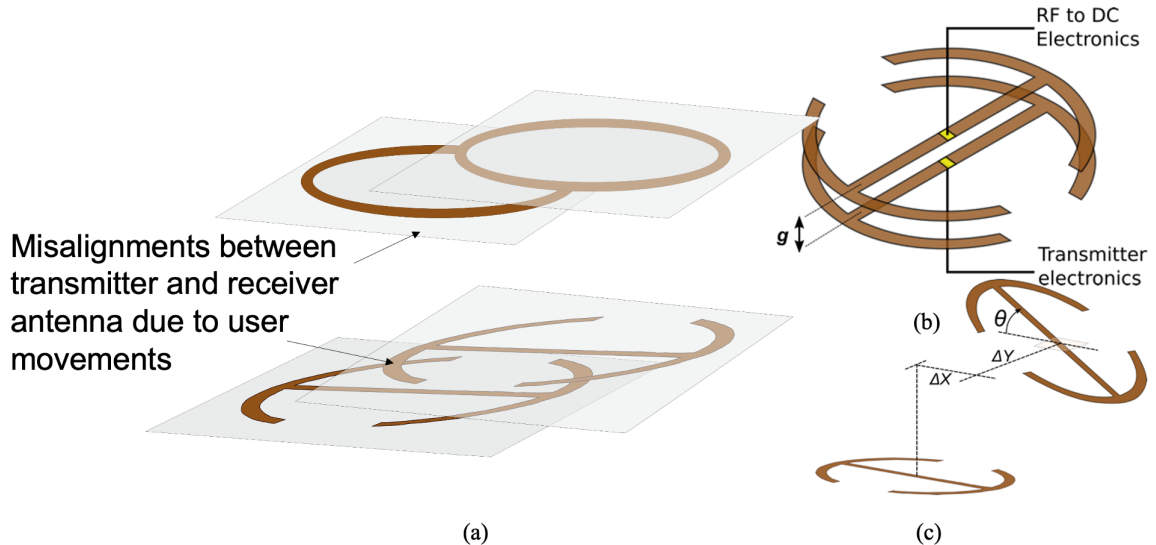
Figure 5.2: (a) Misalignment between the transmitter and the receiver antenna for near-zone power transfer (b) Geometry and configuration of the proposed misalignment resilient power transfer system (c) A typical misaligned case where angular misalignment of θ and lateral misalignment of x and y are shown.

5.2.1 The Proposed anchor-shaped Antenna

To demonstrate the new functionality of the structure, we compare its properties with the two basic types of resonators, i.e. a loop resonator (magnetic resonator) and a dipole resonator (electric resonator). We summarize the current distributions on the three resonators at their respective resonant frequencies as shown in Fig. 5.3. As can be seen on this figure, a dimension $L = 15$ cm was chosen to create similar footprints of the three resonators in order to realize a fair comparison. As shown in Fig. 5.3, the loop antenna shows one wavelength long current distribution along its total length and dipole shows a half wavelength long current distribution. Remarkably, the properties of these two resonators are put together to generate those of the anchor-shaped antenna. It can be observed that approximately half wavelength long current distribution is found along the geometry of the anchor-shaped antenna. More details will be discussed in the next paragraphs. The half wavelength resonance

(a)   λ   (b)   (c)

L

L~λ/2

~λ/2

L

w

G

Resonance
at 0.72 GHz

Resonance
at 0.90 GHz

Resonance
at 0.41 GHz
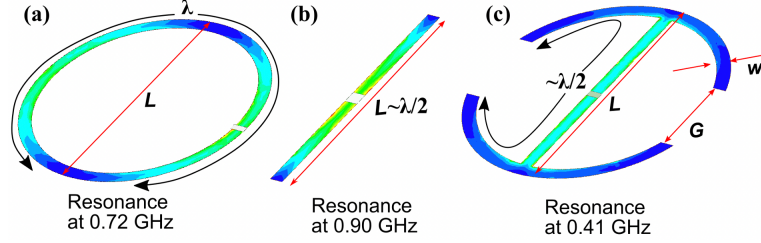
Figure 5.3: Qualitative comparison of the resonant frequency and corresponding current distributions (not to scale, light color represents maxima, and dark color represents minima) for the related resonant antenna configurations (a) single loop, (b) dipole, and (c) anchor-shaped. The length $L = 15$ cm is chosen in this example, the width of the antennas was w = 0.75 cm, G = 5 cm

.

leads to the miniaturization (decreased resonance frequency-longer wavelength) and an anchor- shaped allows increased coupled surface (aperture) and a strong fringing electric field in the vicinity of the resonator through the fringe-enabling cavities on either side of the structure. As a result, the proposed structure adds an electric coupling mode on top of magnetic coupling already present in loop antennas. These effects lead to improved couplings under misalignments, as further discussed in the next sections. This is a result of the miniaturization property of the anchor-shaped topology, where lower resonant frequency is attained for the same footprint. The
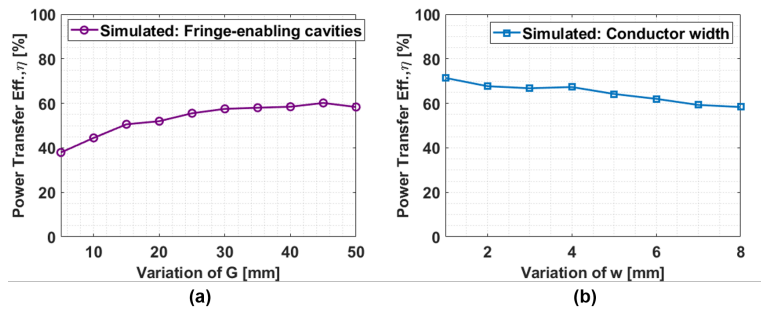
Figure 5.4: Power transfer efficiency of the anchor antenna as a function of the (a) fringe-enabling cavity and (b) width of the strip-line. In these simulations, G = 5 cm when w varies, w = 0.75 cm when G varies , and L = 15 cm.

miniaturization of the anchor-shaped antenna can be seen from the input impedance

and reflection coefficient properties. A comparison of these properties for anchor and loop is shown in Fig. 5.5(a) and (b). As known, the resonance is associated with $\chi(f) = 0$ and $\chi'(f) > 0$, where χ is the reactance profile and χ' is the first derivative of the reactance profile [115]. Considering this in Fig. 5.5(a), the resonant frequency changes from 0.8 GHz for the loop to about 0.4 GHz for the anchor. This verifies the miniaturization property of the antenna. This is further evident in Fig. 5.5(b), where the resonant frequency moves down along the frequency axis for the anchor antenna. In Fig. 5.5(c), the power transfer efficiency (PTE) calculated using
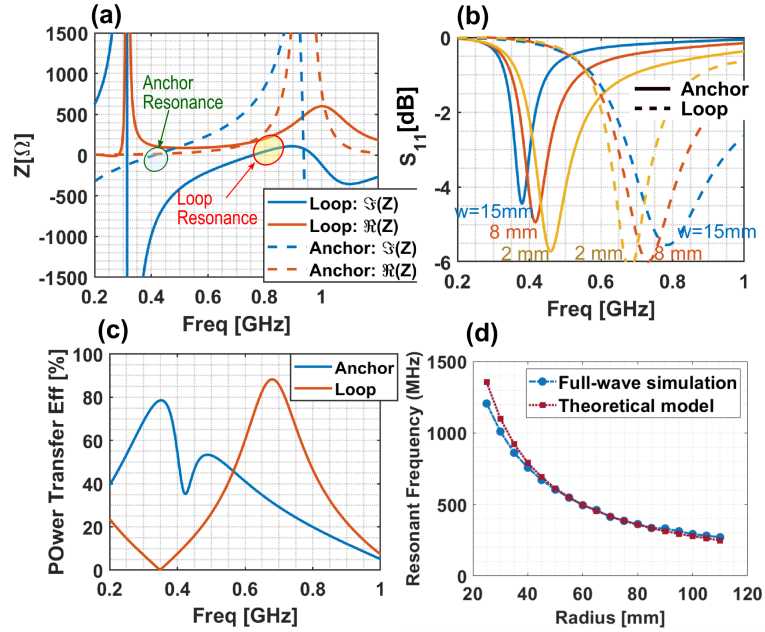
Figure 5.5: Comparison of the anchor shaped and loop antenna in terms of the their (a) input impedance (b) S_{11} matching with changing strip width (c) Power transfer efficiency (%) in presence of similar receiver antenna positioned at 1 cm distance (d) comparison of the theoretical and numerical model of the resonance frequency of the anchor-shaped antenna. In these simulations, we use the dimensions as G = 5 cm, w = 0.75 cm, and L = 15 cm.

$$\eta = \frac{|S_{21}|^2}{(1 - |S_{11}|^2)(1 - |S_{22}|^2)} \tag{5.1}$$

between the transmitting and receiving antennas is shown when the antennas of same type are considered for the transmitter and receiver (as shown in Fig. 5.2(b)).

We observe frequency bifurcation effect caused by two PTE peaks in the proposed antenna. This is typical for coupled structures that simultaneously have electric and magnetic coupling [54]. A gap g was chosen to be 1 cm for this comparison. The power coupling for the loop is slightly better in this aligned case. However, a more in-depth study considering different degrees of misalignments revealed that the PTE for the anchor-shaped antenna is better than that of its loop counterpart.
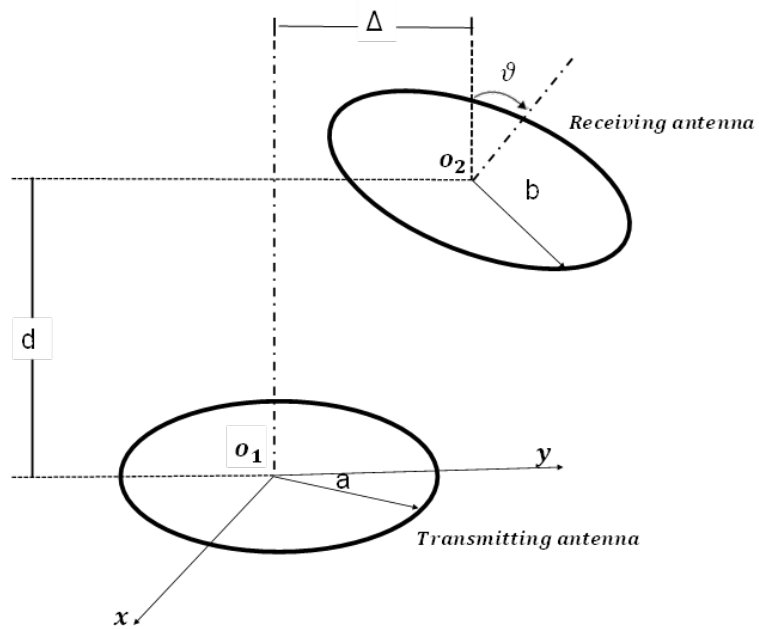
Figure 5.6: A wholesome view of the wireless power transfer system with all lateral and angular misalignments: "d" is the fixed distance between the transmitter and the receiver's initial position. It is represented by "g" in the previous sections. "Δ" is the lateral misalignment distance and "ϑ" is the angular misalignment angle. "a" and "b" are the Tx and Rx radii.

The above discussion points to the conclusion that the anchor antenna is a miniaturized form of the loop antenna combined with dipole to realize the enhancement of the PTE explained via two mechanisms such as (1) the extension of the wavelength and (2) the enhancement of the fringing fields. The RF properties of the anchor-shaped antenna are ultimately deduced from the loop antenna due to the fact that the loop is used as the genesis for the anchor. For more effective PTE, it is

reported that the magneto-inductive effects are used in conjunction with resonance to compensate for the leakage inductance[116]. In this work, the resonant frequency of the loop is the frequency at which the quality factor, Q [117] (which represents the ratio of the energy stored via inductive effects and the energy dissipated per oscillation) is the highest. Thus, the resonance frequency is written as

$$f_{loop} = \frac{c^{8/7}\mu_o^{1/7}\rho^{1/7}}{4 \times 15^{2/7}\pi^{11/7}r_c^{2/7}a^{6/7}},$$

(5.2)

where c is the speed of light, μ_o is the permeability of free space, ρ is the resistivity of the conductive material, r_c is the radius of the conductor, and a is the outer radius of the antenna, is empirically deduced [117]. For the anchor-shaped antenna, the only unknown is set to be the outer radius, a as all the other parameters such as the radius of the conductor and the dimensions of the fringe-enabling cavities (G = 2/3 a) are indeed a function of the outer radius. The resonant frequency of the anchor was thus empirically deduced to be

$$f_{theoretical-anchor} = \frac{10^{9/7}c^{8/7}\mu_o^{1/7}\rho^{1/7}}{4 \times 15^{2/7}\pi^{11/7}a^{8/7}}.$$

(5.3)

In equation (5.3), the cavities have a dimension of two thirds of the outer radius of the anchor and the width (w) of the conductive traces, one tenth of the outer radius. These values were chosen to assure the scalability of the anchor shaped antenna at high frequencies (i.e. at smaller footprints). The performance of the anchor-shaped antenna as a function of these parameters was simulated and reported in Fig. 5.4. The theoretical analysis from equation (5.3) was verified by a full-wave simulation from Ansys HFSS. The comparison between the two models is presented in Fig. 5.5(d). As can be observed, the full-wave simulation and theoretical values of the resonant frequency are in good agreement.

The corresponding inductance of the anchor-shaped antenna was inspired from [117] and can be written as

$$L_{anchor} = \frac{7\mu_o a}{2\pi} \times \left[ln\left(\frac{28a}{\sqrt{\pi w s}}\right) - 2 \right],$$ (5.4)

where w and s are the dimensions of the conductive traces. This self-inductance value is found to be 363 nH, which is higher than 319 nH found for the single loop as reported in [117]. The latter was expected as the length of the conductor in anchor ($P \approx 7a$) is more than that of the loop ($P = 2\pi a$). This is one of the indicators of the reduction of the resonant frequency given by $f_r = 1/(2\pi\sqrt{LC})$. Another factor contributing in the reduction of the frequency is the fringing fields that enhances the capacitance of the anchor, again decreasing the resonant frequency.

From the resonant frequency and the inductance, we deduce the self-capacitance, which is:

$$C_{anchor} = \frac{50 \times a}{7\pi\mu_o c^2} \left[ln\left(\frac{28a}{\sqrt{\pi w s}}\right) - 2 \right]^{-1}$$ (5.5)

where $C_{anchor} = C_{self} + C_{fringe}$. The capacitance associated to the fringing fields can be taken from [118] and can be written as:

$$C_{fringe} = \epsilon_0 \left(\left(\frac{\epsilon_r w}{h}\right)^n + ((\epsilon_r + 1)\pi)^n \left(\frac{1}{ln(\frac{8h}{w+1})} - \frac{w}{8h}\right)^n \right)^{\frac{1}{n}}$$ (5.6)

In this case, n=1.08, w is the with of the strip line, h is the distance separating the two conductive surfaces to generate the fringing fields, and ϵ_r, the dielectric of the transmitting medium. This theoretical model was demonstrated and tested in [118] for dielectric constants from 1 to 24 and for values of h extending from 0 to ∞. For anchor shaped antennas, h can be the fringe-enabling cavity, G or the fixed distance separating the antennas, g. It should be noted that, in this model, the parallel plates are assumed to be perfectly aligned with each other. In the case of misalignments, the new value of the separation becomes $h = \sqrt{d^2 + \Delta^2}$ (for lateral

misalignments) and $h = \sqrt{2a^2(1 - cos\vartheta)}$ (for angular misalignments). Each anchor antenna has a surface area of:

$$A_{anchor} = \pi[a^2 - (a-w)^2] - 2Gw + 2(a-w)w = \frac{57\pi a^2 + 14a^2}{300} \qquad (5.7)$$

The expression of the equation (5.7) is written based on the value of $G = \frac{2a}{3}$ and w $= \frac{a}{10}$ and the mutual capacitance deduced from it will be:

$$C_{mutual} = \epsilon_o \frac{A_{anchor}}{h} = \epsilon_o \left(\frac{57\pi a^2 + 14a^2}{300h} \right) \qquad (5.8)$$

Again, the value of h can be g, G, $\sqrt{d^2 + \Delta^2}$, and $\sqrt{2a^2(1 - cos\vartheta)}$ where Δ is the varying distance in lateral misalignments. In overall, the capacitance of the whole system can be written as:

$$C_{total} = C_{self} + C_{fringe} + C_{mutual}. \qquad (5.9)$$

The total capacitance will be then:

$$C_{total} = C_{Anchor} + C_{mutual} = \frac{50 \times a}{7\pi\mu_o c^2} \left[ln\left(\frac{28a}{\sqrt{\pi ws}} \right) - 2 \right]^{-1} + \epsilon_o \left(\frac{57\pi a^2 + 14a^2}{300h} \right) \qquad (5.10)$$

The inequality (5.11) suggests that the electric coupling has a higher influence in enhancing the wavelength through the extent of the fringing fields. The introduction of the fringe-enabling cavities improve the PTE when transiting from single loop to anchor. This is a result of the increase of the spanning area for coupling between the transmitter and receiver. Therefore, can shift the frequency based on the inequality below

$$\frac{1}{2\pi\sqrt{L(C + C_m)}} < f_{broadside} < \frac{1}{2\pi\sqrt{(L - L_m)C}} \qquad (5.11)$$

where C_m and L_m are the system's mutual capacitance and inductance, respectively. The latter are subject to change based on the misalignment due to the fact that each misalignment strengthens a particular set of fringing fields as explained in [65].

When taking the dipole-like performance of the anchor-shaped antenna into account, a more simplistic model can be derived. From [119] we deduced that, for the anchor antenna, $Perimeter_{anchor} = 2\pi a + 2a - 2G = 2\pi a + 2a - 2(\frac{2}{3}a) \approx 7R = 0.7\lambda$. We then deduce the following expression for the frequency:

$$f_{simplistic-anchor} = \frac{c}{10 \times a} \tag{5.12}$$

where c is the speed of light and a, the outer radius of the anchor antenna. As can be seen in Fig. 5.7, the simplistic model agrees with the simulated results perfectly. For anchor antennas of radius 3 cm or longer, the simplistic model from equation 5.12 differs from simulation by only 5% while the model from equation 5.3 varies from the simulation model by up to 9%. The percent error was calculated using the equation:

$$\delta = \left| \frac{Theoretical/Simplistic - Simulated}{Simulated} \right| \times 100\% \tag{5.13}$$

This result suggests that the anchor-shaped antenna has a dipole-like functionality. Indeed, the equations only take into account. The mutual inductance, using the work published in [120], can be expressed as:

$$L_{m(anchor)} = \frac{\mu_o \pi a^2 b^2}{2(a^2 + b^2 + z^2)^{3/2}} \left(1 + \frac{15}{32}\gamma^2 + \frac{315}{1024}\gamma^4 \right) \tag{5.14}$$

where a and b are the radii of the transmitting and receiving antennas, z the distance between the axes of the transmitter (Tx) and receiver (Rx), and $\gamma = \frac{2ab}{a^2+b^2+z^2}$. In this work, $a = b$, the equation 5.14 will be:

$$L_{m(anchor)} = \frac{\mu_o \pi a^4}{2(2a^2 + z^2)^{3/2}} \left(1 + \frac{15}{32}\gamma^2 + \frac{315}{1024}\gamma^4 \right) \tag{5.15}$$

and $\gamma = \frac{2a^2}{2a^2+z^2}$. When the system undergoes misalignments, we will have the following:

1. **Lateral misalignments:** the length z becomes z' and the equation 5.15 can be expressed as:

$$L'_{m(anchor)} = \frac{\mu_o \pi a^4}{2(2a^2 + z'^2)^{3/2}} \left(1 + \frac{15}{32}\gamma'^2 + \frac{315}{1024}\gamma'^4 \right) \quad (5.16)$$

$z' = \sqrt{D^2 + g^2}$ is the misaligned distance between the centers of the Rx and Tx, where g the fixed distance from the receiving antenna initial center found in the previous equation 5.7 , and $\gamma' = \frac{2a^2}{2a^2 + z'^2}$.

2. **Angular misalignments:** the length z becomes z' and the equation 5.15 can be expressed as:

$$L'_{m(anchor)} = \frac{\mu_o \pi a^4}{2(2a^2 + z'^2)^{3/2}} \left(1 + \frac{15}{32}\gamma'^2 + \frac{315}{1024}\gamma'^4 \right) \quad (5.17)$$

$z' = \sqrt{2a^2(1 - cos\theta)}$ is the misaligned distance between the centers of the Rx and Tx, where a is the outer radius of the receiver/transmitter found in the previous equation 5.7 , and $\gamma' = \frac{2a^2}{2a^2 + z'^2}$.

This is a reinforcement of the results found in Fig. 5.3 from Section 5.2.1.

inin
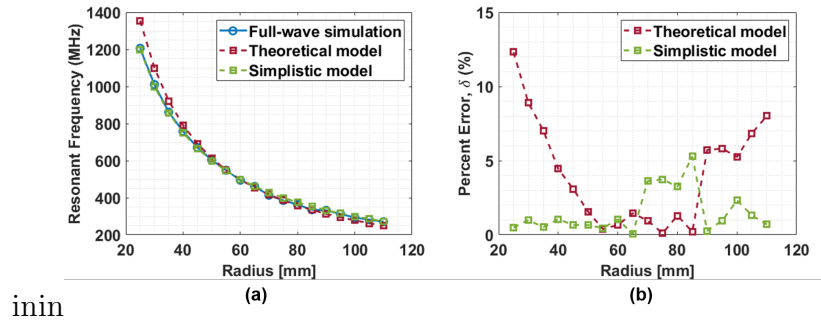
Figure 5.7: Representation of the theoretical and simplistic model of the anchor-shaped frequency modulations compared to their simulated counterpart : (a) theoretical and simplistic models compared to simulation and (b) percent error of the aforementioned models with respect to their simulation counterpart.

68

5.2.2 Near-Field Characteristics

We next focus on the near-field characteristics of the antenna, which have a bearing on the PTE. In Fig. 5.8, we show the vector profile of electric and magnetic near-fields of the loop antenna in its principal plane. These fields are then compared with similar field profiles for the anchor shaped antenna shown in Fig. 5.9. For the loop antenna, E-field lines exist across the diametrically opposite points of the loop. These points are associated with the current minimum in the loop. Likewise, the
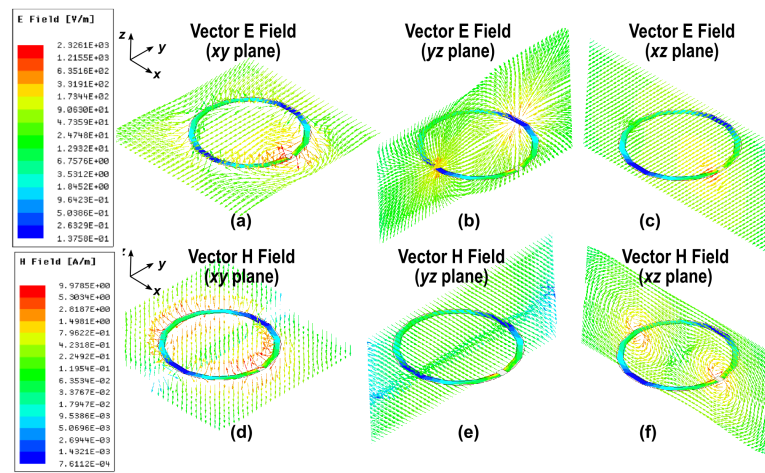
Figure 5.8: Vector E and H fields at the resonant frequency of the resonant loop antenna in orthogonal planes through the geometry of the antenna. (a) – (c) Vector E field in xy, yz and xz planes, (d)-(f) Vector H-fields in xy, yz and xz planes. Same dimensions as in Fig. 5.5 were used.

nature of H-field lines can be derived from the vector plots in Fig. 5.8(d), (e) and (f), suggesting that these fields exist around the conductor near the current maximum points. The input power was chosen to be the default value of 1 W provided by HFSS. A summary of field-lines are summarized in the sketch drawn in Fig. 5.10(a). The vector field profile of the anchor-shaped structure is shown in Fig. 5.9. From Fig. 5.9(a)-(c), it can be inferred that the E-field vector is aligned along the central strip (shank) of the anchor. Furthermore, electric fields also extend beyond the
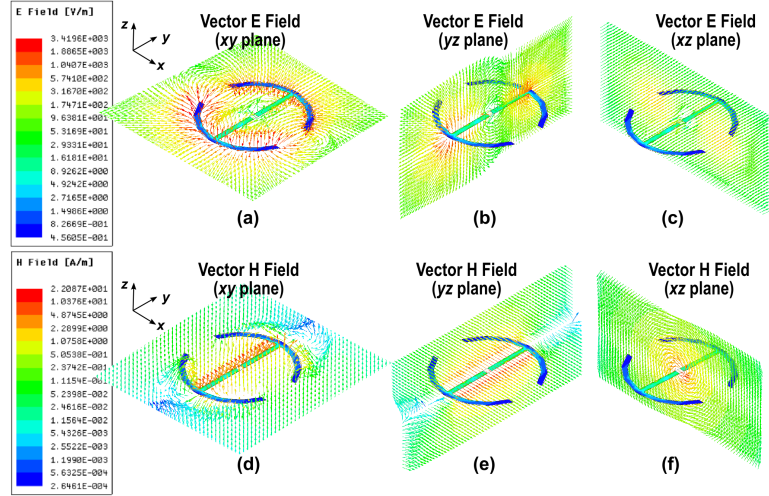
Figure 5.9: Vector E and H fields at the resonant frequency of the anchor shaped antenna in three orthogonal planes through the geometry of the antenna. (a) – (c) Vector E field in xy, yz and xz planes, (d)-(f) Vector H-fields in xy, yz and xz planes.

coupled surface (aperture) due to the fringing fields associated to the two open ends of the anchor (see Fig. 5.10(b)). It is noted that the extended E-fields are also due to the large wavelength, as compared to loop, where the total loop radius is $\lambda/2\pi$ as compared to anchor, where the structure is similar to a miniaturized $0.7 - \lambda$ dipole. These extended fields allow coverage between the transmitter and receiver even under misalignment cases.
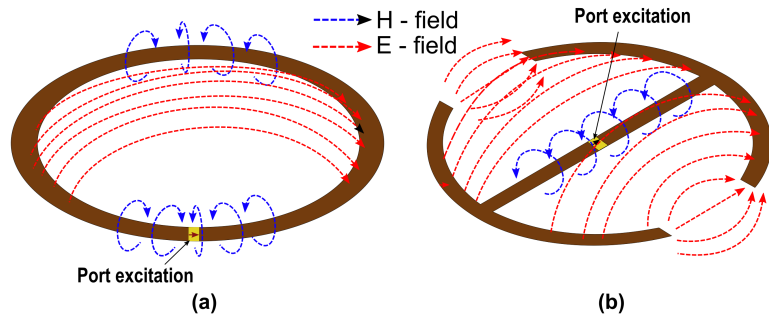
Figure 5.10: Summary of electric and magnetic field lines in the (a) PEC loop and (b) PEC anchor shaped resonators.In these simulations, G = 5 cm, w = 0.75 cm, and L = 15 cm.

5.2.3 Power Transfer Characteristics under Misalignment b/w Transmitter and Receiver

To validate the effect of fringing field and increased wavelength, the power transfer efficiency under different misalignment scenarios are shown in Fig. 5.12 and 5.13. Specifically, we consider four degrees of freedom, where the receiver and transmitter antennas are misaligned. These include the two lateral misalignment movements (represented by Δx, Δy) and the two angular misalignment movements (represented by ϕ, θ).These improvements are associated to (a) longer wavelength (at resonance frequency) allowing a greater extent of electric field lines and (b) presence of fringing fields owing to the open ends of the anchor. The chosen geometrical dimensions of
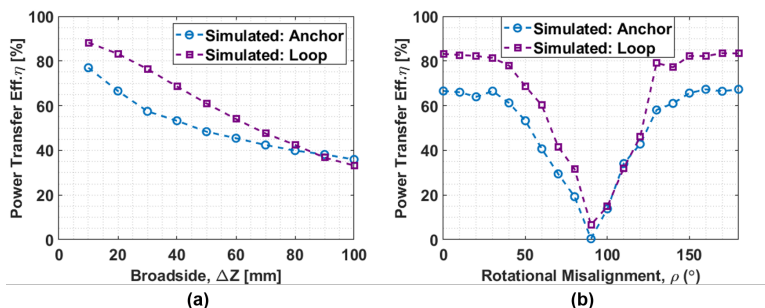
Figure 5.11: Power transfer efficiency of the anchor antenna compared to loop, when (a) the antennas are separated away from one another along the orthogonal axis and (b) rotating the receiving antenna around the orthogonal axis while keep the distance constant with respect to one another. We chose G = 5 cm, w = 0.75 cm, and L = 15 cm for these simulations.

the antennas are same as shown previously in Fig. 5.3. The misalignment resilience of the PTE for the lateral misalignment cases are shown in Fig. 5.13(a). It is noted that for the aligned case (Δx=0 or Δy=0), the efficiency is smaller for the anchor antenna than the loop antenna. We continued the evaluation of the PTE in the broadside direction and found that the single loop antenna performed slightly better than its anchor counterpart (see Fig. 5.11). The frequency of operation was

found to be between 340 MHz and 380 MHz for anchor and 678 MHz and 680 MHz for loop. But the PTE performance becomes better for the anchor shaped antenna for the cases when $\Delta x > 5$ cm or $\Delta y > 5$ cm lateral misalignment. This represents misalignment of 33% of the aperture size.

The resonance frequency for the loop antenna is around 0.72 GHz and for anchor shaped antenna is 0.41 GHz. Since we postulate that the improvement in PTE is due to both, the frequency reduction and the fringing fields, we would like to isolate the role of fringing fields for the improvement in the PTE. Therefore, we plot the PTE as a function of electrical distances (normalized by the wavelength of operation) as shown in Fig. 5.13(b). We do see improvement in the PTE for 0.4λ and $\Delta y > 0.6\lambda$ in this case, which suggests that the fringing fields are indeed responsible for an improvement in PTE under misalignment cases. Furthermore, fringing fields also effect the azimuthal and elevation misalignments as shown Fig. 5.13(c) and (d). Once again, the proposed anchor shaped structure shows improved PTE for $\theta > 30°$ and $\phi > 30°$, owing to the decreased resonant frequency and the extent of the fringing fields. The PTE was also evaluated while changing the orientation of the transmitter relative to the receiver (Fig. 5.11(b)). We notice that when the shanks of the receiver and transmitter are orthogonal the power transfer efficiency shows a null. These results will be further supplemented by measurements in Section 5.2.5.

5.2.4   Magnetic versus Electric Coupling in the Lateral Misalignment

For the proposed antenna, the modality of power transfer changes from inductive to capacitive under different lateral misalignment scenarios. An artifact of this is also the slightly reduced PTE for the proposed antenna when compared to the
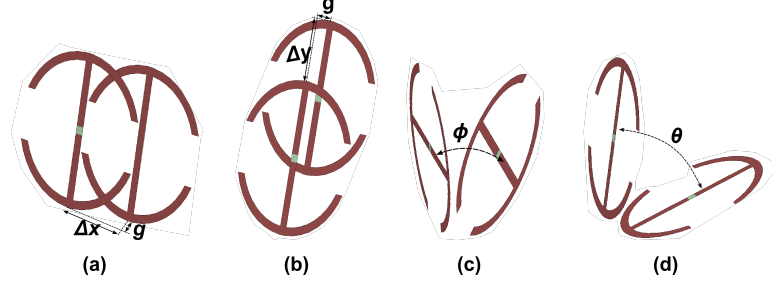
Figure 5.12: Degrees of freedom used for assessment of the proposed antenna (a) Lateral misalignment along openings (b) Lateral misalignment along shank (c) Azimuthal rotational misalignment around shank (d) Elevational rotational misalignment along crown

loop antenna under small lateral misalignment cases (Fig. 5.13(a)). To understand these features, we propose a new method for analysing the type of coupling from transmitter to receiver. Specifically, it is well-known that the EM fields in electric (capacitive) coupling are associated to a wave-impedance greater than 377 Ω and the EM fields in magnetic (inductive) coupling are associated to wave impedance smaller than 377 Ω [121]. Therefore, the inequality

$$Z(inductive) < 377\Omega < Z(capacitive) \tag{5.18}$$

lays out the conditions for these cases. We note that for a strong inductive coupling Z should be much smaller than 377 Ω, and by the same token for strong capacitive coupling Z should be much greater than 377 Ω. When Z is close to 377 Ω, the impedance of the coupled structure is matched with the free-space impedance which is the radiation condition. This refers to radiation loss condition and is associated to loss of efficiency. As stated in [54], in the vicinity of the cavities, the electric field is stronger. By the same token, away from the cavities (in the vicinity of the central bar, which is the shank of the anchor), the magnetic field is stronger. To test these scenarios, a specific apparatus is considered for each:

73

1. The transmitter and receiver are kept at a fixed distance of 20 mm and the receiver is moved laterally along the shank of the transmitter (Fig. 5.14(c), along shank). In this experiment, we anticipate magnetic coupling.

2. The transmitter and receiver are kept at a fixed distance of 20 mm and the receiver is moved laterally across the cavity of the transmitter (Fig. 5.14(c), along cavity). In this experiment, we anticipate electric coupling.

The extent of couplings (magnetic or electric) can be compared using the maximum E-field or H-field values in the respective cases.
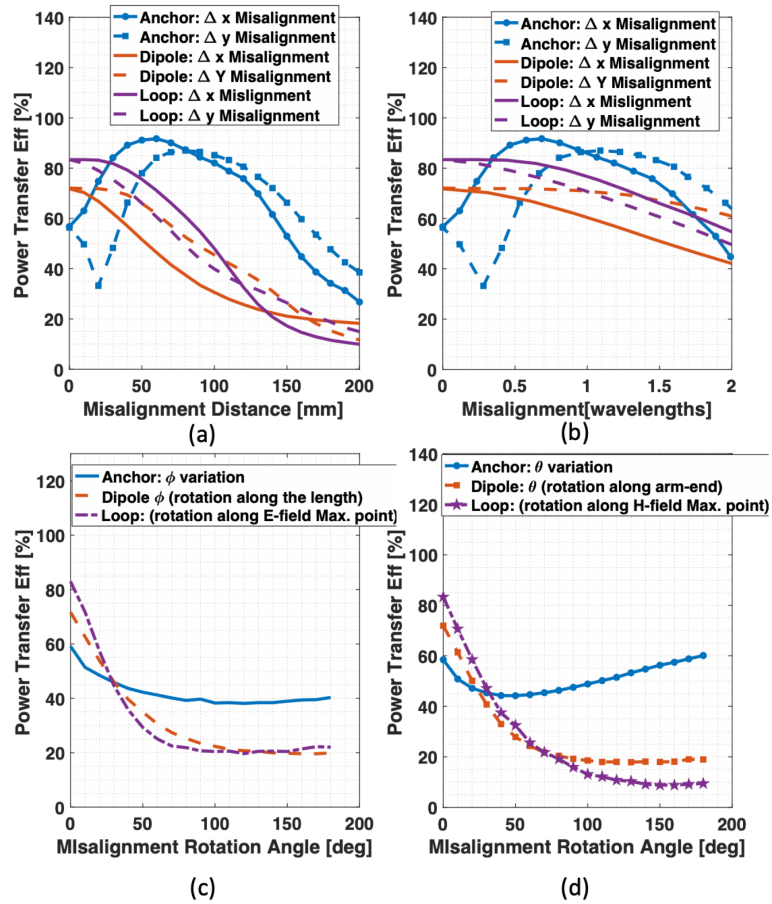
Figure 5.13: Power transfer efficiency under different degrees of misalignment, for the anchor shaped structure, compared with the traditional resonant loop antenna. g was 2 cm, G = 5 cm, w = 0.75 cm, and L = 15 cm for these simulations.

A full-wave simulation was carried out for the above cases. The conductive traces of the antennas were assigned PEC boundary conditions, an airbox was used to model free space radiation, and a 50-Ω lumped port was assigned to each antenna's excitation port. Medium-sized mesh grids were used for the setup. While displacing the receiving antenna by up to 10 cm, the peak electric and magnetic fields were recorded for each case. The recorded values are plotted in Fig. 5.14(a) and (b). A qualitative parameter to determine the type of coupling, i.e. the ratio of the peak electric and magnetic fields, is plotted in Fig. 5.14(d). The comparison impedance through inequality (5.18), knowing the free-space wave impedance ($Z_o = 377$ Ω) is also shown. Fig. 5.14(d) shows a monotonic increase in the wave-impedance as the
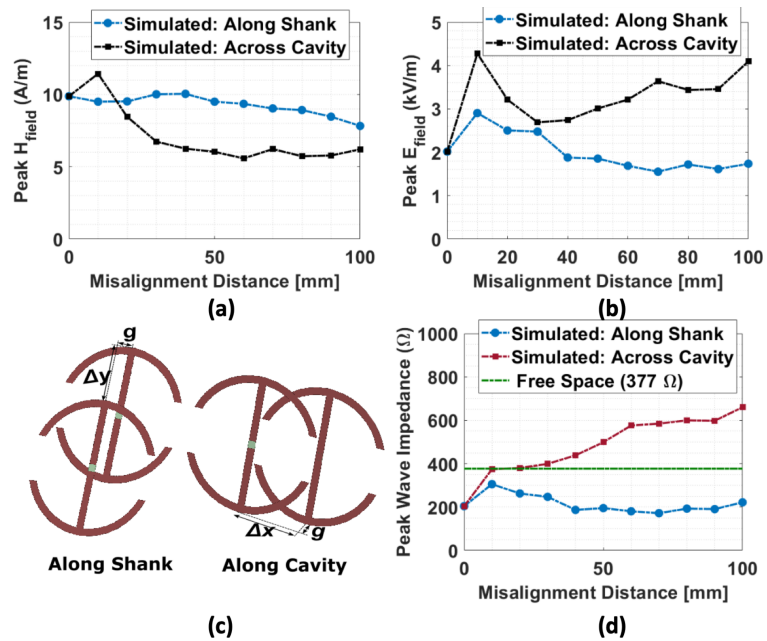
Figure 5.14: Near field and wave-impedance characteristics of the proposed anchor antenna (G = 5 cm, w = 0.75 cm, and L = 15 cm) (a) the peak magnetic field exhibited by the transmitter as the receiver slides along the shank and across the crowns of the transmitter (b) the peak magnetic field exhibited by the transmitter as the receiver slides along the shank and across the crowns of the transmitter (c) misalignment setup for E-field and H-field testing (d) peak wave impedance of the air gap between the transmitter and receiver obtained from the corresponding electric and magnetic fields compared to impedance of plane waves in free space.

antenna is moved along the shank, while shows an increase and then decrease for the case along the cavity. That is, for the either of the cases, the system looses energy in radiation for small misalignment distances due to Z close to 377 Ω. Furthermore, the peak in 'Along-shank' curve is associated to the dip in the PTE for the ΔY misalignment in Fig. 5.13(a), since the peak represents an impedance closer to 377 Ω.

This analysis further serves to verify that the use of fringing-fields invokes capacitive coupling, aiding PTE for the misalignment cases. Through this, the system exploits mixed couplings by virtue of its unique shape. The proposed principle also holds for different types of the polygons used in lieu of the circular periphery. As can be seen in Fig. 5.15, regardless of the nature of the polygon forming the crown of the anchor, the performance the power transfer efficiency is retained as the same.

5.2.5 Measurements

The validation of the proposed anchor-shaped antenna is realized by measuring the PTE of the antenna and comparing it with the PTE of the loop antenna. Both loop and anchor antennas were prototyped using FR4 substrate of dielectric constant $\epsilon_r = 4.4$, loss tangent $tan\delta = 0.017$ and thickness 1.54 mm. The photos of the measurement set-up and measured results are shown in Fig. 5.16 and Fig. 5.17, respectively.

First, a comparison of the PTE performance of the loop antenna and the anchor antenna is conducted when the antennas had the same footprint of $L=$ 15 cm. The other dimensions of the fabricated anchor antenna were $G = 5$ cm and $w = 0.75$ cm. These results are shown in Fig. 5.17 (a)-(c). For these cases, the resonant frequency of the anchor-shaped antenna was found to be approximately half of the
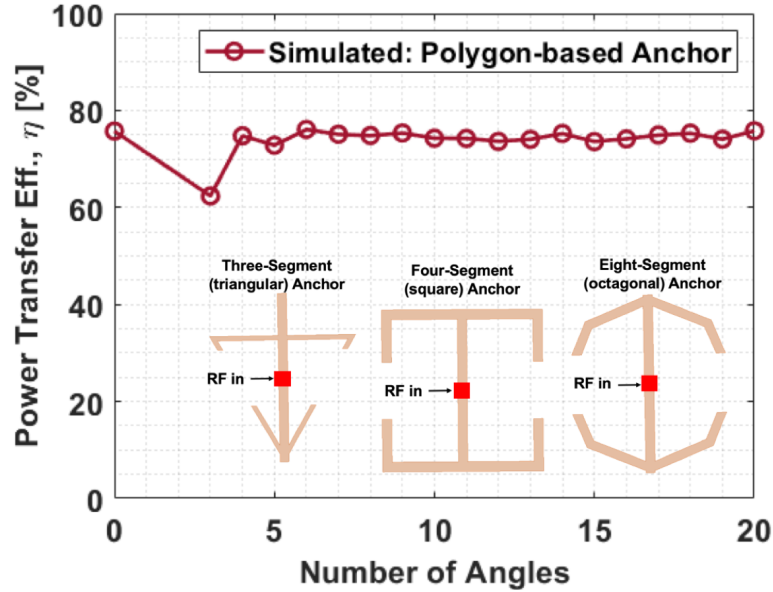
Figure 5.15: Photo of the PTE performance of different polygonal configurations (various segments or angles) used to generate the crowns of the anchor(in inset): example of three different anchors generated from different polygonal peripheries.

loop antenna. To isolate the effect of only the shape, in the second case, we compare the performances of anchor and loop designed for the same operating frequency. For this case, anchor antenna with footprint $L=9$ cm is characterized and compared with the loop antenna (Fig. 5.17 (d)-(h)). Within this case, the radii of the loop and anchor are different, therefore, two choices exist for axis of rotation. These choices are associated to two different results as shown in the inset of Fig. 5.17. Corresponding measurement cases are considered for a fair and rigorous comparison.

5.2.6 PTE Improvements for Lateral Misalignment

For lateral misalignment along the x-axis as shown in Fig. 5.17(a), the anchor antenna maintains a PTE almost constant at around 85% for varying misalignment cases. This was achieved when the receiver and transmitter are positioned with initial gap $g = 1$ cm and the receiver is moved sideways Δx from 1 cm to 10 cm. The

loop antenna, however experiences a decaying PTE from 90% to 40%. Further, Fig. 5.17(a) shows a good agreement between simulated and measured power transfer efficiency.

In Fig. 5.17(d), the results are compared for the 'small-anchor' and loop antenna. Once again, even with 60% miniaturized size, we observe better PTE performance of the anchor antenna over the considered range of misalignment. In Fig. 5.17(a) and (e), a trough is observed in the power transfer efficiency for small misalignment cases, which are consistent with the analysis presented in Section 5.2.4.

5.2.7   Angular Misalignment in the Elevation Plane

In this case, the rotational misalignment is introduced such that the central bars of the receiver and the transmitter create an angle θ, which is varied from 10° to 180°. As shown in Fig. 5.17(b), when considering the anchor of the same size as the loop antenna, an average PTE of 65% is shown by the anchor antenna and the PTE is almost uniform throughout the whole angular range. For the loop antenna, however, the PTE decreased from 85% to 20% for this angular range. Similar comparisons are made between the 'small-anchor' ($G = 3$ cm, $w = 0.2$ cm, and $L = 9$ cm) and the loop ($G = 5$ cm, $w = 0.75$ cm, and $L = 15$ cm) as shown in Fig. 5.17(e). The anchor antenna exhibited an average PTE of 80%, while the loop experienced a rapid decay. Another case that we considered was when the 'small anchor' was placed at the center of square substrate whose side is of same dimension as the loop antenna (15 cm). This is to create angular misalignment with the same radius of rotation as the larger loop antenna with dimension of L=15 cm (Fig. 5.17(g)). Due to miniaturized size and extended radius of rotation, the performance of the

anchor antenna was found to be degraded. Even so, the proposed antenna holds the advantage of miniaturization of 60%.

5.2.8   Angular Misalignment in Azimuthal Plane

The relative angular misalignment along the open ends of the anchor shape is referred to as azimuthal rotation (Fig. 5.16, right). For the same size case (Fig. 5.17 (c)), for $\phi \geq 50°$, the average PTE exhibited by the anchor antenna was found to be 55% while that of the loop antenna was 20%. For the same frequency operation or the 'small-anchor' case (Fig. 5.17 (f)), the average PTE was found to be 60%. For 'small-anchor' case with large rotation radius (Fig. 5.17 (h)), no improvement in PTE over the larger loop was noted due to the elongated radius of rotation. As shown before, the proposed geometry holds advantage of miniaturization for this case. In sum, the anchor-shaped antenna performs better than the loop antenna either due to increased power-transfer efficiency or due to miniaturized size. For all four misalignment degrees of freedom, the value of S_{11} was found to be between -6 dB and -44 dB for the anchor antenna and -8 dB to -37 dB for the loop antenna. 3-dB fractional bandwidth ranged from 26% to 72% for the anchor and between 16% and 29% for the loop.

5.2.9   Potential Applications

Due to the ability of the proposed power transfer system to sustain higher RF performance when subjected to misalignments, it can be incorporated into wearable and other IoT type devices. It is an excellent solution to smart and adaptive wireless charging, where some level of movement is anticipated by the bearer. Because of the low-profile and ease for fabrication, anchor-shaped antennas present themselves as

a strong candidate for charging platforms for on-clothing implementation of power transfer and harvesting and inductive charging for mobile phones and medical devices like insulin pump. In the next section (Section 5.3) we present a full textile version of the anchor-shaped antenna system for power transfer and harvesting for wearable applications (see Fig. 5.1). This system will comprise of a chair whose upholstery is used to implement the transmitter and a dress where the receiver (anchor-shaped antenna + rectifier). The design, fabrication, and measurements related to the whole system are presented in the section below.

5.3 Textile-Integration of Anchor-Shaped and Its Ergonomic Applications

5.3.1 Misalignment Resilient Antenna Geometries for Ergonomic Textile Integration

In the previous sections, an anchor shaped antenna geometry has been proposed which has shown high WPT efficiency under misalignments [65]. Specifically, this geometry showed approximately 65% improvement in efficiency, when compared to a loop antenna of same size and under linear and angular misalignment cases. Notably, these advantages arise from the two pronged advantage of the anchor shape (see Fig. 5.19). First, due to an open arm structure, the fringing electrical fields are exhibited near the open ends of the arms, and these fields extend beyond the area of the aperture. This allowed for wireless power transfer when the receiver and transmitters were misaligned. Secondly, due to a decreased frequency of operation, the anchor shaped structure was miniaturized as well. This allowed for extended

near-zone fields due to an increased wavelength and therefore an increase in the power transfer efficiency under misalignments. The same measurements were carried out for antennas of the same geometry and dimensions that were made of conductive textiles embroidered onto denim fabric. The antennas performed as good as their PCB-based ancestors and the results are reported in Fig. 5.18.
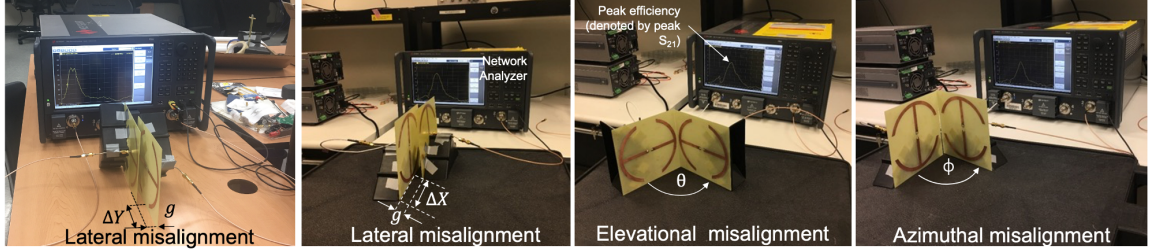
Figure 5.16: Photo of the 2-port measurement setup for power transfer efficiency evaluation (a) lateral misalignment (ΔY) with g=5 cm, (b) lateral misalignment (ΔX) with g=5 cm, (c) angular misalignment due to elevation, and (d) angular misalignment due to azimuth.

In this piece of work, we will demonstrate the wireless charging system that uses the previously proposed antennas. To test their performances for the wearable applications, we conduct tests of misalignment resiliency for the antenna, when wrapped around a cylindrical surface. We further conduct simulations to understand the surface absorption rates (SAR) of the skin tissue when using these antennas.

5.3.2 The Effects of Mechanical Deformation and Misalignment on PTE

Fig. 5.20 shows the efficiency of wireless power transfer when anchor shaped antennas are used for transmitter and receiver. Specifically, the tests consisted of a receiver antenna, which was wrapped around a cylindrical surface to mimic the wrapping of a flexible antenna over an arm or a leg ($R_{curvature} = 37$ mm). We also

considered the misalignment between the transmitter and receiver antennas to determine the effect of minor movements on the PTE. For this study, we chose anchor shaped antenna with diameter 15 cm and strip width of 0.75 cm. The results are supported by the distribution of electric and magnetic fields that can be seen in Fig. 5.21. The coupled antennas exhibited a resonant frequency of 360 MHz. This frequency was chosen considering certain defense and commercial bands such as 300 MHz and 433 MHz being commonly used. The size of the antenna can be scaled to align it exactly with these bands. More details on the RF properties of the antenna are shown in [65]. The efficiency (η) was obtained using scattering parameters evaluated from full-wave simulations and then by applying $\eta = \frac{|S_{21}|^2}{(1-|S_{11}|^2)(1-|S_{22}|^2)}$. The simulation results were further verified by measurement tests using fabric substrate antennas fabricated using embroidery of conductive threads on Denim + stabilizer textile (see Fig. 5.24(c)). The fabrication methods were adopted from the prior work of [122]. We also note a dielectric constant of $\epsilon_r = 1.67$ and a loss tangent $\tan\delta = 0.07$ for the textile surface from this prior work. The conductive thread, Elektrisola-7, was used for embroidery to prototype the anchor-shaped antennas. SMA connectors with 50-Ω impedance were soldered at the feeding ports for measurements.

Simulation and measurement results show power transfer efficiency (PTE) of the wrapped receiver antenna under misalignment (see Fig. 5.20). The radius of curvature of the cylinder was chosen to be 37 mm, which represents the radius of an average wrist. The normal distance between the transmitter and receiver antennas was chosen to be 1 cm, which represents a typical close distance power transfer while sitting or lying down (see Fig. 5.1). Depending on the direction of misalignment and two possible wrapping configurations (see Fig. 5.20(a) and (b)), four potential cases arise for this investigations. First, we consider case of misalignment along the
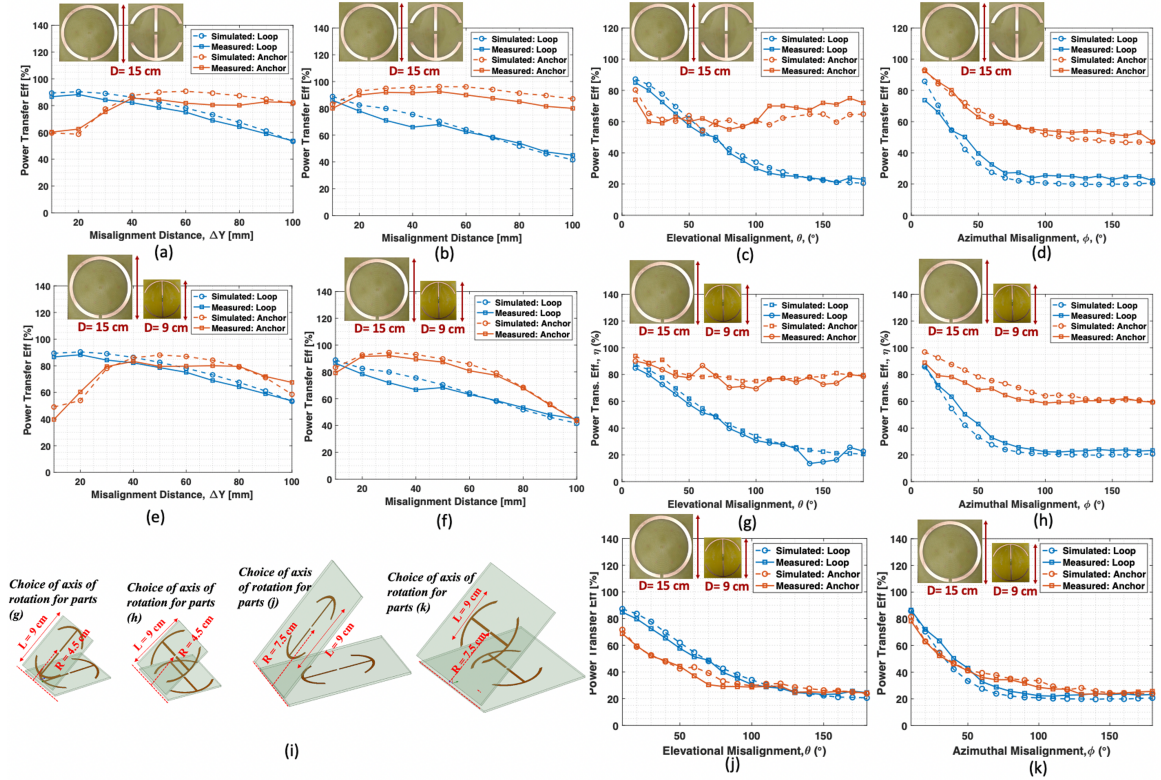
Figure 5.17: Misalignment tests for the large anchor as compared to the loop antenna for same sizes of the two types of antennas shown in (a)-(d) and same operational frequency for the two types of the two antennas (e)-(h). (i) shows the distinction in the measurement configuration for angular misalignment cases (g), (h), (j) and (k). The dimensions of the fabricated anchor shaped antenna was $G = 5$ cm, $w = 0.75$ cm, and $L = 15$ cm. For the smaller anchor antenna shown in the parts (j) and (k), the dimensions were chosen to be $G = 3$ cm, $w = 0.2$ cm, and $L = 9$ cm. The dimensions for the loop antenna were $w = 0.75$ cm, and $L = 15$ cm.

cavities. For this case, when the receiver antenna is wrapped across the cavities, the PTE was found to be 70% on an average upon misalignment (Fig. 5.20(c)), while an average PTE of 50% was found when the receiver was wrapped along the shank (Fig. 5.20(d)). The second case involves the misalignment movement along the shank where an average of 80% of PTE was exhibited when the receiver antenna was wrapped across the cavities (Fig. 5.20(e)) and 55% when it is wrapped along the shank (Fig. 5.20(f)). A maximum of 10 cm misalignment is shown, which rep-
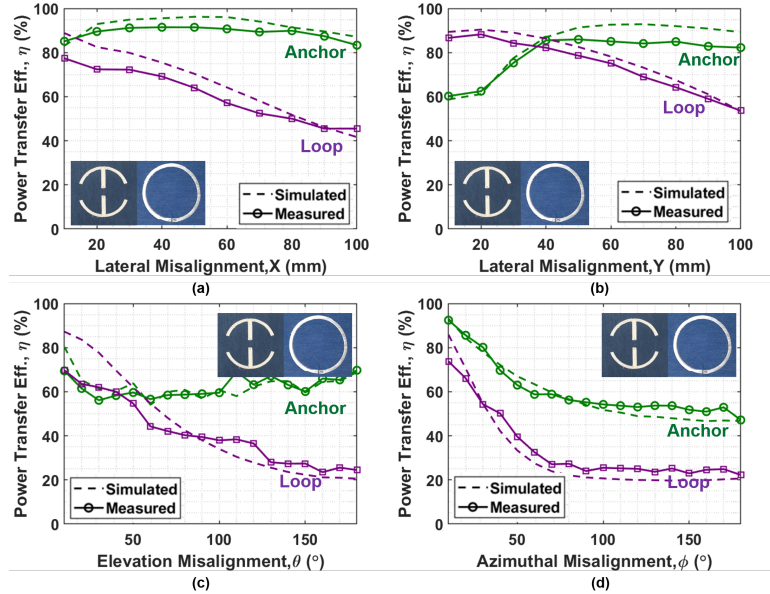
Figure 5.18: PTE performance of the textile-based anchor-shaped antenna compared to its single loop counterpart: (a) PTE performance when the Tx and Rx underwent lateral misalignments across the fringe-enabling cavities, (b) PTE performance when the Tx and Rx underwent lateral misalignments along the shank of the anchors, (c) PTE performance when the Tx and Rx underwent elevational misalignments, and (d) PTE performance when the Tx and Rx underwent azimuthal misalignments

resents a movement of 66% of the total size of the antenna. For these scenarios, the value of S_{11} was found to be around -19 dB at the resonant frequency.

The measured and simulated results agree quite well and further show that the PTE
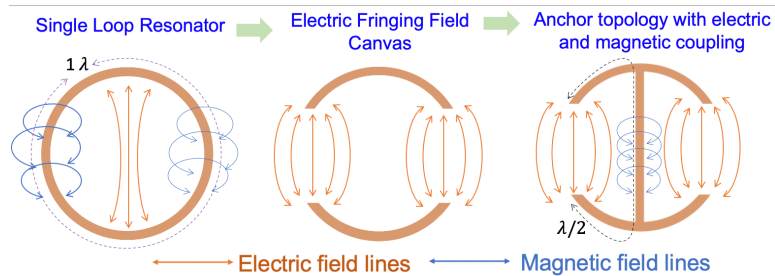
Figure 5.19: Evolution of the anchor topology from its single loop antenna. Single loop resonator represents the starting point. Electric fringe-enabling cavities introduced into the single loop. Resulting anchor topology is attained by using a central bar for ringing fields and increased resonance wavelength within the same area.

remains better than 38% and is found to be as high as 80%. Specifically, the anchor

shaped structure allows increased reach of fringing fields, and the PTE values remain high under wrapping and under misalignment cases. These results validate the misalignment resilience of the anchor shaped antenna which was previously reported for non-conformal or planar cases [65].

5.3.3   SAR Considerations of the Proposed Wireless Power Transfer

The influence electromagnetic fields in the near-zone of receiver antenna on the human tissue was characterized using full-wave simulation of the transmitter and receiver antenna. The receiver antenna was backed by a ferrite sheet to reduce human exposure to radiation. We noted only a nominal effect of the ferrite sheet on the S_{11} of the antennas and on the S_{21} between the antennas. The receiver antenna is placed near a human torso to evaluate the SAR (see Figure 5.22). Built-in torso model from HFSS was used for this simulation. The input power at the transmitter was chosen to be 1 W transferred over a distance of at least 6 inches to a surface area of 675 cm^2 (representing the receiver front). The maximum received power is close to 15 mW, which is well within the ICNIRP [123] limit of 1000 $\mu W/cm^2$ from 30 MHz to 400 MHz. Fig. 5.22(a) depicts the simulation setup and results are shown in Fig. 5.22(b). The evaluation was done for two cases, where the transmitting and receiving devices were laterally misaligned along the direction of (1) the shank and (2) the end-cavities (see Fig. 5.22(b)). As can be seen, when the antennas are laterally misaligned up to 10 cm, the maximum average SAR value of 0.3 W/kg was noted, and is found to be within the regulated limit of 0.4 W/kg [123].
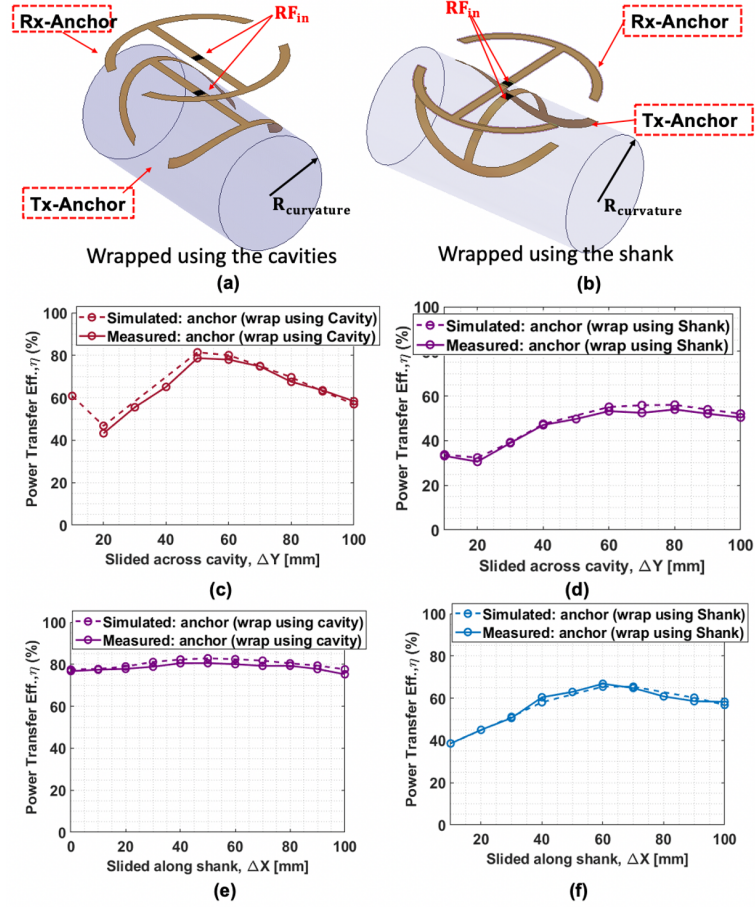
Figure 5.20: Influence of wrapping over cylindrical surfaces and lateral misalignments ($R_{curvature}$ = 37 mm) emulating wearable antennas wrapped over arms and legs (a) Wrapping along cavity (b) Wrapping along shank (c) Power transfer efficiency for case-(a) and movement along shank (d) Power transfer efficiency for case-(b) and movement along shank (e) Power transfer efficiency for case (a) and movement along the cavities (a) Power transfer efficiency for case-(b) and movement along the cavities.

5.4   RF to DC Rectifier Design and Optimization

The textile integration of rectifier requires a minimalistic approach while using only embroidered transmission lines and a small number of RF components. An RF-to-DC rectification circuit that uses transmission line resonances and a single rectifier diode was designed and fabricated. The goal was to minimize the number of RF

components in the circuit for an easy textile integration, while also to maximize the RF-to-DC power conversion efficiency.

5.4.1 Working Principle of the $\lambda_g/8$-Shorted Stub Rectifier

The circuit-representation of the rectifier is illustrated in Fig. 5.23(a). According to the work published in [124], the Schottky diode is a parallel circuit of an internal capacitor C_e and resistor R_e. The impedance of the diode is expressed as:

$$Z_{Diode} = \frac{R_e}{1 + (R_e C_e \omega)^2} - j\frac{R_e^2 C_e \omega}{1 + (R_e C_e \omega)^2}. \tag{5.19}$$

Placing a small capacitor in parallel with the diode will make the impedance of the circuit look like:

$$Z_{Diode+shunt} = \frac{R_e}{1 + (R_e C_{total} \omega)^2} - j\frac{R_e^2 C_{total} \omega}{1 + (R_e C_{total} \omega)^2}. \tag{5.20}$$

where $C_{total} = C_e + C_2$. To maximize the RF-to-DC conversion efficiency, the imaginary part of the diode impedance $\mathfrak{Im}(Z_{Diode+shunt}) = \frac{R_e^2 C_{total} \omega}{1 + (R_e C_{total} \omega)^2}$ should be matched with the impedance of a shorted stub. Therefore, the series $\lambda/8$-shorted stub is used to achieve the conjugate matching. The impedance of the shorted stub will depend on the frequencies that are multiples of the resonant frequency (f_r). The multiples of the resonant frequency are the harmonics and their orders can be labeled as $k = \frac{f}{f_r}$ where f represents the harmonics. The impedance of the shorted stub will be:

$$Z_{\lambda/8-stub} = jZ_l tan(\beta l) = jZ_l tan(\frac{\pi}{4}k) = \begin{cases} 0, & \text{if k} = 0 (DC signal). \\ jZ_l, & \text{if k} = 1 (Fundamental signal). \\ \infty, & \text{if k} = 2 (Second harmonic). \\ -jZ_l, & \text{if k} = 3 (Third harmonic). \end{cases} \tag{5.21}$$

The equation (5.21) suggests that the the second harmonic will be terminated due to the high impedance represented by the shorted stub. Therefore, the currents related to the second harmonics that will be flowing through the diode will be exponentially decayed. The third harmonics will contribute in making the diode more capacitive and any related current that will flow through the diode will be filtered away by the 33-nH DC pass filter (inductive counterpart). The expression of the impedance of the rectifying circuit will be:

$$Z_{rect.circuit} = \frac{R_e}{1 + (R_e C_{total}\omega)^2} - j\frac{R_e^2 C_{total}\omega}{1 + (R_e C_{total}\omega)^2} + jZ_l. \tag{5.22}$$

The conjugate matching will be achieved with $Z_l = \frac{R_e^2 C_{total}\omega}{1+(R_e C_{total}\omega)^2}$. At the resonant frequency, the value of C_2 will be tuned to make:

$$Z_{rect.circuit} = \frac{R_e}{1 + (R_e C_{total}\omega)^2}, \tag{5.23}$$

which should be significantly small with respect to the load resistor ,Z_{load} to achieve high RF-to-DC conversion efficiencies.

$$Z_{rect.circuit} = \frac{R_e}{1 + (R_e C_{total}\omega)^2} << Z_{load} \tag{5.24}$$

. The fact that the topology considered in this work is a single-diode, when $Z_{rect.circuit} = Z_{load}$, the maximum power transfer will be capped at 50% as the RF-to-DC conversion efficiency depends on the ratio $\frac{Z_{load}}{Z_{rect.circuit}+Z_{load}}$. Therefore, a very significant decay in $Z_{rect.circuit}$ will help achieve an RF-to-DC conversion efficiency up to 95% for lossless circuits. The efficiency will slightly decrease based on the loss factor of the circuit. As shown in the prior works [122], these features are realizable by using a resonant shorted transmission line section and by positioning a capacitor connected in parallel with the rectifying diode (see Fig. 5.23(a)). The length of the transmission line was optimized to be $\lambda_g/8$ to achieve this effect. A DC block capacitor C_1 is added at the input, while L, and C_2 were optimized for a 50 Ω input impedance
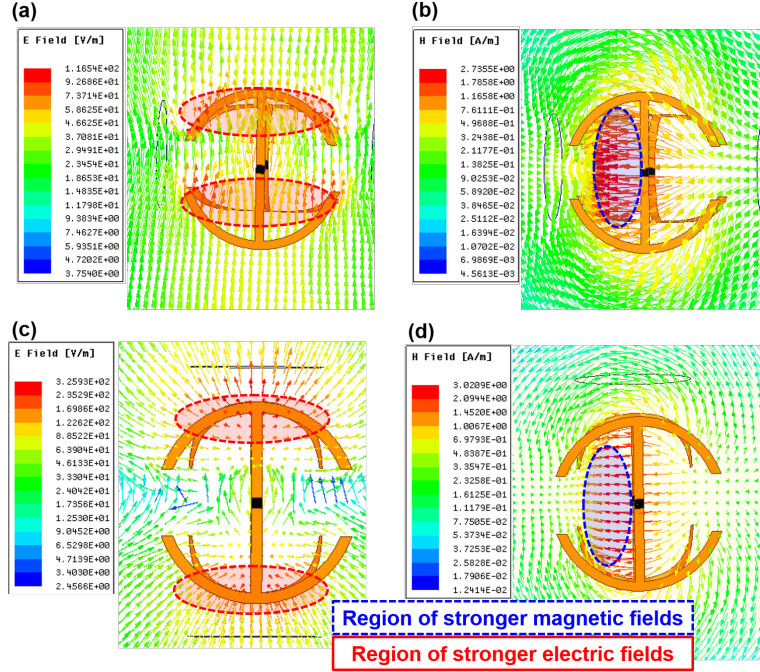
Figure 5.21: Field distribution resulted from wrapping the antenna over cylindrical surfaces and lateral misalignments ($R_{curvature} = 37$ mm) emulating wearable antennas wrapped over arms and legs (a) E-fields resulted from wrapping using the crown of the anchor , (b) H-fields resulted from wrapping using the crown of the anchor, (c) E-fields resulted from wrapping using the fringe-enabling cavities of the anchor, and (d) E-fields resulted from wrapping using the fringe-enabling cavities of the anchor.

along with high RF to DC power conversion efficiency at 360 MHz. The choke inductor L was used to remove the ripples from the output DC waveform. For illustration, the design and measurements were conducted with a resistive load of Z_{load} = 683 Ω, however exact load conditions will be subject to the output devices, such as IoT/IoHT, wearable sensor or rechargeable super-capacitor which are connected at the output of the rectifier. The values of these RF components are summarized in Table 5.1. After optimizing the components and lengths of transmission lines in ADS circuit simulation software, the rectifiers were implemented on a denim textile substrate (see Fig. 5.23(b)). The conductive regions were realized using embroidery of conductive threads on the substrate. A conductive thread, Elektrisola-7, consisting of silver-coated copper strands (Cu/Ag50 amalgam), was used for the
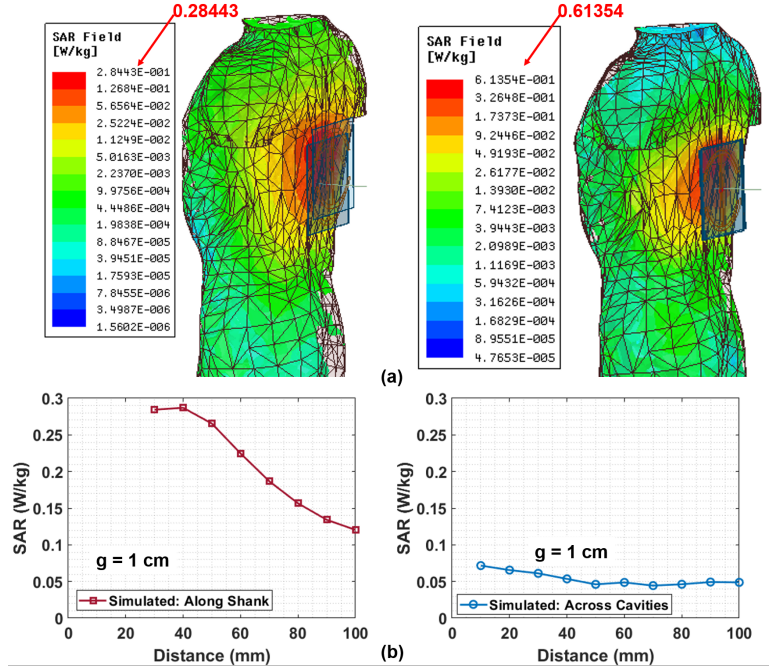
Figure 5.22: SAR evaluation of the system when it is subject to both lateral misalignments namely along the shank and across the cavity: (a) Photo of the human model with extracted SAR value and (b) SAR values extracted from human model for various misalignment distances (input RF power = 1 W).

embroidery process. Details of the the embroidery steps can be referred from the prior works [125, 77, 122].The measurements were conducted by providing an RF signal of frequency 360 MHz with power level changing between 0 dBm and 32 dBm (Fig. 5.23(d), (e)). The simulated and measured results show a good agreement. This agreement is better than some of the prior comparisons, as we used a non-linear model for the diode in ADS, which was available from the vendor. The required input signal was achieved using a Keysight MXG signal generator (N5183B) and power amplifier (Mini-circuits ZHL-20W-13+). The output of the rectifier, the DC voltage waveform, was recorded through a mixed signal oscilloscope (MSOS254A). The waveforms showed almost flat output voltage with no ripples, which was then used to calculate the output DC power from the rectifier using V^2/Z_{load}.
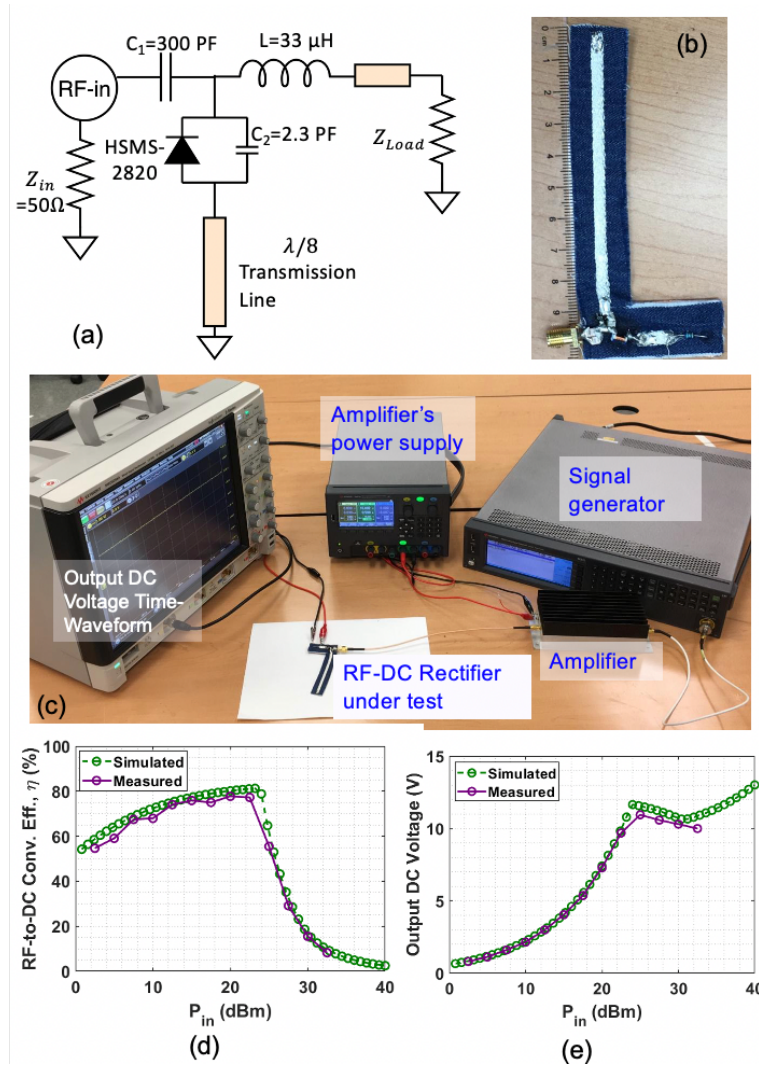
Figure 5.23: Fabric-based RF to DC conversion rectifying circuit made of conductive thread embroidered onto fabric substrate (a) Circuit diagram of single diode rectifier using transmission lines (the circuit is powered by a 50-Ω RF source) (b) Fabricated prototype using denim substrate (c) Measurement set-up used for rectifier efficiency characterizations (d) Simulated and measured efficiency as a function of RF input power and (e) Simulated and measured collected DC voltage as a function of RF input power.

The power conversion performance of the rectifier is shown in Fig. 5.23(d) and as shown, a peak of 77.27 % of RF-to-DC conversion efficiency was achieved at around 22.5 dBm input. Beyond input power of 22 dBm, the voltage level was found to be at least 10 V (Fig. 5.23 (b)). The comparison with state-of-the-art is done in Table

91

Table 5.1: Optimized parameters of the textile-based rectifying circuit based on a $\lambda_g/8$-short-circuited stub

C_1	300 pF (DC block)
Operating Frequency	360 MHz
C_2	2.3 pF (tuned for diode impedance matching)
Z_{Load}	683 Ω (optimized for high power collection)
L	33 μH (RF choke)
Diode	HSMS2820 (for medium power rectification)
Substrate	denim ($\epsilon_r = 1.67$ and tan$\delta = 0.07$)
Conductive surfaces	Elektrisola-7 ($\sigma = 2.44 \times 10^6$ S/m [122])
Length of TL	$\lambda_g/8$* (for 360 MHz)
Skin depth, δ	17μm (for 360 MHz)

*$\lambda_g/8 = \lambda/(8\sqrt{\epsilon_r}) = \lambda/(8\sqrt{1.67}) = 8.06$ cm

4.3. To the authors' knowledge, this is the highest RF-to-DC efficiency reported for a textile-based rectifying circuit. Moreover, we note a 50%, 60%, and 70% of RF-to-DC conversion efficiency at the input power range values of 26 dB, 22 dB, and 14 dB, respectively. These results are comparable or better than the current state-of-the-art reported in prior works (see Table 4.3).

5.5 System Design and Tests using RF Rectifier and Anchor Shaped Antenna

5.5.1 An Illustration of Ergonomic Wireless Power Transfer

Having optimized the misalignment resilient antenna and corresponding rectifier for RF to DC rectification, we consider the performance of the textile integrated rectenna system using these components. Specifically, first the ergonomic nature of
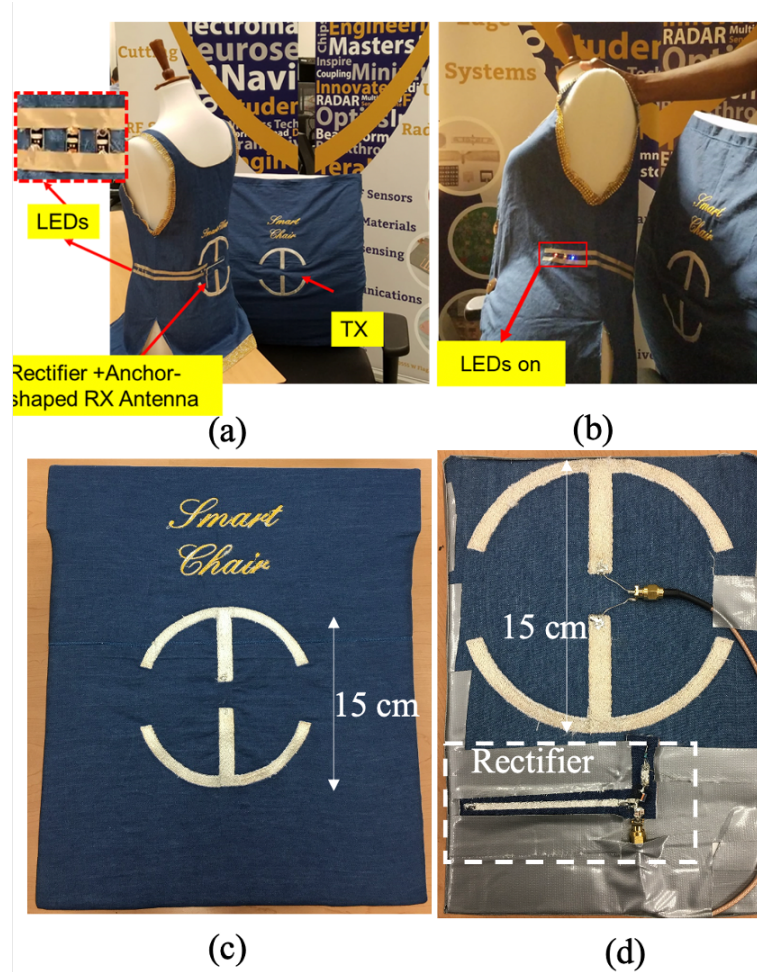
Figure 5.24: Illustration of practical use of the ergonomic wireless charging platform (a) Fabric embroidered antenna and rectifier circuits in dressing and chair upholstery (b) LEDs turned on under wireless powering and under misalignments (c) Close-up photograph of the transmitting antenna (d) Close-up photograph of receiver antenna and rectifier circuit.

the set-up is illustrated for a user seated in a chair with rectenna receiver integrated in her item of clothing (see Fig. 5.24). Notably, due to textile nature of the antenna substrate, and due to a conductive fiber based antenna and circuit fabrication techniques, such an integration is now possible. Likewise, the transmitter antenna is embroidered in the upholstery of chair. The close-up photographs of the transmitter antenna and receiver rectenna are shown in Fig. 5.24(c) and (d), respectively.

To illustrate the wireless power transfer, three LEDs were connected in parallel to the output DC line of the rectifier [126]. As shown, the LEDs were lit when the receiver was in the vicinity of the transmitter and for the cases when the receiver underwent misalignments. Total transmit power of about 1W was used for this experiment. The misalignments were done by rotating and laterally translating the receiver as shown in Fig. 5.24(b). This experiment serves to demonstrate the usefulness of the proposed ergonomic wireless charging system and successful operation of the receiver antenna and rectifier circuits.

5.5.2 Quantitative Power Collection Set-up

To quantitatively characterize the performance of the system, we conducted elaborate experiments to measure the wireless power transfer in the inductive near-field and radiative near field regions of the transmitter antenna. The performance of the receiver in a very close proximity (1 cm to 10 cm) of the transmitter antenna has been covered in the prior works [65, 126]. In this work, we aim to learn if a user could walk around in the vicinity of the transmitter antenna, while allowing wireless power transfer through the wearable surfaces. These determinations are made by collecting power under exaggerated misalignment between the transmitter and receiver antennas, ranging up to 4 ft. from the transmitter and 2 ft. of lateral shifts.

The adopted set-up for this measurement is shown in Fig. 5.25. The power transmitter (Tx) was positioned at the edge of the grid and was stationary. The transmitter consisted of Keysight MXG signal generator (N5183B) and power amplifier (Mini-circuits ZHL-20W-13+) which provided a total output power of about 1 W. The receiver antenna was placed at translating locations, each 6 inches apart, covering an area of 4 ft. × 4 ft. (see Fig. 5.25(b)). We note that, in practical setting

(as shown in Fig. 5.24), the receiver antenna's plane may rotate with respect to the transmitter antenna's plane. Therefore, we consider two cases. That is, we consider the cases with receiver antenna placed in parallel with and perpendicular to the transmitter antenna. Received power or voltage information for an arbitrary angle can be interpreted by knowing these two orthogonal cases.
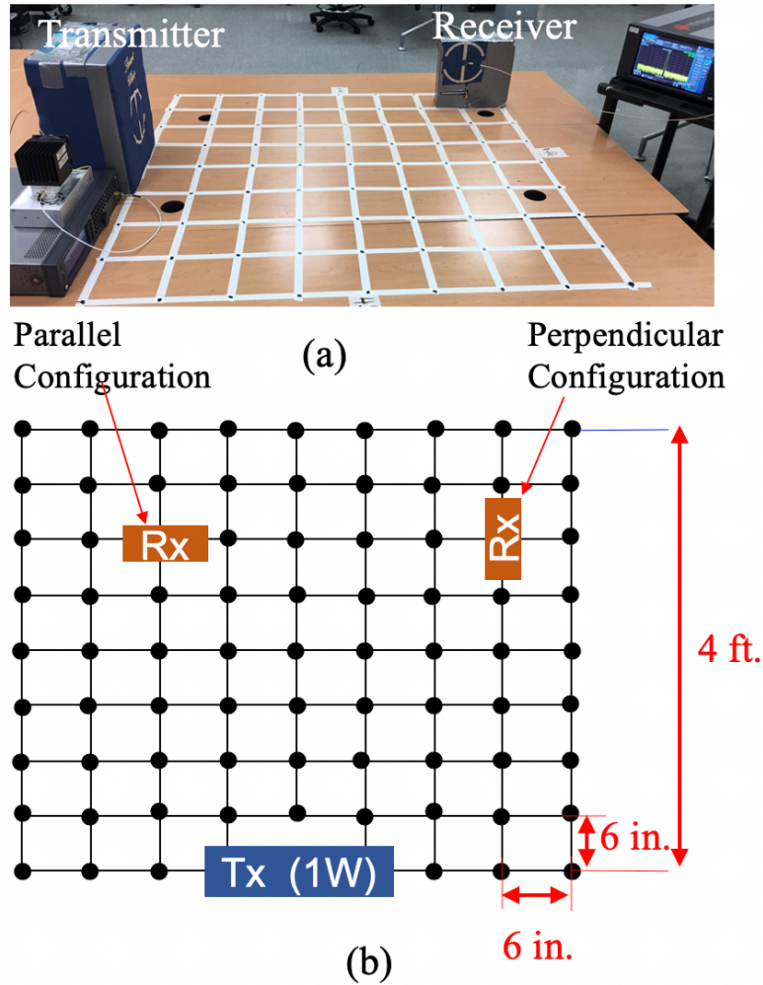
Figure 5.25: (a) Photo of the measurement set-up with 2D grid where the receiver was translated for individual measurements (b) Schematic of the 2D grid, perpendicular / parallel configuration and dimensions of the grid points used for the measurements.
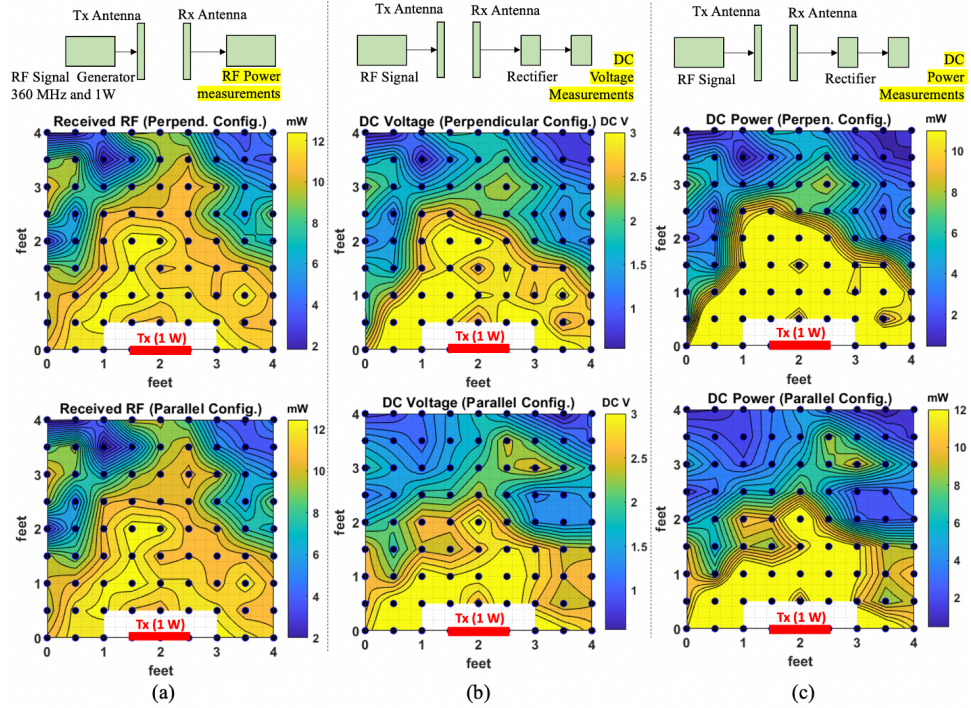
Figure 5.26: Measurement of the RF power, DC voltage (using RF-DC rectifier shown in) and DC power across 2D region in the front of the transmitter antenna. The black marker points represent the measurement points, while the colors in 2D region represents the interpolated values. (a) RF power recorded using a spectrum analyzer (b) DC voltage recorded using a multimeter (c) DC power measured calculated by V^2/R, with $R = 683\ \Omega$.

5.5.3 Measurement Results

The tests characterized the RF power received by the receiver antenna at each of the grid points. To test the efficacy of the rectifier in providing a DC output, measurements were also conducted for rectifier's output of DC voltage and DC power. These measured values, as a function of 2 dimensional space, are provided in Fig. 5.26. RF power measurements are shown in Fig. 5.26(a), while rectified DC voltage and DC power measurements are shown in Fig. 5.26(b) and (c), respectively. First we consider Fig. 5.26(a). As shown, above 10 mW of power is recorded by the receiver within a distance of 1.5 ft. normal distance from the transmitter antenna. Remarkably, the power levels remain > 10 mW across 4 ft. of lateral region at 1.5

ft. normal distance from transmitter. Further, at a normal distance of 2 ft., 12 mW power is received by the antenna. The power decrease to about 2 mW, when we move away to a normal distance of 4 ft. from the transmitter antenna. We also note that the orientation of the receiver antenna has rather small impact on the collected power, as we compare the top and bottom 2D plots in Fig. 5.26(a).

Next in Fig. 5.26(b) and (c), we present the output of the antenna + rectifier circuit of Fig. 5.23. The output voltages were recorded and found to be up to 3 V in the vicinity of the transmitter, which is relevant for the state of the art IoT sensors and charging devices. Note that the output voltages can be increased by using multiple diode based rectifiers for voltage multiplication [127]. The corresponding DC power was calculated using $P = V^2/R$ with $R = 683\Omega$ as shown in the Fig. 5.26(c). Furthermore, we note that the rectified DC power is in the same order as the RF power collected by the antenna. Notably, between 0 and 2 ft., the incident RF power is around 10 mW to 12 mW (or 10 dBm to 11 dBm). At this input power level, the rectifier efficiency is close to 60% (see Fig. 5.23), allowing around 6 to 10 mW of DC power availability. This verifies the power conversion efficiency of the rectifier. Overall, this verifies that for a 1-W transmitter, the choice of diode and components (which determines the efficiency for a given input power) is well optimized for wireless power collection at up to approximately 2 ft. from the transmitter. We note that received power levels are of interest for low-power wearable sensors and IoT devices [13, 14]. Power consumption of these devices is in pW to μW range and therefore the proposed wireless powering through daily life activities is appropriate for wireless powering or charging these devices. Specifically, low-power devices, such as temperature sensors with power consumption between 113 pW and 1.4 μW [15, 16, 17, 18, 19], current and voltage sensors as well as biosensors with power consumption of 9.3 nW and 436 μW [20, 21, 22, 23] are already

reported in prior works. Furthermore, the collected DC power level is enough to power ECG monitoring system, pulse oximeters, or neural recording systems with typical power requirements between 5 to 12 mW [128, 129, 130].

5.6   Conclusion

In this chapter, a new class of misalignment-resilient antenna topology referred to as anchor-shaped is proposed. It allows for both lateral and angular misalignments within the ranges of 1 cm to 10 cm as well as 10° and 180°, respectively. With respect to its single-loop counterpart, the PTE performance of the proposed anchor-shaped antenna is better and that of the single-loop antenna experiences a rapid decrease. The excellent performance of the anchor-shaped antenna is due to the fringe-enabling cavities that are introduced in the structure , which boots both electric and magnetic coupling modes that are responsible for high and stable PTEs. This design is very well suitable for contact-less and misalignment-free wireless charging applications.

The antenna topology was used to developed wireless charging platform that is embedded into clothing to be used by patients with charging needs for the devices, medical professionals to charge their wearable devices while focusing on saving lives, and general consumer electronics to charge their everyday wearable/portable devices. The charging platform uses a transmitter that can be integrated into the upholstery of bed, chair, wheeled chair, bedsheets, mattresses, benches, walls, ceiling, and floors. These transmitters are set to transmit a maximum of 1 W [per FCC/FDA regulations] The receiver is embedded into clothing items when the power reception and harvesting is done and the DC power collected was found to be up to 10 mW which is enough to drive a wide range of IoT devices.

CHAPTER 6

SMART BANDAGE FOR ELECTROCHEMICAL DETECTION VIA ELECTRONIC DATA MODULATION

6.1 Introduction

In this chapter, a smart bandage is demonstrated for remote monitoring of chronic wounds. This assessment was made possible using fabric-integrated data modulation through the "transmit-reflect" principle. The latter suggests the use of an interrogator that transmits an RF signal to the smart bandage, which at its turn, will respond to the interrogator via its textile-based voltage-controlled oscillator (VCO). The VCO takes the electric signal given by an electrochemical sensor detecting the level of uric acid found in the wound bed. Based on the uric acid concentration, the VCO will output a signal with a specific frequency that will be used for the assessment based on the 0.4-mM threshold reported to gauge the severity and the restoration of the damaged tissue. The work presented in this chapter starts with an exhaustive survey on smart bandages used for the treatment/healing status of chronic wounds (Section 6.2), followed by an overview of the proposed generation-1
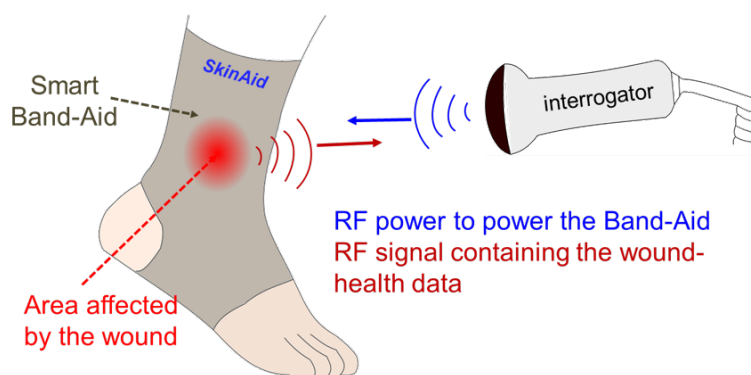
Figure 6.1: Smart bandage that responds to an interrogator power signal by reflection of the data-signal containing the wound-health data back to the interrogator.

smart bandage (Section 6.2.1), the proposed generation-1 smart bandage (Section 6.2.5), and concluded by the system integration and testing close to an "in-vivo" setting (Section 6.2.8).

6.2 A Survey on Chronic Wounds and Smart Bandages For Wound Monitoring

Chronic wounds carry with them various complications including difficult/lengthy healing process, very expensive- $25B spent in wound care annually in the United States [131], long-term immobility, infection, and hospitalization. Therefore, close attention should be paid to such health problem as it can yield amputation when it is in conjuction to diabetes [132] or even cases of death. According the National center for Health Statistic, chronic wound is the 7th cause of death in the United States [133]. Therefore, effective and adaptive therapeutics can yield healing improvement, better quality of life, and healthcare cost reduction. Among the adaptive therapeutics are the smart bandages where wound healing status and treatment modalities are incorporated. For reliable use, the bandages are supposed to be sensitive, selective, stable, and mechanically robust to assure durability [134]. The most crucial part of the bandage is the sensor that detects the biomarkers. So far, the selected biomarkers have been the pH of the wound, its temperature, its oxygenation, its moisture, its enzymes, and its level of uric acid [135, 134, 136]. The latter has been proven to be an indicator of the severity of the wound [69, 70]. Seizing this opportunity, several smart bandages have been developed to assess the wound healing process using uric acid monitoring [134, 136].These smart bandages consisted of using an electrochemical sensor to detect the level of uric acid. The output of the sensor is connected to a potentiostat to enable NFC or RFID communication

[136], RF transceiver, and micro-controller Arduino added atop the potentiostat to extract the wound-data [134]. It can be noted that the electronics incorporated into the bandage made of PCB, which yields discomfort to the patient, use coin cells or Li-ion batteries to power the sensor and the rest of circuitry. As a result, the power consumption is a challenge to tackle. To resolve this issue, developing a system that can seamlessly monitor the wound by characterization the concentration of uric acid using bio-sensing would be the best solution. This system can use wireless powering method and on-fabric simplistic circuitry to realize smart sensing systems with low-power consumption. If developed, this improvement would help patients overcome their financial burden, healing process (fast recovery), and a better quality of life. However, these bandages use Li-ion batteries to power the circuitry used to operate the bandages. The latter also feature some complex and rigid micro-controller circuits that are power hungry that cannot be integrated into clothing. To make that possible, we proposed a voltage controlled oscillator (VCO)-based sensing of wound health towards a flexible, fabric integrated and wireless wound monitoring system (Fig. 6.1). Using this system, the characterization of the wound fluid for can be conducted to determine by measuring the uric acid concentration found in the fluid. For integration into the band-aid, the circuit is developed on a fabric substrate, which allows possible band-aid integration for comfort, flexibility, and wearability of the sensor. Furthermore, in the proposed concept, the sensor is designed to be powered from an incident radio frequency signal remotely given by a nearby interrogator, which will enable transmit-reflect type operation of the sensor. This operation features a very critical circuit, the voltage-controlled oscillator that converts the return DC voltage given by the sensor into a (frequency) modulating signal that is sent back to the interrogator. In this work, a benchtop solution of the smart bandage is demonstrated by consuming 0.38 mW of power and the average

101

sensitivity was 44.67 MHz/mM. This smart system uses low-cost material (gauze fabric) and is easy to fabricate and user-friendly (can be used by non-tech savvy individuals like elderly patient, nurses, etc).

To respond to this need, we propose a voltage controlled oscillator (VCO) based sensing of wound health towards a flexible, fabric integrated and wireless wound monitoring system (Fig. 6.1). The VCO will be able to replace all the electronics added on top of the sensor for a simpler, more cost-efficient, easy to fabricate, wirelessly powered, and compact monitoring platform. Using this system, the characterization of wound fluid for can be conducted to determine by measurement of uric acid content in the wound fluid. For integration into band-aid (see Fig. 6.2), the circuit is integrated on a fabric substrate, which allows possible band-aid integration for comfort, flexibility and wearability of the sensor. Furthermore, in the proposed concept the sensor it is designed to be powered from an incident radio frequency signal remotely, which will enable incident-reflect type operation of the sensor (Fig. 6.1).

6.2.1 Generation-1 Smart Bandage

A system diagram of the envisioned wireless wound monitoring system is shown in Fig. 6.1. The proposed system will use an interrogator, which will transfer wireless RF power, to be received by the fabric-based antenna integrated in the bandage. An RF to DC rectifier circuit, which is based on a flexible textile substrate, will be used to convert the received RF power into DC voltage. The obtained DC power will be used to power uric acid sensor and voltage-controlled oscillator to modulate the DC output from the sensor into an RF frequency. The frequency of the RF signal from the VCO will be a function uric acid concentration. The generated RF

signal will be transmitted back to the interrogator device transferring the wound data back to the interrogator. In this work, here we will demonstrate the feasibility
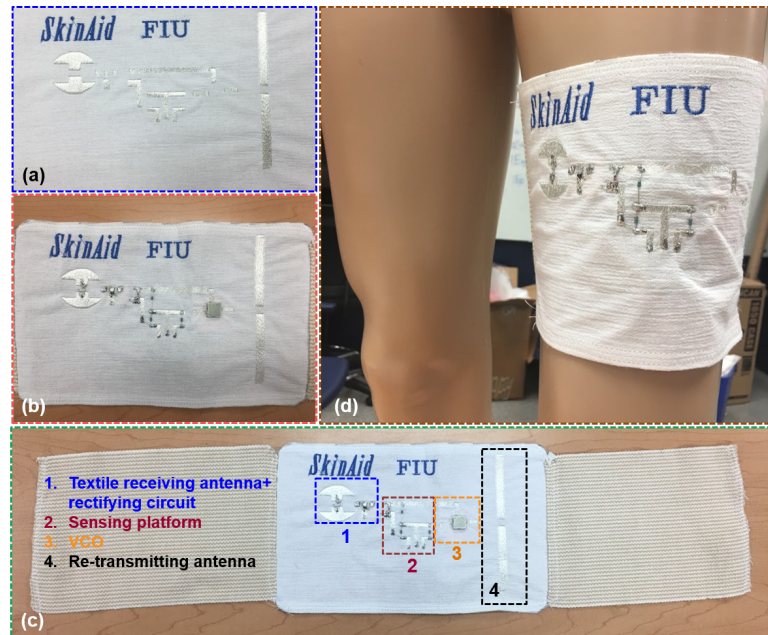
Figure 6.2: Our recently developed smart bandage: (a) a freshly embroidered sample of the bandage, (b) complete circuitry of the bandage, (c) final look of the bandage with all the circuitry responsible for receiving the RF power from the interrogator and converting this RF power into DC using a rectifier (1), the sensing platform for uric acid detection (2), a voltage-controlled oscillator to convert the DC output of the sensor into RF signal (3), and the re-transmitting textile antenna to reply back to the interrogator (4), and (d) the illustration of the smart bandage on someone's leg.

and operation of textile integrated VCO based wireless sensor, which may be used for developing the system shown in Fig. 6.1.In this work, uric acid is used as the biomarker and its characterization is done by electrochemical sensing (see Fig.6.2 (2)). The sensor used is a textile-based enzymatic sensor inspired from [35]. The sensor will be powered by the textile-based rectifier and after sensing the uric acid concentration, will send the wound information in the form of an electric signal that is fed in the textile-based oscillator, which at the end modulate the wound-data in the form of frequency that is communicated back to the interrogator. In the next

sections, the electrochecmical sensor, the VCO, and a bench-top version of the smart bandage will be presented and discussed.

6.2.2 Textile Based Voltage-Controlled Oscillator (VCO)

The VCO circuit was designed using a Crystek CVCO055BE and realized on a flexible fabic substrate by using embroidery of conductive thread (Elektrisola-7) onto a gauze fabric ($\epsilon_r = 1.67$ and $\tan\delta = 0.07$) and can be seen in Fig. 6.3. The

Circuit diagram of the VCO   **Finished prototype**
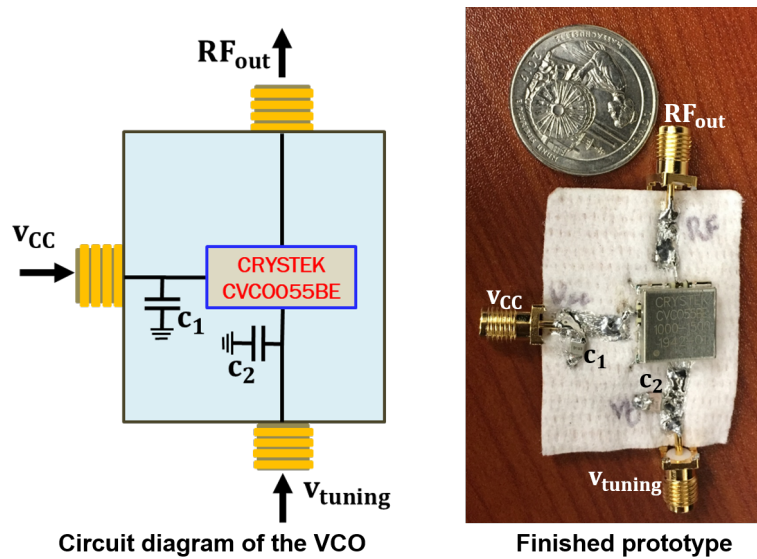
Figure 6.3: Circuit representation of the VCO and its corresponding finished prototype.

circuit and implementations are shown in Fig. 6.3. The embroidery was done using Brother sewing machine, which uses automated CAD design method to implement a desired pattern of conductive traces. The voltage controlled oscillator chip, Crystek CVCO055BE was used to convert the DC output level obtained from the sensor to an oscillating RF frequency for data-modulation. The capacitance $C_1 = 1$ nF, and $C_2 = 10$ nF, and the $V_{CC} = 3.14$ V (and 10.479-mA current) were used to calibrate the IC for operation based on the desired output and input. To test the IC's performance

on a fabric substrate, we varied the control voltage from $V_{tuning} = 0$ to 6.2 V (and 4-μA current) in order to emulate a feedback of the electrochemical sensor due to changing concentration of uric acid present in the wound fluid. The DC voltage was given using a Keysight E36312A power supply (see Fig. 6.4 (right)). The current
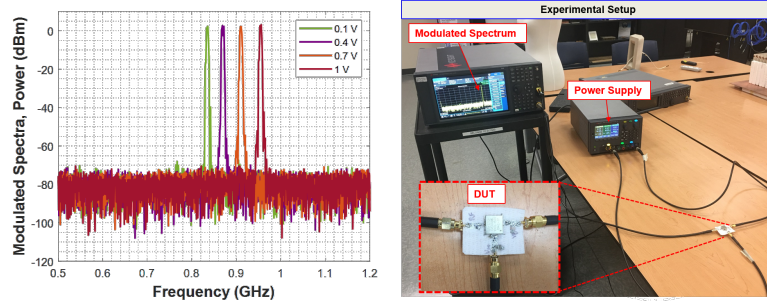
Figure 6.4: Experimental setup and results from the VCO characterization: (left) modulated spectra from frequencies obtained from tuning the VCO from 0.1 to 1 V and (right) the experimental setup

drawn by the IC was recorded to be 10.5 mA. Therefore, power requirements of the operation were within 33 mW. A comparison of the output frequency obtained in experiments with the IC's normal operation based on the equation

$$f_{VCO}(MHz) = 836 \times \left(1 + asinh \left(\frac{2C_1}{C_2} \times V_{CTRL} \right) \right) \quad (6.1)$$

where the related results and measurements are provided in Fig. 6.3(left). The
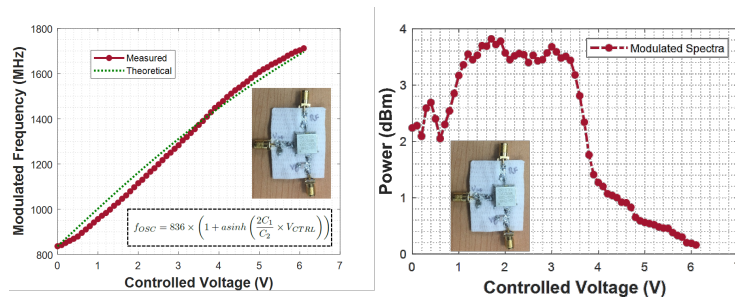
Figure 6.5: Measured results of the characterization of the VCO: (right) measured output modulated frequency of the VCO and (left) Power level of different spectra recorded from frequency modulation.

V_{tuning} was varied from 0 to 6.2 V,the output modulated frequency (f_{VCO}) was measured to be between 836 MHz and 1.712 GHz. The spectra associated to these frequencies were measured using a Keysight PXA signal analyzer N9030B and were between 0.15 dBm and 3.8 dBm (see Fig. 6.5 (right)). There is agreement between the theoretical and measured values showing an expected operation of the VCO for the sensor-integration application. The experiment shows that flexible substrates may be used for near perfect operation proving its utility for fabric-integration.

6.2.3   Textile based Enzymatic Sensor

A 3-electrode flexible enzymatic sensor was designed and fabricated, as shown in Fig. 6.7. The there electrodes, namely counter electrode (CE), reference electrode (RE), and working electrode (WE) are used to connect the input and output of the sensor while the sensor is exposed to the test fluid (Figs. 6.7 & 6.6). In the experimental demonstrations, the wound fluid is emulated by using uric acid solutions of varying concentration (as further discussed in Section 6.2.4). An electric potential of -0.6 V was used to power the sensor using the electrodes CE and RE. The feedback of the sensor on the uric acid detection is given in the form of an electric current whose theoretical model is

$$i_{Feedback}(\mu A) = 6.234 + 0.338 \times log_2(0.985 \times C_{UA}) \qquad (6.2)$$

and measured across the RE and WE, where a resistance of 350 kΩ is placed in parallel. The resulted voltage is used as (V_{tuning}) for the VCO.

6.2.4   Wound Assessment Using Data Modulation

The feasibility of VCO based sensor for wound monitor data modulation for RF transfer is tested by conducting a bench-top experiment (see Fig. 6.8), in which
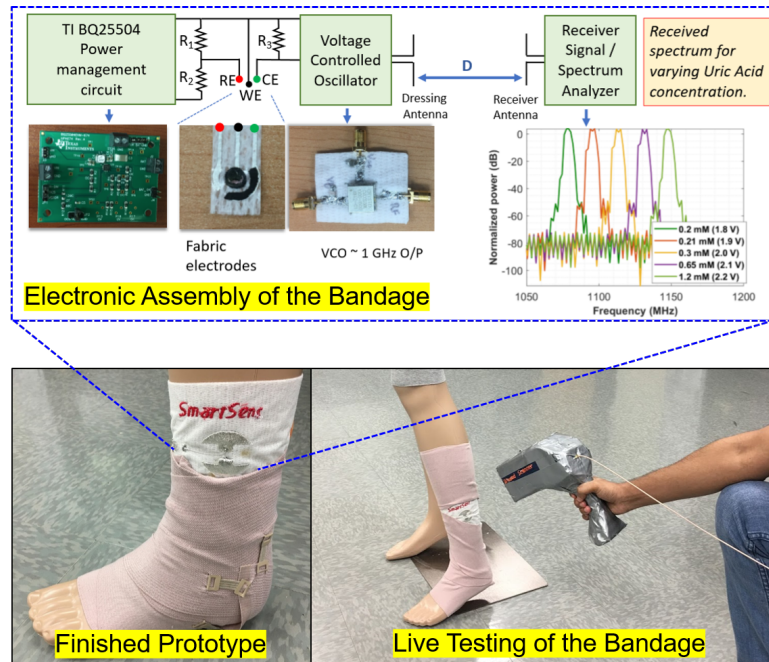
Figure 6.6: Photos of the proposed smart bandage responding to an interrogator by responding back to the interrogator with a modulated signal of the wound-data (Bottom left) finished prototype of the bandage, (Bottom right) live testing of the bandage based on the layout (zoomed-out on Top).

DC power source is connected to a TI BQ25504 power management system, which would provide a constant input to the uric acid sensor while also powering the VCO IC. The DC source emulates the power received from a rectenna, powered from a wireless power transmission source. In addition to the PMC it contains the sensor, the VCO, and a pair of 915-MHz microstrip patch antennas distanced by 25 cm, used for power reflection back to the interrogator, Keysight PXA signal analyzer. This is the equivalent of a testing system where the proposed smart bandage is illuminated by a scanner (interrogator). The tests are conducted by using uric acid solutions of different molar concentrations to understand sensor's modulation capability in relation to practical molar values in wound. Figs. 6.6 & 6.7 show the experimental setup for this wound assessment test. In this set up, the TI BQ25504 ultra low power boost converter uses a voltage divider to assure a constant voltage of -0.6 V (as
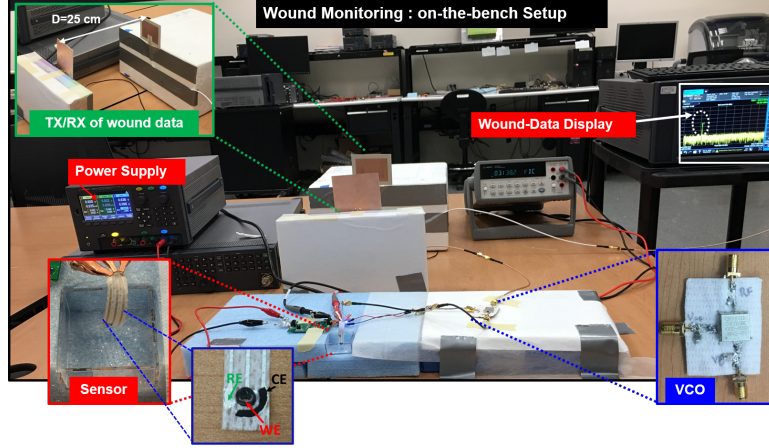
Figure 6.7: Bench-top setup of the proposed smart health system developed with the integration of on-fabric circuits emulating the wound healing assessment

suggested in [35]) is being delivered to the sensor. This power management circuit is to be replaced by a constant out put rectifier in future work in this direction. The latter used a bias power of 10 mW from a keysight E36312A triple output programmable DC power supply. The sensor is dipped into a container of uric acid molar solution at different concentrations. The VCO was supplied 0.38 mW by the power management circuit (BQ25504). The frequency modulation was evaluated for uric acid of concentration ranging from 200 μM to 1 mM. The feedback voltage from the output of the VCO ranged from 1.875 V to 2.15 V following the equation

$$V_{tuning}(V) = 2.175 + 0.105 \times log_2\left(0.235 \times (C_{UA})^{0.205}\right). \tag{6.3}$$

The feedback of the sensor was also recorded using a Keysight U1242B true RMS multimeter. Measured results this can be seen on Fig. 6.8 (b). The wound-data provided by the VCO is captured using a Keysight PXA signal analyzer N9030B showing the spectrum for uric acid level and the corresponding equation is:

$$f_{Bandage}(MHz) = 1121.256 + 12.365 \times log_2\left(0.965 \times (C_{UA})\right). \tag{6.4}$$
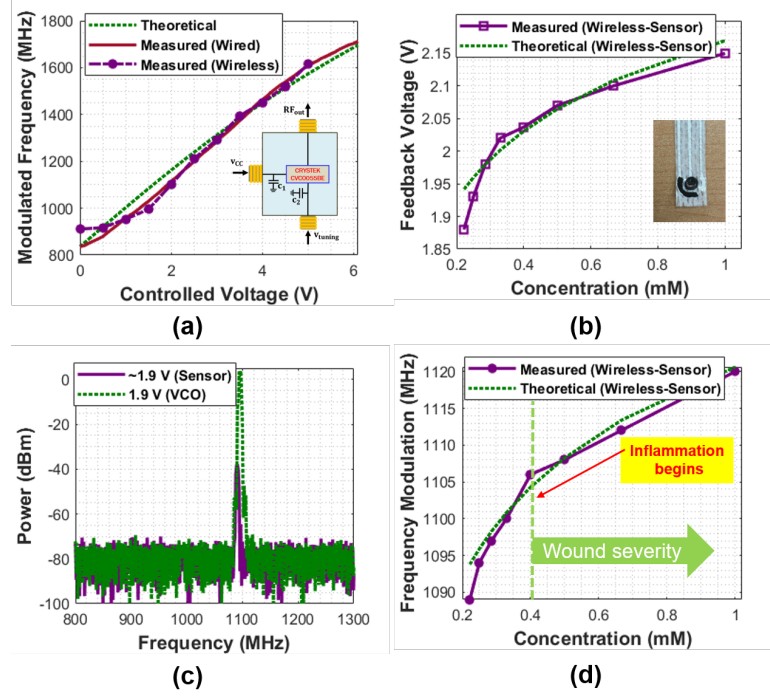
Figure 6.8: Performance of the benchtop solution of the smart bandage: (a) wireless and wired performance of the textile-based VCO compared with its theoretical model, (b) Feedback response of the electrochemical sensor, (c) Spectra representing the output of the VCO along with that of the sensor+VCO, and (d) Measured and theoretical models of the wound assessment using the smart bandage.

The spectra are shown in Fig. 6.8(c) and Fig. 6.8(d) translates the shifting of the spectral peak with changing levels of uric acid concentration. The variation of VCO's output frequency spectral peaks are shown in Fig. 6.8(b) with changing molar concentration (C_{UA}) levels. The signals from the modulated frequency were re-transmitted back to the interrogator at 25 cm using a pair of 915-MHz antennas. The signals can also be received by any remote receiver like a phone, tablets, and a computer. An important parameter is the sensitivity of modulated data with changing uric acid concentration, which is calculated to be 44 MHz/μM. This sensitivity is adjustable by changing the ratio of resistors C_1 and C_2. The total power consumed by the sensor alone is 24 μW. To parameterize the assessment of wound healing sta-

tus based on an obtained frequency, an equation was developed by curve fitting of the experimental data. Two model were developed. The first model represents the relation between uric acid concentration C_{UA} in millimolar (mM) with the applied voltage V_{CTRL} in Volts (V) as can be seen in equation(6.3). The second represents the modulated frequency ($f_{Bandage}$) in MHz as a function of the variable uric acid concentration (C_{UA}) and displayed in equation (6.4). These equations can be used for quick and reliable assessment of the wound. Because of these unique attributes, this smart bandage seems appealing to customized and personalized care because of its cost-efficiency, ease to fabricate, and the theoretical model used for quick and reliable assessment.

6.2.5   Generation-2 Smart Bandage

previously published electrochemical monitoring wearable solutions are battery powered and / or consisted of transceiver ICs for transmittance of the modulated signal to a remote receiver. These solutions lead to bulky and uncomfortable-to-wear electronics [137, 138, 139] on human body. New wearable devices will require textile integration with minimalistic electronics [with the ability of being integrated into a single chip]. Therefore, a potential solution should cater to challenges of (1) wireless illumination, (2) wireless data transfer and (3) conformable and low-profile clothing-integratable electronics. To do so, a robust frequency modulation-based RFID modality is proposed [consisting of a transmit-reflect module], which directly modulates the sensor-data and reflects frequency-modulated signals [with the help of a voltage-controlled oscillator] to a remote location. A remotely-powered, smart dressing solution used to reduce battery requirements, while frequency data-modulation and signal reflection are used for robust electro-chemical assessment of
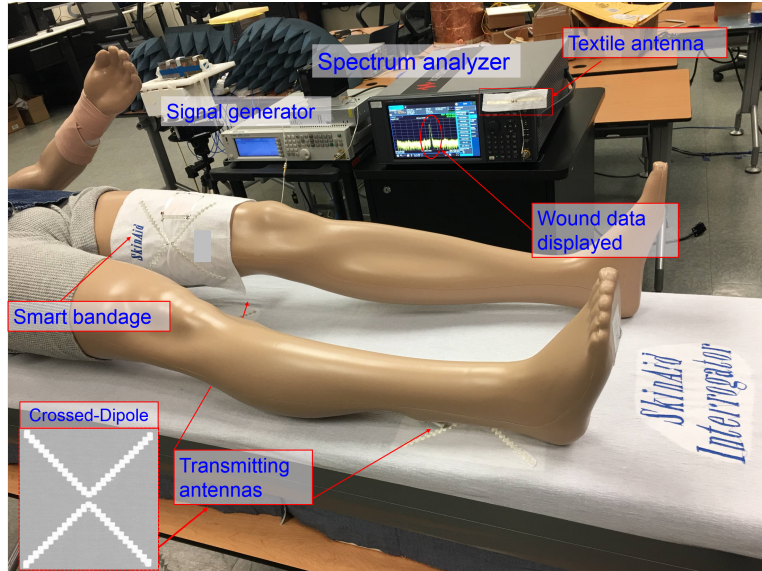
Figure 6.9: Complete wirelessly powered system representing the smart bandage with all the different components. Wound data to be collected at more than 3 ft. away from the bandage by the textile antenna (attached to the spectrum analyzer)

chronic wounds (see Fig.6.9). In this new experiment, we demonstrate the performance of a battery-free electrochemical sensing platform, integrated on fabric-surfaces with wireless power transfer and harvesting for health assessment. We present a fully-functional setup for wound monitoring consisting of an interrogator, a bandage consisted of a textile-based rectifier, a textile VCO, and a textile-based antenna for data transfer. A remote receiver emulated by a spectrum analyzer is used to capture the wound data. We emulate electrochemical sensor's DC signal output through a resistive load in the circuit.

6.2.6 Battery-free, VCO-Based Frequency Modulations

Fig. **??** shows the blocks of the system that operate as follows: (1) the power transmitter module (e.g. integrated in a bed-sheet) consists of a transmitting antenna to provide RF power to a similar receiving antenna located in the bandage, using

frequencies between 350 MHz and 573 MHz. (2) The bandage features a textile-substrate rectifier to convert the RF power into DC to power an electrochemical sensor and a voltage-controlled oscillator (VCO). (3) A tri-electrode sensor with typical power usage of 24 μW, which senses uric acid (emulating chronic wound fluid) concentration to provide a DC current as a function of the concentration. (4) The VCO converts the DC signal into an RF signal, providing a simple data-modulation for transmittance through a second textile-based data-antenna (operating at 915 MHz). The modulated output signal, based on its frequency, will provide the uric acid concentration extracted from the wound fluid. Based on the value of the concentration, the wound-health status can be assessed [about the severity or restoration of damaged tissue] by obtaining a unique frequency from the remote receiver.

6.2.7 Wireless Power Telemetry Link

1. **Near Field Power Transfer using Corrugated Crossed-Dipole Antenna**

   The system in Fig. 6.9 illustrates a bedridden patient with a bandage on their left leg. The bandage circuit is powered through a transmitter antenna integrated in the bed. The proposed antennas were designed and fabricated using conductive fiber embroidery [113]. The shape of the antenna (see Fig. 6.9, inset), a corrugated crossed-dipole, is based on prior-proposed misalignment resilient anchor shaped antennas [112]. Misalignment resilience helps patients who may be subject to intermittent movements, which could interrupt the effective transfer of power from the bed to the bandage. The topology is based on prior works [112], and features corrugations known for modifying the EM

fields of antenna apertures and enable axial symmetry [140]. It is anticipated that the performance of the system will be stable on an average under lateral, diagonal, and angular misalignments. As can be seen in Fig. 6.10, the peak power transfer efficiency (PTE) is 80%, when the misalignment is introduced along the direction of stronger electric fields and 60% along the direction of stronger magnetic fields. It can inferred that the PTE is approximately con-
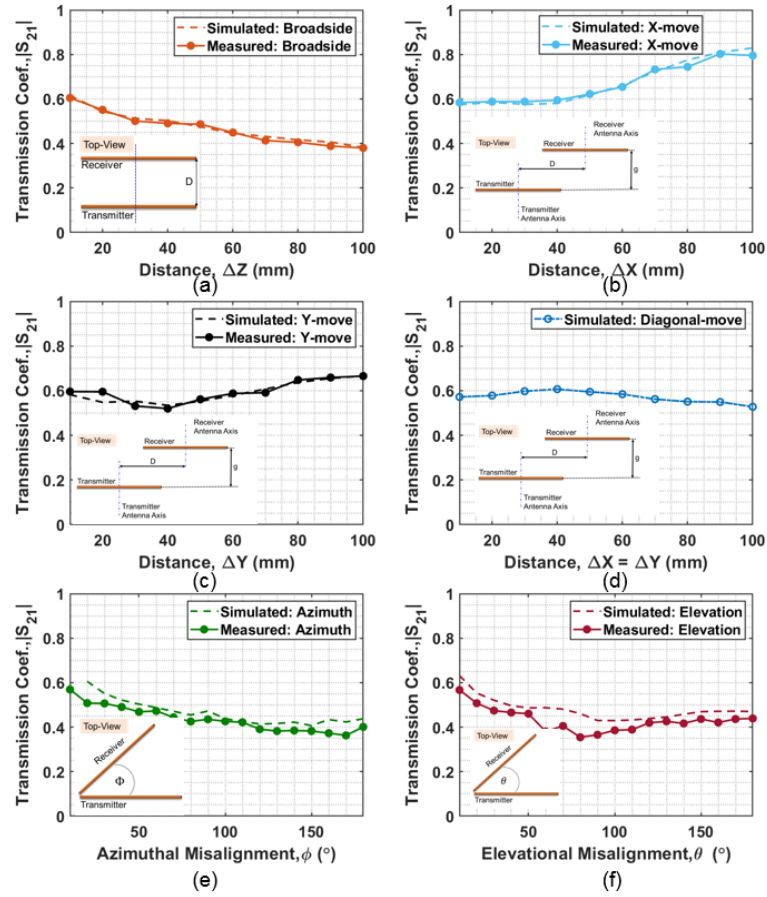
Figure 6.10: Effects of lateral and angular misalignments on the transmission capability of the antenna: (a) broadside direction when D varies from 1 to 10 cm, (b) and (c) lateral misalignments where $g = 1$ cm and DX,DY varies from 1 to 10 cm, (d) diagonal misalignment when where $g = 1$ cm and $DX=DY$ varies from 1 to 10 cm, (e) elevational misalignment, and (f) azimuthal misalignment.

stant under all misalignments. This is an indication that the system will be continuously powered regardless of the movement of the bearer.

2. **Textile-Based Rectifier**

Fig. 6.11 shows the rectifier featured in the proposed smart bandage. This
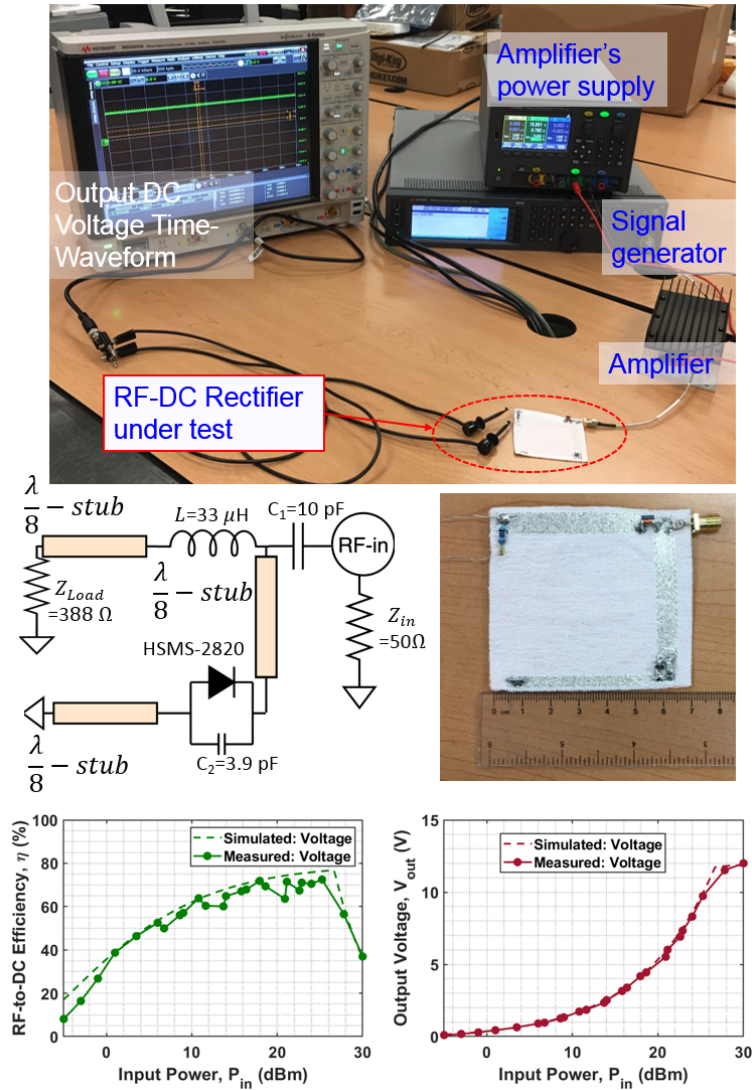
Figure 6.11: Textile-based rectifier: (Top) measurement setup for the rectifying circuit, (Middle-left) circuit diagram of the rectifier with all the lumped components,(Middle-right) finished prototype of textile rectifier, (Bottom-left) simulation and measurement results of RF-to-DC conversion efficiency, and (Bottom-right) simulated and measured collected DC voltage

single-diode rectifying circuit is a modified version of the first textile-based single-diode rectifier using a $\lambda/8$-shorted stub [113]. This circuit uses an extra $\lambda/8$-stub before the diode to compensate for the capacitive effect introduced by the diode. The impedance of the circuit is

$$Z_{circuit} = \frac{R_e}{1 + (R_e C_{total} \omega)^2} - j \frac{R_e^2 C_{total} \omega}{1 + (R_e C_{total} \omega)^2}, \tag{6.5}$$

where $C_{total} = C_e + C_2$, C_e is the capacitance of the diode and C_2 the capacitance of the small capacitor added in parallel with the diode. The imaginary part of the equation (6.5) shows that the rectifier is primarily capacitive. For high-efficiency achievement, the capacitive part of the impedance should be suppressed by conjugate matching.

The goal here is to eliminate the presence of the imaginary part of $Z_{circuit}$ and minimize the real part as much as possible. The conjugate matching is achieved by equating the magnitude of the impedance of the $\lambda/8$-stub to the $\Im(Z_{circuit})$. The rectifier was designed to operate at around 500 MHz and the lumped components used can be seen in Fig. 6.11 (Middle-left). A full-wave simulation was realized to estimate the RF-to-DC conversion efficiency as well as the collected DC voltage using ADS. The circuit was later fabricated using
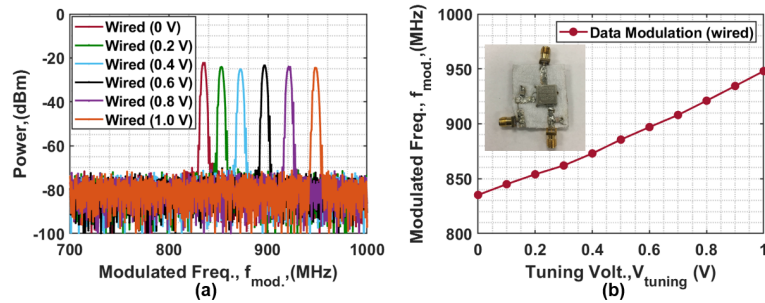
Figure 6.12: Textile VCO's (a) output spectra emulating the modulated data, and (b) obtained calibration curve showing frequency as a function of tuning voltage, which emulates the sensor output.

automated embroidery of Elektrisola-7 onto gauze fabric and tested. It was found that the textile rectifier exhibited an RF-to-DC conversion efficiency of 76% at 26 dBm input and the DC voltage collected at that power level was 10 V (see Fig. 6.11). This efficiency level is comparable or better than the current state of the art reported in [113].

3. **Textile-Based Voltage-Controlled Oscillator** The voltage-controlled oscillator is responsible for the modulation of the wound data detected by the electrochemical sensor. The characterization of the VCO circuit is shown in Fig. 6.12. A textile-integrated VCO, Crystek CVCO055BE, was achieved using embroidered Elektrisola-7 thread on a gauze-fabric as can be seen in Fig. 6.12 (b, inset). The tuning voltage was chosen to be between 0 and 1 V to test the VCO performance on a fabric substrate, and emulating the anticipated sensor output voltage. The modulated frequency was captured by a Keysight PXA signal analyzer N9030B [emulating a remote receiver] found to be between 836 MHz and 950 MHz.

6.2.8 Measurement Setup Realized to Emulate "IN-VIVO" Electrochemical Sensing and Monitoring Scenarios

To emulate real-life ["in-vivo"] settings, we assembled a measurement system [apparatus] that comprised of all the subsystems mentioned above. The apparatus included a smart bed (see Fig. 6.13), the smart sensing system (see Fig. 6.14), and a point-of-collection of wound data provided by the modulated small RF signal given by the textile-based VCO. The RF signal is received by an omnidirectional antenna (see Fig. 6.15). The resulted measurement setup can be see in Fig. 6.16. The smart bed is illuminated by a RF signal generator and power amplifier. The
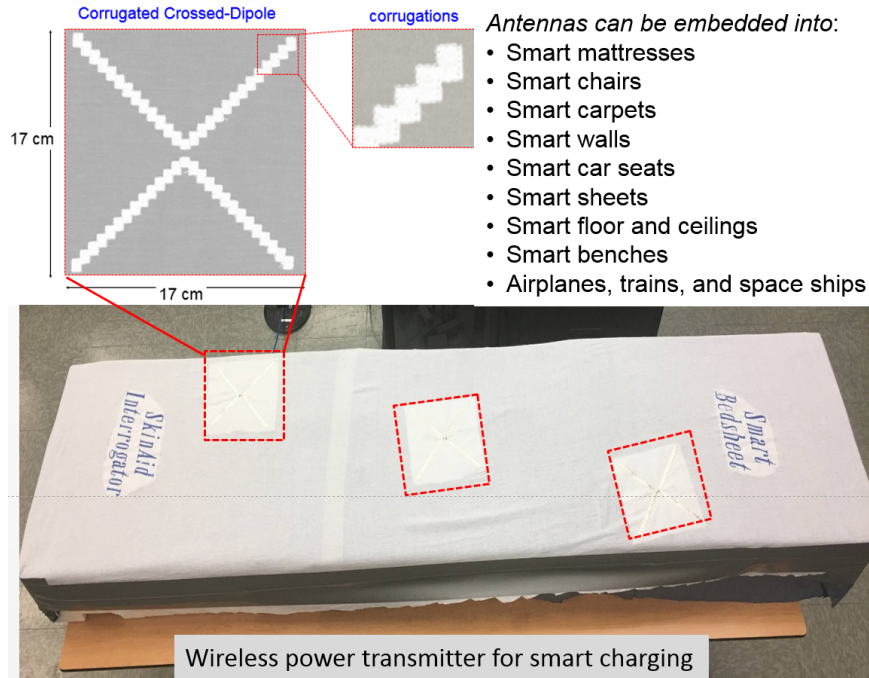
Figure 6.13: Wireless transmitting RF module to illuminate any receiving system for smart charging, monitoring, and sensing platform

RF signal transmitted by the smart bed is captured by the smart dressing solution [smart bandage] that converted it into DC to power the sensor and bias the VCO. The sensor, upon dipping in the would fluid [here emulated by placing a resistor at the sensor location] will sens the concentration of uric acid present in the wound fluid and sens the resulted DC signal to the VCO. The VCO modulates the DC signal and the obtained RF signal is sent to the 915-MHz dipole to re-transmit it wirelessly to the remote receiver [spectrum analyzer]. Upon reception of the modulated RF signal, the frequency is used for assessment. Using equation (6.2.4) we can determine the corresponding uric acid level that was detected by the sensor. The uric acid level that is resulted for applying the assessment equation (Equation 6.2.4) will be compared with the threshold, which is 0.4 mM.

The system was tested (see Fig. 6.16), where the transmitter was the bed separated from the bandage receiver by 6 in. (see Fig. 6.9) and the wound fluid was emulated
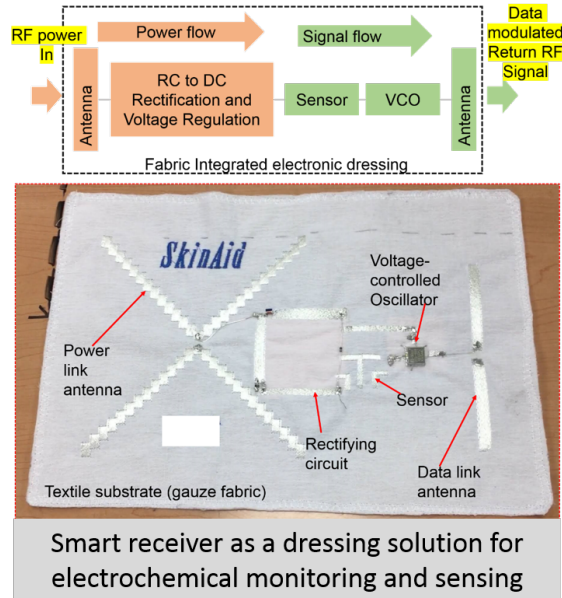
Figure 6.14: Resulted spectrum captured by a remote receiver (in this case a Keysight spectrum analyzer) representing the wound-data info sent more than 3 ft. away by the textile-antenna from the smart bandage.

by a resistive load. As can be seen in Fig. 6.14, the output signal sent by the sensor had a voltage level of 0.1 V and the corresponding frequency-modulation was at 845 MHz. This frequency can be visualized from the Fig. 6.16 (inset:wound data). This signal was captured at a distance of more than 3 ft. away from the bandage. The corresponding concentration of the wound fluid is 0 mM < 0.4 mM. This result suggests that the wound is healed.

6.3   Conclusion

In this chapter, we proposed smart bandages that are textile integrated, self-powered, and provide new methods to modulate the electrochemical sensor data for transmission. This was presented through two generations of the smart bandages. Direct frequency modulation is achieved using a VCO-based DC to RF modulation. The
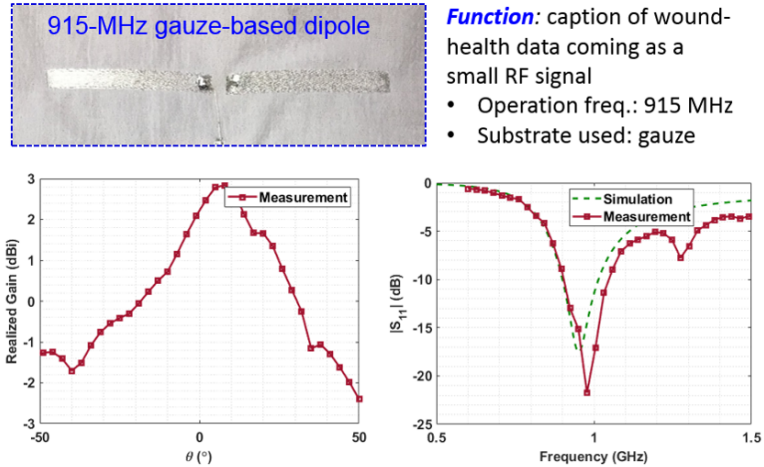
Figure 6.15: Re-transmitting antenna placed at the input-port of the signal analyzer to capture the small RF signal resulted from the modulation of the wound-health data
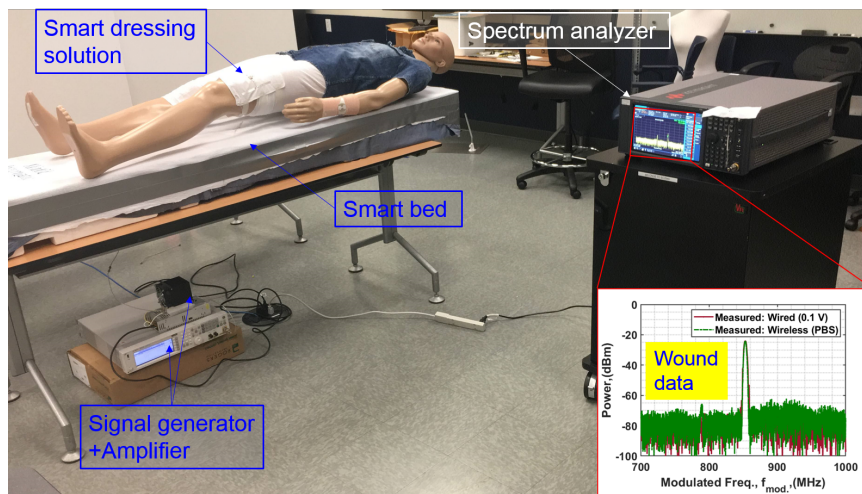
Figure 6.16: Experimental setup consisting of all elements of power transfer, smart sensing, and data transmittance to achieve reliable electrochemical assessment of chronic wounds. This apparatus can be used as a reference to real-life "in-vivo" scenarios

bandages feature a textile-based rectifier and VCO along with misalignment-resilient textile-based antenna (anchor and corrugated crossed-dipole) for power telemetry and dipole antenna for wound-data communication link. In sum, wireless powering, wireless data-extraction using frequency modulation was established with excellent

agreement with theoretical expectations of the rectifier and VCO. To the authors' knowledge, this is the first time a wirelessly powered battery-less smart bandage system, with power telemetry and wireless link, has been demonstrated with frequency modulation. The proposed system could effect the personalized, connected care by comfortable wearability and long-term usage. It is demonstrated that robust and reliable assessment of chronic wounds can be done using reduced electronic and textile-based voltage-controlled oscillator. The results can be used as a reference experiment for "in-vivo electrochemical monitoring" of chronic wounds.

CHAPTER 7

CONCLUSION AND FUTURE WORK

This chapter concludes the work proposed in this dissertation. The work started with a brief introduction to the problem, the goals, and methodology (Chapter 1). That was followed by a background and literature research. This part of the work was a general introduction about the works that have been published in each section, their limitations, and our contribution (Chapter 2). In the third chapter (Chapter 3) the RF characterization of the conductive textiles used to develop our textile-integrated systems was presented and discussed. In the following chapter (Chapter 4), a far-field system was designed, developed ,and tested using textile-integrated rectenna array for boosted Wi-Fi signals. A near-field power transfer and harvesting system that used anchor-shaped antennas was used into clothing items for wireless charging (Chapter 5). Finally, a smart bandage that uses wireless power transfer and harvesting on textiles to remotely monitor the healing process of chronic wounds (Chapter 6). This work is wrapped-up with some major takeaways found in Section 7.1 and some recommendations in Section 7.2.

7.1   Conclusion

We demonstrate the best design guidelines for our fabric-integrated systems is having the conductive textiles (Elektrisola-7) embroidered in the direction of the RF current (90°-fill stitch). This design guideline also suggested the resilience of the fabricated structures to mechanical deformations like bending and twisting. Textile-based antennas and harvesting circuits were developed at 360 MHz and 2.45 GHz exhibiting up to 70% at an 8-dBm and 77% at 22 dBm input power. Their integration into items of clothing was realized and DC power of up to 10 mW was collected, which

suggests their suitability to illuminate a wide range of sensors and IoT devices. We finally developed a smart bandage to continuously monitor chronic wounds using the frequency modulation from the detection of uric acid present in the wound bed. The smart bandage used the "transmit-reflect" principle to assess the healing status of the chronic wound using the data modulation from the low-power electrochemical sensing of wound fluid. The assessment was realized using the 0.4-mM threshold reported to be related to the severity and restoration of the wounded tissue. A theoretical model was demonstrated for trustworthy outcomes related to assessing the wound's healing status. In addition, a more realistic setup that mimics an "in-vivo/real-life" electrochemical monitoring setting for chronic wounds.

7.2 Future Works

A more sophisticated smart bandage can be used not only to assess the healing process of the wound, but also for its treatment. It can be also used to remotely send the wound data to any medical personal for assessment. The interrogator can be incorporated into a hospital bed, a wall, a floor, or ceiling to power continuously power the bandage.

BIBLIOGRAPHY

[1] H.-S. Zhang, S.-L. Chai, K. Xiao, and L. F. Ye, "Numerical and experimental analysis of wideband e-shape patch textile antenna," *Progress in Electromagnetics Research*, vol. 45, pp. 163–178, 2013.

[2] L. Song, A. C. Myers, J. J. Adams, and Y. Zhu, "Stretchable and reversibly deformable radio frequency antennas based on silver nanowires," *ACS applied materials & interfaces*, vol. 6, no. 6, pp. 4248–4253, 2014.

[3] S. Cheng, Z. Wu, P. Hallbjorner, K. Hjort, and A. Rydberg, "Foldable and stretchable liquid metal planar inverted cone antenna," *IEEE Transactions on antennas and propagation*, vol. 57, no. 12, pp. 3765–3771, 2009.

[4] B. S. Cook and A. Shamim, "Inkjet printing of novel wideband and high gain antennas on low-cost paper substrate," *IEEE Transactions on Antennas and Propagation*, vol. 60, no. 9, pp. 4148–4156, 2012.

[5] J. Zhong, A. Kiourti, T. Sebastian, Y. Bayram, and J. L. Volakis, "Conformal load-bearing spiral antenna on conductive textile threads," *IEEE Antennas and Wireless Propagation Letters*, vol. 16, pp. 230–233, 2016.

[6] Z. Wang, L. Zhang, Y. Bayram, and J. L. Volakis, "Embroidered conductive fibers on polymer composite for conformal antennas," *IEEE Transactions on Antennas and Propagation*, vol. 60, no. 9, pp. 4141–4147, 2012.

[7] A. Kiourti, C. Lee, and J. L. Volakis, "Fabrication of textile antennas and circuits with 0.1 mm precision," *IEEE Antennas and Wireless Propagation Letters*, vol. 15, pp. 151–153, 2015.

[8] J. Zhong, A. Kiourti, J. L. Volakis, T. Sebastian, and Y. Bayram, "Mechanical and thermal tests of textile antennas for load bearing applications," in *2016 IEEE International Symposium on Antennas and Propagation (APSURSI)*, pp. 1943–1944, IEEE, 2016.

[9] Z. Wang, L. Z. Lee, D. Psychoudakis, and J. L. Volakis, "Embroidered multi-band body-worn antenna for gsm/pcs/wlan communications," *IEEE Transactions on Antennas and Propagation*, vol. 62, no. 6, pp. 3321–3329, 2014.

[10] A. Salleo and W. S. Wong, *Flexible Electronics: Materials and Applications*. Springer, 2009.

[11] L. Roselli, N. B. Carvalho, F. Alimenti, P. Mezzanotte, G. Orecchini, M. Virili, C. Mariotti, R. Goncalves, and P. Pinho, "Smart surfaces: Large area electronics systems for internet of things enabled by energy harvesting," *Proceedings of the IEEE*, vol. 102, no. 11, pp. 1723–1746, 2014.

[12] W. R. Lambert, "Rf flex circuit transmission line and interconnection method," Aug. 18 1998. US Patent 5,795,162.

[13] U. Olgun, C.-C. Chen, and J. L. Volakis, "Design of an efficient ambient wifi energy harvesting system," *IET Microwaves, Antennas & Propagation*, vol. 6, no. 11, pp. 1200–1206, 2012.

[14] J. M. Gilbert and F. Balouchi, "Comparison of energy harvesting systems for wireless sensor networks," *International Journal of automation and computing*, vol. 5, no. 4, pp. 334–347, 2008.

[15] H. Wang and P. P. Mercier, "Near-zero-power temperature sensing via tunneling currents through complementary metal-oxide-semiconductor transistors," *Scientific Reports*, vol. 7, no. 1, p. 4427, 2017.

[16] F. Deng, Y. He, B. Li, L. Zhang, X. Wu, Z. Fu, and L. Zuo, "Design of an embedded CMOS temperature sensor for passive RFID tag chips," *Sensors*, vol. 15, no. 5, pp. 11442–11453, 2015.

[17] J. Lee and S. Cho, "A 1.4-μW 24.9-ppm/deg C Current Reference With Process-Insensitive Temperature Compensation in 0.18-μm CMOS," *IEEE Journal of Solid-State Circuits*, vol. 47, no. 10, pp. 2527–2533, 2012.

[18] K. Souri, Y. Chae, F. Thus, and K. Makinwa, "12.7 A 0.85 V 600nW all-CMOS temperature sensor with an inaccuracy of$\pm$0.4 C (3σ) from- 40 to 125 C," in *Solid-State Circuits Conference Digest of Technical Papers (ISSCC), 2014 IEEE International*, pp. 222–223, IEEE, 2014.

[19] M. K. Law and A. Bermak, "A 405-nW CMOS temperature sensor based on linear MOS operation," *IEEE Transactions on Circuits and Systems II: Express Briefs*, vol. 56, no. 12, pp. 891–895, 2009.

[20] Y. Ji, C. Jeon, H. Son, B. Kim, H.-J. Park, and J.-Y. Sim, "A 9.3 nW all-in-one bandgap voltage and current reference circuit using leakage-based PTAT generation and DIBL characteristic," in *Proceedings of the 23rd Asia and South Pacific Design Automation Conference*, pp. 309–310, IEEE Press, 2018.

[21] K. Ueno, T. Hirose, T. Asai, and Y. Amemiya, "A 300 nW, 15 ppm/° C, 20 ppm/V CMOS Voltage Reference Circuit Consisting of Subthreshold MOS-FETs," *IEEE Journal of solid-state circuits*, vol. 44, no. 7, pp. 2047–2054, 2009.

[22] J. Salvia, P. Lajevardi, M. Hekmat, and B. Murmann, "A 56MΩ CMOS TIA for MEMS applications," in *Custom Integrated Circuits Conference, 2009. CICC'09. IEEE*, pp. 199–202, IEEE, 2009.

[23] J. Hu, Y.-B. Kim, and J. Ayers, "A low power 100MΩ CMOS front-end transimpedance amplifier for biosensing applications," in *Circuits and Systems (MWSCAS), 2010 53rd IEEE International Midwest Symposium on*, pp. 541–544, IEEE, 2010.

[24] B. DeLong, C. Chen, and J. Volakis, "Wireless energy harvesting for medical applications," in *Antennas and Propagation & USNC/URSI National Radio Science Meeting, 2015 IEEE International Symposium on*, pp. 1213–1213, IEEE, 2015.

[25] J. Zhong, A. Kiourti, T. Sebastian, Y. Bayram, and J. L. Volakis, "Conformal load-bearing spiral antenna on conductive textile threads," *IEEE Antennas and Wireless Propagation Letters*, vol. 16, pp. 230–233, 2017.

[26] D. Vital, S. Bhardwaj, and J. L. Volakis, "Bending and twisting for RF performances of textile transmission lines," in *2018 IEEE Antennas and Propagation Society International Symposium (APSURSI)*, July 2019.

[27] B. DeLong, Q. Yuan, and J. L. Volakis, "Long range, safe power transmission using iteratively-tuned rectification," in *2015 International Symposium on Antennas and Propagation (ISAP)*, pp. 1–2, Nov 2015.

[28] A. Kiourti, C. Lee, and J. L. Volakis, "Fabrication of textile antennas and circuits with 0.1 mm precision," *IEEE Antennas and Wireless Propagation Letters*, vol. 15, pp. 151–153, 2015.

[29] H. Sun, Y.-x. Guo, M. He, and Z. Zhong, "Design of a high-efficiency 2.45-ghz rectenna for low-input-power energy harvesting," *IEEE Antennas and Wireless Propagation Letters*, vol. 11, pp. 929–932, 2012.

[30] H. Sun, Y.-x. Guo, M. He, and Z. Zhong, "A dual-band rectenna using broadband yagi antenna array for ambient rf power harvesting," *IEEE Antennas and Wireless Propagation Letters*, vol. 12, pp. 918–921, 2013.

[31] S. Shen, C.-Y. Chiu, and R. D. Murch, "Multiport pixel rectenna for ambient rf energy harvesting," *IEEE Transactions on Antennas and Propagation*, vol. 66, no. 2, pp. 644–656, 2017.

[32] A. M. Jawad, R. Nordin, S. K. Gharghan, H. M. Jawad, and M. Ismail, "Opportunities and challenges for near-field wireless power transfer: A review," *energies*, vol. 10, no. 7, p. 1022, 2017.

[33] R. Shadid and S. Noghanian, "A literature survey on wireless power transfer for biomedical devices," *International Journal of Antennas and Propagation*, vol. 2018, 2018.

[34] S. Smith, T. Tang, J. Terry, J. Stevenson, B. Flynn, H. Reekie, A. Murray, A. Gundlach, D. Renshaw, B. Dhillon, *et al.*, "Development of a miniaturised drug delivery system with wireless power transfer and communication," *IET nanobiotechnology*, vol. 1, no. 5, pp. 80–86, 2007.

[35] F.-G. Zeng, S. Rebscher, W. Harrison, X. Sun, and H. Feng, "Cochlear implants: system design, integration, and evaluation," *IEEE reviews in biomedical engineering*, vol. 1, pp. 115–142, 2008.

[36] C. Sauer, M. Stanacevic, G. Cauwenberghs, and N. Thakor, "Power harvesting and telemetry in cmos for implanted devices," *IEEE Transactions on Circuits and Systems I: Regular Papers*, vol. 52, no. 12, pp. 2605–2613, 2005.

[37] A. Kurs, A. Karalis, R. Moffatt, J. D. Joannopoulos, P. Fisher, and M. Soljačić, "Wireless power transfer via strongly coupled magnetic resonances," *science*, vol. 317, no. 5834, pp. 83–86, 2007.

[38] K. Fotopoulou and B. W. Flynn, "Wireless power transfer in loosely coupled links: Coil misalignment model," *IEEE Transactions on Magnetics*, vol. 47, no. 2, pp. 416–430, 2010.

[39] G. Vandevoorde and R. Puers, "Wireless energy transfer for stand-alone systems: a comparison between low and high power applicability," *Sensors and Actuators A: Physical*, vol. 92, no. 1-3, pp. 305–311, 2001.

[40] S. J. Mazlouman, A. Mahanfar, and B. Kaminska, "Mid-range wireless energy transfer using inductive resonance for wireless sensors," in *2009 IEEE International Conference on Computer Design*, pp. 517–522, IEEE, 2009.

[41] E. M. Thomas, J. D. Heebl, C. Pfeiffer, and A. Grbic, "A power link study of wireless non-radiative power transfer systems using resonant shielded loops," *IEEE Transactions on Circuits and Systems I: Regular Papers*, vol. 59, pp. 2125–2136, Sep. 2012.

[42] A. Kurs, A. Karalis, R. Moffatt, J. D. Joannopoulos, P. Fisher, and M. Soljačić, "Wireless Power Transfer via Strongly Coupled Magnetic Resonances," *Science*, vol. 317, no. 5834, pp. 83–86, 2007.

[43] A. Costanzo, M. Dionigi, D. Masotti, M. Mongiardo, G. Monti, L. Tarricone, and R. Sorrentino, "Electromagnetic energy harvesting and wireless power transmission: A unified approach," *Proceedings of the IEEE*, vol. 102, pp. 1692–1711, Nov 2014.

[44] D. Zhu, L. Clare, B. H. Stark, and S. P. Beeby, "Near field wireless power transfer using curved relay resonators for extended transfer distance," *Journal of Physics: Conference Series*, vol. 660, p. 12136, dec 2015.

[45] D. Liu, H. Hu, and S. V. Georgakopoulos, "Misalignment sensitivity of strongly coupled wireless power transfer systems," *IEEE Transactions on Power Electronics*, vol. 32, no. 7, pp. 5509–5519, 2016.

[46] D. Liu and S. V. Georgakopoulos, "Cylindrical misalignment insensitive wireless power transfer systems," *IEEE Transactions on Power Electronics*, vol. 33, no. 11, pp. 9331–9343, 2018.

[47] A. A. Eteng, S. K. A. Rahim, and C. Y. Leow, "Wireless Nonradiative Energy Transfer: Antenna performance enhancement techniques.," *IEEE Antennas and Propagation Magazine*, vol. 57, pp. 16–22, jun 2015.

[48] H. Younesiraad and M. Bemani, "Analysis of coupling between magnetic dipoles enhanced by metasurfaces for wireless power transfer efficiency improvement," *Scientific Reports*, vol. 8, dec 2018.

[49] H. Cheng and H. Zhang, "Investigation of Improved Methods in Power Transfer Efficiency for Radiating Near-Field Wireless Power Transfer," *Journal of Electrical and Computer Engineering*, vol. 2016, 2016.

[50] S. Aldhaher, P. C.-K. Luk, and J. F. Whidborne, "Electronic tuning of misaligned coils in wireless power transfer systems," *IEEE Transactions on Power Electronics*, vol. 29, no. 11, pp. 5975–5982, 2014.

[51] J. Choi, J. Xu, R. Makhoul, and J. M. R. Davila, "Implementing an impedance compression network to compensate for misalignments in a wireless power transfer system," *IEEE Transactions on Power Electronics*, vol. 34, no. 5, pp. 4173–4184, 2018.

[52] S. Lee, H. Hoang, Y. Choi, and F. Bien, "Efficiency improvement for magnetic resonance based wireless power transfer with axial-misalignment," *Electronics letters*, vol. 48, no. 6, pp. 339–340, 2012.

[53] Z. Zhang and B. Zhang, "Angular-misalignment insensitive omnidirectional wireless power transfer," *IEEE Transactions on Industrial Electronics*, vol. 67, no. 4, pp. 2755–2764, 2019.

[54] J.-S. Hong and M. J. Lancaster, "Couplings of microstrip square open-loop resonators for cross-coupled planar microwave filters," *IEEE Transactions on Microwave theory and Techniques*, vol. 44, no. 11, pp. 2099–2109, 1996.

[55] Chwei-Sen Wang, G. A. Covic, and O. H. Stielau, "Power transfer capability and bifurcation phenomena of loosely coupled inductive power transfer systems," *IEEE Transactions on Industrial Electronics*, vol. 51, pp. 148–157, Feb 2004.

[56] D. Liu and S. V. Georgakopoulos, "Cylindrical misalignment insensitive wireless power transfer systems," *IEEE Transactions on Power Electronics*, vol. 33, no. 11, pp. 9331–9343, 2018.

[57] G. Vandevoorde and R. Puers, "Wireless energy transfer for stand-alone systems: a comparison between low and high power applicability," *Sensors and Actuators A: Physical*, vol. 92, no. 1-3, pp. 305–311, 2001.

[58] S. J. Mazlouman, A. Mahanfar, and B. Kaminska, "Mid-range wireless energy transfer using inductive resonance for wireless sensors," in *2009 IEEE International Conference on Computer Design*, pp. 517–522, IEEE, 2009.

[59] G. Vandevoorde and R. Puers, "Wireless energy transfer for stand-alone systems: a comparison between low and high power applicability," *Sensors and Actuators A: Physical*, vol. 92, no. 1-3, pp. 305–311, 2001.

[60] A. Kurs, A. Karalis, R. Moffatt, J. D. Joannopoulos, P. Fisher, and M. Soljačić, "Wireless power transfer via strongly coupled magnetic resonances," *science*, vol. 317, no. 5834, pp. 83–86, 2007.

[61] H. Hu, K. Bao, J. Gibson, and S. V. Georgakopoulos, "Printable and conformal strongly coupled magnetic resonant systems for wireless powering," in *WAMICON 2014*, pp. 1–4, IEEE, 2014.

[62] D. Liu, H. Hu, and S. V. Georgakopoulos, "Misalignment sensitivity of strongly coupled wireless power transfer systems," *IEEE Transactions on Power Electronics*, vol. 32, no. 7, pp. 5509–5519, 2016.

[63] K. Fotopoulou and B. W. Flynn, "Wireless power transfer in loosely coupled links: Coil misalignment model," *IEEE Transactions on Magnetics*, vol. 47, no. 2, pp. 416–430, 2010.

[64] C. M. Zierhofer and E. S. Hochmair, "Geometric approach for coupling enhancement of magnetically coupled coils," *IEEE transactions on Biomedical Engineering*, vol. 43, no. 7, pp. 708–714, 1996.

[65] D. Vital and S. Bhardwaj, "Misalignment resilient anchor-shaped antennas in near-field wireless power transfer using electric and magnetic coupling modes (*Minor Revisions*)," *IEEE Transactions on Antennas and Propagation*, vol. 1, no. 1, pp. 1–1, 2020.

[66] D. Sharman, "Chronic gout in the diabetic foot," *The Diabetic Foot Journal*, vol. 17, no. 1, 2014. Date Accessed 2019-11-23.

[67] S. R. Nussbaum, M. J. Carter, C. E. Fife, J. DaVanzo, R. Haught, M. Nusgart, and D. Cartwright, "An economic evaluation of the impact, cost, and medicare policy implications of chronic nonhealing wounds," *Value in Health*, vol. 21, no. 1, pp. 27–32, 2018.

[68] P. Kassal, J. Kim, R. Kumar, W. R. de Araujo, I. M. Steinberg, M. D. Steinberg, and J. Wang, "Smart bandage with wireless connectivity for uric acid biosensing as an indicator of wound status," *Electrochemistry Communications*, vol. 56, pp. 6–10, 2015.

[69] M. L. Fernandez, Z. Upton, and G. K. Shooter, "Uric acid and xanthine oxidoreductase in wound healing," *Current rheumatology reports*, vol. 16, no. 2, p. 396, 2014.

[70] M. L. Fernandez, Z. Upton, H. Edwards, K. Finlayson, and G. K. Shooter, "Elevated uric acid correlates with wound severity," *International wound journal*, vol. 9, no. 2, pp. 139–149, 2012.

[71] Y. Umasankar, M. Mujawar, and S. Bhansali, "Towards biosensor enabled smart bandages for wound monitoring: Approach and overview," in *2018 IEEE SENSORS*, pp. 1–4, IEEE, 2018.

[72] M. G. Filanovsky, K. Sukhdeo, and M. C. McNamara, "Ulcerated tophaceous gout," *Case Reports*, vol. 2015, p. bcr2015210707, 2015.

[73] H. Derakhshandeh, S. S. Kashaf, F. Aghabaglou, I. O. Ghanavati, and A. Tamayol, "Smart bandages: the future of wound care," *Trends in biotechnology*, vol. 36, no. 12, pp. 1259–1274, 2018.

[74] D. Vital, S. Bhardwaj, and J. L. Volakis, "Bending and twisting tests for rf performances of textile transmission lines," in *2019 IEEE International Symposium on Antennas and Propagation and USNC-URSI Radio Science Meeting*, pp. 2173–2174, IEEE, 2019.

[75] www.creativematerials.com, "127-48 screen-printable electrically conductive ink."

[76] Z. Wang, L. Zhang, Y. Bayram, and J. L. Volakis, "Embroidered conductive fibers on polymer composite for conformal antennas," *IEEE Transactions on Antennas and Propagation*, vol. 60, no. 9, pp. 4141–4147, 2012.

[77] D. Vital, J. Zhong, S. Bhardwaj, and J. L. Volakis, "Loss-characterization and guidelines for embroidery of conductive textiles," in *2018 IEEE International Symposium on Antennas and Propagation & USNC/URSI National Radio Science Meeting*, pp. 1301–1302, IEEE, 2018.

[78] H.-S. Zhang, S.-L. Chai, K. Xiao, and L. F. Ye, "Numerical and experimental analysis of wideband E-shape patch textile antenna," *Progress in Electromagnetics Research*, vol. 45, pp. 163–178, 2013.

[79] R. Moro, S. Agneessens, H. Rogier, and M. Bozzi, "Wearable textile antenna in substrate integrated waveguide technology," *Electronics Letters*, vol. 48, pp. 985–987, August 2012.

[80] S. Lemey, F. Declercq, and H. Rogier, "Textile antennas as hybrid energy-harvesting platforms," *Proceedings of the IEEE*, vol. 102, no. 11, pp. 1833–1857, 2014.

[81] L. Song, A. C. Myers, J. J. Adams, and Y. Zhu, "Stretchable and reversibly deformable radio frequency antennas based on silver nanowires," *ACS applied materials & interfaces*, vol. 6, no. 6, pp. 4248–4253, 2014.

[82] B. S. Cook and A. Shamim, "Inkjet printing of novel wideband and high gain antennas on low-cost paper substrate," *IEEE Transactions on Antennas and Propagation*, vol. 60, no. 9, pp. 4148–4156, 2012.

[83] S. Cheng, Z. Wu, P. Hallbjorner, K. Hjort, and A. Rydberg, "Foldable and stretchable liquid metal planar inverted cone antenna," *IEEE Transactions on antennas and propagation*, vol. 57, no. 12, pp. 3765–3771, 2009.

[84] Z. Wang, L. Zhang, Y. Bay Ram, J. L. Volakis, *et al.*, "Embroidered conductive fibers on polymer composite for conformal antennas," *IEEE Transactions on Antennas and Propagation*, vol. 60, no. 9, p. 4141, 2012.

[85] J. Zhong, A. Kiourti, J. L. Volakis, T. Sebastian, and Y. Bayram, "Mechanical and thermal tests of textile antennas for load bearing applications," in *Antennas and Propagation (APSURSI), 2016 IEEE International Symposium on*, pp. 1943–1944, IEEE, 2016.

[86] L. Corchia, G. Monti, and L. Tarricone, "Wearable antennas: Nontextile versus fully textile solutions," *IEEE Antennas and Propagation Magazine*, 2019.

[87] S. Shawalil, K. N. Abdul Rani, and H. A. Rahim, "2.45 ghz wearable rectenna array design for microwave energy harvesting," *Indonesian Journal of Electrical Engineering and Computer Science*, vol. 14, pp. 677–687, 05 2019.

[88] D. Vital, J. L. Volakis, and S. Bhardwaj, "Loss-Characterization and Guidelines for Embroidery of Conductive Textiles," in *2018 IEEE Antennas and Propagation Society International Symposium (APSURSI)*, July 2018.

[89] A. Kiourti, C. Lee, and J. L. Volakis, "Fabrication of textile antennas and circuits with 0.1 mm precision," *IEEE Antennas and Wireless Propagation Letters*, vol. 15, pp. 151–153, 2016.

[90] C. A. Balanis, *Antenna Theory: Analysis and Design*. Hoboken, New Jersey: John Wiley and Sons, 4 ed., 2015.

[91] M. Vallejo, J. Recas, P. del Valle, and J. Ayala, "Accurate human tissue characterization for energy-efficient wireless on-body communications," *Sensors*, vol. 13, no. 6, pp. 7546–7569, 2013.

[92] "IEEE C95.1-2005 - IEEE Standard for Safety Levels with Respect to Human Exposure to Radio Frequency Electromagnetic Fields, 3 kHz to 300 GHz."

[93] C. R. Valenta and G. D. Durgin, "Harvesting Wireless Power: Survey of Energy-Harvester Conversion Efficiency in Far-Field, Wireless Power Transfer Systems," *IEEE Microwave Magazine*, vol. 15, pp. 108–120, June 2014.

[94] M. M. Mohamed, G. A. Fahmy, A. B. Abdel-Rahman, A. Allam, A. Barakat, M. Abo-Zahhad, H. Jia, and R. K. Pokharel, "High-Efficiency CMOS RF-to-DC Rectifier Based on Dynamic Threshold Reduction Technique for Wireless Charging Applications," *IEEE Access*, vol. 6, pp. 46826–46832, 2018.

[95] S. Hemour, Y. Zhao, C. H. P. Lorenz, D. Houssameddine, Y. Gui, C. Hu, and K. Wu, "Towards Low-Power High-Efficiency RF and Microwave Energy Harvesting," *IEEE Transactions on Microwave Theory and Techniques*, vol. 62, pp. 965–976, April 2014.

[96] T. Paing, E. Falkenstein, R. Zane, and Z. Popovic, "Custom IC for ultra-low power RF energy harvesting," in *2009 Twenty-Fourth Annual IEEE Applied Power Electronics Conference and Exposition*, pp. 1239–1245, IEEE, 2009.

[97] D. Masotti, A. Costanzo, M. D. Prete, and V. Rizzoli, "Genetic-based design of a tetra-band high-efficiency radio-frequency energy harvesting system," *IET Microwaves, Antennas Propagation*, vol. 7, pp. 1254–1263, December 2013.

[98] G. A. Vera, A. Georgiadis, A. Collado, and S. Via, "Design of a 2.45 GHz rectenna for electromagnetic (EM) energy scavenging," in *2010 IEEE Radio and Wireless Symposium (RWS)*, pp. 61–64, Jan 2010.

[99] U. Olgun, C. Chen, and J. L. Volakis, "Wireless power harvesting with planar rectennas for 2.45 GHz RFIDs," in *2010 URSI International Symposium on Electromagnetic Theory*, pp. 329–331, Aug 2010.

[100] J. F. Ensworth, S. J. Thomas, S. Y. Shin, and M. S. Reynolds, "Waveform-aware ambient RF energy harvesting," in *2014 IEEE International Conference on RFID (IEEE RFID)*, pp. 67–73, April 2014.

[101] B. DeLong, A. Kiourti, and J. L. Volakis, "A 2.4-GHz wireless sensor network using single diode rectennas," in *2016 IEEE International Symposium on Antennas and Propagation (APSURSI)*, pp. 403–404, June 2016.

[102] "FCC Rules and Regulations — AIR802 — 2.4 & 5 GHz Bands."

[103] B. J. DeLong, *Integration of Radio Frequency Harvesting with Low Power Sensors*. PhD thesis, The Ohio State University, 2018.

[104] V. Talla, B. Kellogg, B. Ransford, S. Naderiparizi, J. R. Smith, and S. Gollakota, "Powering the next Billion devices with Wi-Fi," *Commun. ACM*, vol. 60, pp. 83–91, 2015.

[105] S.-E. Adami, P. Proynov, G. S. Hilton, G. Yang, C. Zhang, D. Zhu, Y. Li, S. P. Beeby, I. J. Craddock, and B. H. Stark, "A flexible 2.45-ghz power harvesting wristband with net system output from- 24.3 dbm of rf power," *IEEE Transactions on Microwave Theory and Techniques*, vol. 66, no. 1, pp. 380–395, 2017.

[106] J. S. Besnoff, T. Deyle, R. R. Harrison, and M. S. Reynolds, "Battery-free multichannel digital ecg biotelemetry using uhf rfid techniques," in *2013 IEEE International Conference on RFID (RFID)*, pp. 16–22, IEEE, 2013.

[107] R. M. El Khosht, M. A. El Feshawy, M. A. El Shorbagy, M. N. Farag, A. E. El Said, H. F. Hammad, and A. T. Abdel-Hamid, "A foldable textile-based broadband archimedean spiral rectenna for rf energy harvesting," in *2016 16th Mediterranean Microwave Symposium (MMS)*, pp. 1–4, IEEE, 2016.

[108] B. Naresh, V. K. Singh, V. Bhargavi, A. Garg, and A. K. Bhoi, "Dual-band wearable rectenna for low-power rf energy harvesting," in *Advances in Power Systems and Energy Management*, pp. 13–21, Springer, 2018.

[109] A. Costanzo, D. Masotti, and M. Del Prete, "Wireless power supplying flexible and wearable systems," in *2013 7th European Conference on Antennas and Propagation (EuCAP)*, pp. 2843–2846, IEEE, 2013.

[110] D. Masotti, A. Costanzo, and S. Adami, "Design and realization of a wearable multi-frequency rf energy harvesting system," in *Proceedings of the 5th European Conference on Antennas and Propagation (EUCAP)*, pp. 517–520, IEEE, 2011.

[111] M. Dini, M. Filippi, A. Costanzo, A. Romani, M. Tartagni, M. Del Prete, and D. Masotti, "A fully-autonomous integrated rf energy harvesting system for wearable applications," in *2013 European Microwave Conference*, pp. 987–990, IEEE, 2013.

[112] D. Vital and S. Bhardwaj, "Misalignment resilient anchor-shaped antennas in near-field wireless power transfer using electric and magnetic coupling modes," *IEEE Transactions on Antennas and Propagation*, 2020.

[113] D. Vital, P. Gaire, S. Bhardwaj, and J. L. Volakis, "An ergonomic wireless charging system for integration with daily life activities," *IEEE Transactions on Microwave Theory and Techniques*, 2020.

[114] N. Owen, P. B. Sparling, G. N. Healy, D. W. Dunstan, and C. E. Matthews, "Sedentary behavior: emerging evidence for a new health risk," in *Mayo Clinic Proceedings*, vol. 85, pp. 1138–1141, Elsevier, 2010.

[115] P. Jin and R. W. Ziolkowski, "Low-q, electrically small, efficient near-field resonant parasitic antennas," *IEEE Transactions on Antennas and Propagation*, vol. 57, no. 9, pp. 2548–2563, 2009.

[116] S. Y. R. Hui, W. Zhong, and C. K. Lee, "A critical review of recent progress in mid-range wireless power transfer," *IEEE Transactions on Power Electronics*, vol. 29, no. 9, pp. 4500–4511, 2013.

[117] O. Jonah, S. V. Georgakopoulos, and M. M. Tentzeris, "Optimal design parameters for wireless power transfer by resonance magnetic," *IEEE Antennas and Wireless Propagation Letters*, vol. 11, pp. 1390–1393, 2012.

[118] Y. Chow, K. Wan, T. Sarkar, and B. Kolundzija, "Microstrip line on ground plane with closely spaced perforations—fringe fields and formulas by synthetic asymptote," *Microwave and Optical Technology Letters*, vol. 32, no. 3, pp. 201–204, 2002.

[119] M. Hamid and R. Hamid, "Equivalent circuit of dipole antenna of arbitrary length," *IEEE transactions on Antennas and Propagation*, vol. 45, no. 11, pp. 1695–1696, 1997.

[120] S. Raju, R. Wu, M. Chan, and C. P. Yue, "Modeling of mutual coupling between planar inductors in wireless power applications," *IEEE Transactions on Power Electronics*, vol. 29, no. 1, pp. 481–490, 2013.

[121] H. W. Ott, *Electromagnetic Compatibility Engineering*. John Wiley and Sons, Inc., 2009.

[122] D. Vital, S. Bhardwaj, and J. L. Volakis, "Textile based large area rf-power harvesting system for wearable applications," *IEEE Transactions on Antennas and Propagation*, 2019.

[123] ICNIRP, "Icnirp guidelines for limiting exposure to electromagnetic fields (100khz to 300 ghz)," *Health Phys 118(5):483-524;2020*, vol. 118, no. 5, pp. 483–524, 2020-*Accessed: 09-08-2020*.

[124] P. Wu, S. Y. Huang, W. Zhou, Z. H. Ren, Z. Liu, K. Huang, and C. Liu, "High-efficient rectifier with extended input power range based on self-tuning impedance matching," *IEEE Microwave and Wireless Components Letters*, vol. 28, no. 12, pp. 1116–1118, 2018.

[125] K. Finkenzeller, *RFID Handbook: Radio-frequency identification fundamentals and applications*. Wiley, 1999.

[126] D. Vital, J. L. Volakis, and S. Bhardwaj, "A wireless power transfer system (wpts) using misalignment resilient, on-fabric resonators for wearable applications," in *2020 IEEE MTT-S International Microwave Symposium (IMS)*, pp. 1–1, IEEE, 2020.

[127] J. F. Dickson, "On-chip high-voltage generation in mnos integrated circuits using an improved voltage multiplier technique," *IEEE Journal of solid-state circuits*, vol. 11, no. 3, pp. 374–378, 1976.

[128] E. Spanò, S. Di Pascoli, and G. Iannaccone, "Low-power wearable ecg monitoring system for multiple-patient remote monitoring," *IEEE Sensors Journal*, vol. 16, no. 13, pp. 5452–5462, 2016.

[129] M. Tavakoli, L. Turicchia, and R. Sarpeshkar, "An ultra-low-power pulse oximeter implemented with an energy-efficient transimpedance amplifier," *IEEE transactions on biomedical circuits and systems*, vol. 4, no. 1, pp. 27–38, 2009.

[130] R. R. Harrison, R. J. Kier, C. A. Chestek, V. Gilja, P. Nuyujukian, S. Ryu, B. Greger, F. Solzbacher, and K. V. Shenoy, "Wireless neural recording with single low-power integrated circuit," *IEEE transactions on neural systems and rehabilitation engineering*, vol. 17, no. 4, pp. 322–329, 2009.

[131] P. Kassal, J. Kim, R. Kumar, W. R. de Araujo, I. M. Steinberg, M. D. Steinberg, and J. Wang, "Smart bandage with wireless connectivity for uric acid

biosensing as an indicator of wound status," *Electrochemistry Communications*, vol. 56, pp. 6–10, 2015.

[132] D. Sharman, "Chronic gout in the diabetic foot," *The Diabetic Foot Journal*, vol. 17, no. 1, 2014. Date Accessed 2019-11-23.

[133] K. Oakes, "Heart disease remains the leading cause of death in the us," *Clinicians Review*, 2018.

[134] A. Pal, D. Goswami, H. E. Cuellar, B. Castro, S. Kuang, and R. V. Martinez, "Early detection and monitoring of chronic wounds using low-cost, omniphobic paper-based smart bandages," *Biosensors and Bioelectronics*, vol. 117, pp. 696–705, 2018.

[135] H. Derakhshandeh, S. S. Kashaf, F. Aghabaglou, I. O. Ghanavati, and A. Tamayol, "Smart bandages: the future of wound care," *Trends in biotechnology*, vol. 36, no. 12, pp. 1259–1274, 2018.

[136] P. Kassal, J. Kim, R. Kumar, W. R. de Araujo, I. M. Steinberg, M. D. Steinberg, and J. Wang, "Smart bandage with wireless connectivity for uric acid biosensing as an indicator of wound status," *Electrochemistry Communications*, vol. 56, pp. 6–10, 2015.

[137] P. Kassal, J. Kim, R. Kumar, W. R. de Araujo, I. M. Steinberg, M. D. Steinberg, and J. Wang, "Smart bandage with wireless connectivity for uric acid biosensing as an indicator of wound status," *Electrochemistry Communications*, vol. 56, pp. 6–10, 2015.

[138] H. Derakhshandeh, S. S. Kashaf, F. Aghabaglou, I. O. Ghanavati, and A. Tamayol, "Smart bandages: the future of wound care," *Trends in biotechnology*, vol. 36, no. 12, pp. 1259–1274, 2018.

[139] P. Mostafalu, A. Tamayol, R. Rahimi, M. Ochoa, A. Khalilpour, G. Kiaee, I. K. Yazdi, S. Bagherifard, M. R. Dokmeci, B. Ziaie, *et al.*, "Smart bandage for monitoring and treatment of chronic wounds," *Small*, vol. 14, no. 33, p. 1703509, 2018.

[140] P. A. Soares, P. Pinho, and C. Wuensche, "High performance corrugated horn antennas for cosmogal satellite," *Procedia Technology*, vol. 17, pp. 667–673, 2014.

VITA

DIEFF VITAL

December 23, 1986	Born, Torbeck, Haiti
2020	M.S, Electrical Engineering Florida International University Miami, Florida
2017	B.S., Mechanical and Industrial Engineering Florida Polytechnic University Lakeland, Florida

1. <u>Third Place Winner</u>: 2019 IEEE IMS Student Design Competition

2. <u>Honorable Mention</u>: 2019 and 2020 IEEE IMS 3MT Competitions

3. <u>Second Place Winner</u>: Best Poster Award - 2019 Transforming Antenna Center Workshop

4. McKnight Dissertation Year Fellowship 2020-2021

PUBLICATIONS AND PRESENTATIONS

1. Vital, Dieff, Bhardwaj, Shubhendu, and Volakis, John L. (2019), *Textile-Based Large Area RF-Power Harvesting System for Wearable Applications.* IEEE Transaction on Antennas and Propagation

2. Vital, Dieff, and Bhardwaj, Shubhendu (2020), *Misalignment Resilient Anchor-Shaped Antennas in Near-Field Wireless Power Transfer Using Electric and Magnetic Coupling Modes.* IEEE Transaction on Antennas and Propagation

3. Vital, Dieff, Bhardwaj, Shubhendu , and Volakis, John L.(2020), *An Ergonomic Wireless Charging System for Integration with Daily Life Activities.*IEEE Transactions on Microwave Theory and Techniques

4. Mao, Chunxu, Vital, Dieff, Pingjuna L. Werner, Douglas Werner, Bhardwaj, Shubhendu (2019), *Dual-Polarized Embroidered Textile Armband Antenna Array with Omni-Directional Radiation for On/Off-Body Wearable Applications.* IEEE Transaction on Antennas and Propagation

5. Vital, Dieff, Volakis, John L. , Bhardwaj, Shubhendu (2021) "*A Novel Corrugated-Shank Anchor-Shaped Antenna for Wireless Power Transfer,*" (2021) IEEE URSI-GASS

6. Vital, Dieff, Volakis, John L. , Bhardwaj, Shubhendu (2021) *"An Ultra-High-Frequency Wirelessly-Powered Smart Bandage for Wound Monitoring and Sensing using Frequency Modulation,"* (2021) IEEE International Microwave Symposium (IMS)

7. Vital, Dieff, Volakis, John L. , Bhardwaj, Shubhendu (2020) *"A Wireless Power Transfer System (WPTS) Using Misalignment Resilient, On-Fabric Resonators for Wearable Applications,"* (2020) IEEE International Microwave Symposium (IMS)

8. Vital, Dieff , Bhardwaj, Shubhendu, and Volakis, John L. (2019) *"A 2.45 GHz RF Power Harvesting System Using Textile-Based Single-Diode Rectennas"* (2019) IEEE International Microwave Symposium (IMS)

9. Vital, Dieff, Zhong,Jingni, Bhardwaj, Shubhendu, Volakis, John L. (2018), *Loss-Characterization and Guidelines for Embroidery of Conductive Textiles.* 2018 IEEE APS USNC/URSI.

10. Vital, Dieff , Bhardwaj, Shubhendu, and Volakis, John L. (2019), *Misalignment Resilient, Near Field Wireless Power Transfer (WPT) Antennas using Anchor Shape.* 2019 IEEE APS USNC/URSI.

11. Vital, Dieff , Bhardwaj, Shubhendu, and Volakis, John L. (2019), *Bending and Twisting Tests for RF Performances of Textile Transmission Lines.* 2019 IEEE APS USNC/URSI.

12. Vital, Dieff , Bhardwaj, Shubhendu, and Volakis, John L. (2019), *Textile-Based Novel Anchor-Shaped Antenna for Near-Field Wireless Power Transfer.* 2019 IEEE International Workshop on Antenna Technology (iWAT).

13. Vital, Dieff, Bhansali, Shekhar, Volakis, John L., and Bhardwaj, Shubhendu (2020), *Electronic Wound Monitoring Using Fabric-Integrated Data Modulation ,".* 2020 IEEE APS USNC/URSI.

14. Vital, Dieff, Volakis, Bhardwaj, Shubhendu, John L. (2020), *Flexible Ink-Based Interconnects for Textile-Integrated RF Components ,".* 2020 IEEE APS USNC/URSI.

15. Vital, Dieff ,Gonzalez, Alfredo, Alwan, Elias, Volakis, John L., and Bhardwaj, Shubhendu (2020), *A 2.45 –GHz Frugal Dumbbell-Shaped Rectenna Built on Recyclable Substrates ,".* 2020 IEEE APS USNC/URSI.

16. Vital, Dieff, *A 2.45-GHz RF Power Harvesting System Using Textile-Based Single-Didoe Rectennas* ,2020 McKnight Doctoral Mid-Year Research & Writing Conference held in Tampa, Florida February 21, 2020

17. Vital, Dieff, Volakis, John L., Bhardwaj, Shubhendu "Power Transfer and Harvesting System Having Anchor-Shaped Antennas" (US 16/916,187)

18. Vital, Dieff, Dieff, Bhushan, Pulak, Bhansali, Shekhar, Volakis, John L., Bhardwaj, Shubhendu "Smart Bandage for Electrochemical Monitoring and Sensing Using Fabric-Integrated Data Modulation" (US 17/157,624)